Data-driven Techniques Applied to Functional Neuroimaging Analyses

by

WILLIAM REEVES

(Under the Direction of Qun Zhao)

ABSTRACT

The study of magnetic resonance imaging (MRI) data hinges on a strong methodological foundation. With improvements in data collection, methodologies must evolve to keep pace with cutting-edge studies. One such area of study is in the graphical analysis of functional MRI data. This uses neuroactivational patterns inherent in data to determine which areas are most-highly linked with each other.

To define these changes, this work begins by exploring ways to increase sensitivity of pre-existing methods. Using the difference degree test (DDT), it is shown that a modification to the null-model generation method results in higher sensitivity while maintaining accuracy of the findings. This results in the detection of differentially weighted edges which, in turn, help define differentially expressed hub nodes between groups.

Common brain parcellation strategies used in graphical studies often involve the application of an idealized brain parcellation which subdivides the brain into discreet regions based on anatomical landmarks. In practice, idealized anatomical parcellations are flawed due to the brain regions being based on idealized anatomical structures which are not representative of experimental data. A novel method referred to as the independent component analysis (ICA)-based parcellation algorithm (IPA) was developed to overcome these shortcomings. This method employed ICA to detect areas that exhibited similar neuroactivational patterns and subsequently used them to define regions of interest (ROIs). The IPA showed high consistency in ROI definition and showed higher homogeneity than the standard idealized anatomical parcellation and its usefulness in graph theoretic analysis.

After development using humans, the performance of an improved IPA known as the anatomy-free IPA (af-IPS) is profiled using a developmental pig

traumatic brain injury model. The improvements made to the IPA produced regions of interest which maintained spatial consistency while also removing its dependence on idealized anatomy. Groupwise differences between treatment groups were profiled utilizing the subsequent parcellations.

Both the modified DDT and the IPA represent a substantive continuation of decades of research and methodological refinement in the field. While further research must be done to fully explore their potential, the DDT and IPA can hopefully serve as a springboard for further evolution in analytic methodologies.

INDEX WORDS: Functional magnetic resonance imaging,

Neuroimaging, Statistical analysis, Graph theory, Graph simulation, Hypertension, Brain parcellation, Method development, Independent component analysis, Traumatic brain injury, Pig model

Data-driven Techniques Applied to Functional Neuroimaging Analyses

by

WILLIAM REEVES

B.S., Augusta University, 2015 B.S., Augusta University, 2018

A Dissertation Submitted to the Graduate Faculty of the University of Georgia in Partial Fulfillment of the Requirements for the Degree.

DOCTOR OF PHILOSOPHY

Athens, Georgia

©2025 William Reeves All Rights Reserved

Data-driven Techniques Applied to Functional Neuroimaging Analyses

by

WILLIAM REEVES

Major Professor: Qun Zhao

Committee: Heinz-Bernd Schüttler

Jeffrey Urbauer Nathan Yanasak

Electronic Version Approved:

Ron Walcott Dean of the Graduate School The University of Georgia August 2025

DEDICATION

I dedicate this work to all non-traditional students who had to find their true passions the hard way, to those who give it their all to pursue their dreams despite the hardships, and to all those people who support those dreamers along the way. You can only ever be a positive force in this world when you find peace and happiness within yourself.

ACKNOWLEDGMENTS

I thank everyone who helped me to achieve my dreams. I couldn't have done this without my partner whose unwavering support saw me through some of the toughest times in my life. My dad who has provided such an immense opportunity for growth and who has always believed in me and who I can be. I am so appreciative of so many people who have either provided words of encouragement and advice or helped in very tangible ways like helping with groceries or watching over our dog. I'm very lucky to have worked with some amazing people in my lab. From researchers who left soon after I joined to those who will replace me after I leave, each one of you has changed the way I undertake research, and your stellar work has made me a better researcher. Under the guidance of my advisor, I've been able to do and study things I couldn't have comprehended but a few short years ago. At his instruction, I've been able to form myself into the scientist I am today. I'm thankful for so many people in my life, and all I can do is try to return their kindness to those who want to follow in my footsteps. Their generosity and thoughtfulness is a debt I may never be able to repay, but I hope to inspire anyone who wants to pursue science as their career by telling them about the amazing people that I've met through my journey. I truly wish all of you the best of luck.

Contents

A	cknov	vledgments	V
Li	st of	Figures	viii
Li	st of	Tables	xiv
I	The	Study of Magnetic Resonance Imaging Data and Method-	
	olog	rical Review	I
	I.I	A Brief Introduction to Magnetic Resonance Imaging	I
	I.2	A Discussion of fMRI Analysis Methodology	3
	1.3	Conclusion	II
2	Cha	racterization of Resting-State Functional Connectivity Chang	ges
	in H	Iypertension by a Modified Difference Degree Test	12
	2. I	Abstract	13
	2.2	Introduction	14
	2.3	Materials and Methods	15
	2.4	Results	21
	2.5	Discussion	25
	2.6	Conclusion	30
	2.7	Author Contribution Statement	31
3	fMI	RI-based Data-Driven Brain Parcellation using Independent	
	Con	nponent Analysis	32
	3.I	Abstract	33
	3.2	Introduction	34
	3.3	Materials and Methods	36
	3.4	Results	4 I
	3.5	Discussion	48
	3.6	Conclusion	54
	3.7	Acknowledgements	54

	3.8	Author Contribution Statement	54			
4						
	4.I	Introduction	55			
	4.2	Materials & Methods				
	4.3	Results				
	4.4	Discussion	69			
	4.5	Conclusion	74			
5	Con	clusion	<i>7</i> 5			
Appendices						
A	A Supplementary Material - Chapter 3					
Bi	Bibliography 82					

List of Figures

I.I	Example BOLD activation timeseries are shown with example	
	Pearson's correlation values listed in the titles. The blue and	
	red lines represent BOLD activation timeseries that have been	
	Fisher transformed into z-scores (mean of zero and standard	
	deviation of 1). The top plot shows a correlation value of ap-	
	proximately zero whereas the bottom figure shows an elevated	
	correlation of 0.449	5
1.2	An example of a graph is shown where the size of the nodes,	
	shown in red, represents the number of nodes connected to	
	it. The graph contains 100 total nodes and a minimum nodal	
	degree of six	7
2.I	Flowchart of the Difference Degree Test (DDT). The resting	
	state functional connectivity (rsFC) maps and participant de-	
	mographic information are linearly regressed while regressing	
	out the age, sex, and race as nuisance variables. The difference	
	network (D) is used to generate an adaptive threshold value, as	
	well as null networks with matching mean and variance with	
	annihilated internal structure. The difference network, thresh-	
	old, and null networks are used in the final statistical testing to	
	obtain nodal statistical significance which, when thresholded,	
	produces statistically significant differentially expressed hub	
	nodes	18

2.2	The comparative analysis results between the modified (2.2A-	
	2.2C) and base (2.2D-2.2F) DDT are shown for 1 (2.2A,2.2D),	
	3 (2.2B,2.2E), and 5 (2.2C,2.2F) simulated hub nodes. The	
	nodal true positivity rate (TPR) and false positivity rates (FPR)	
	are given along the y-axis, with the different number (4, 7, or	
	11) of differentially weighted edges (DWEs) per hub node be-	
	ing shown along the x-axis. Each different simulation type is	
	shown in the assorted color combinations with the random	
	(Rand) simulation's TPR being shown in blue with FPR in	
	purple, the small world (SmW) TPR in red, FPR in green, and	
	the hybrid (Hyb) TPR in yellow with the FPR in light blue.	
	The error bars shown in the plot represent the standard de-	
	viation of the simulation's TPR/FPR values and are drawn	
	uneven as to illustrate that no T/FPR value ever exceeded 1 or	
	fell below o	23
2.3	A tree graph representation of the hub nodes (red) and differen-	
	tially weighted edges (DWE) connection with other non-hub	
	nodes (blue) is shown. The numbers inside the circle represent	
	the node number	25
2.4	Illustration of the anatomical regions of seven statistically sig-	
	nificant differentially expressed hub nodes. Node 3 is located	
	at the Right (R) Inferior Temporal (light blue), Node 9 at the	
	Right Inferior Parietal (blue), node 10 at the Right Lingual	
	Gyrus (purple), node 31 at the Right Lateral Occipital (red),	
	node 42 at the Right Hippocampus (orange), node 64 at the	
	Left (L) Putamen (yellow), and node 85 at the Left Cerebellum	
	Gray Matter (GM) (green). Presented in radiological orienta-	
	tion with left shown on the right side	26
2.5	Group-segregated box plots of partial correlation values are	
	shown for the seven differentially expressed hub nodes. The	
	group's partial correlation value is listed on the y-axis while	
	the x-axis represents different differentially weighted edges that	
	hub node is connected to (Red: the hypertensive group; Blue:	
	the normotensive group)	27

- 2.6 Modified (Mod) and Base difference degree test (DDT) mean true positivity rate (TPR) and false positivity rate (FPR) is shown for the random (6A), small world (6B), and hybrid (6C) simulation schemes. With the Mod TPR shown as a blue line, the Base TPR in red, Mod FPR in Yellow, and Base FPR in purple, the TPR and FPR values are shown as a function of α significance values. The bars shown on the lines represent a single standard deviation of the simulation over 100 trials.
- - Visualizations of example IPA parcellations. The first column (2A/2C) shows the group independent component analysis (ICA) derived parcellations whereas the second (2B/2D) demonstrates the individualized parcellations. The top row (2A/2B) visualizes parcellations in a normotensive individual while the bottom row (2C/2D) exemplifies the parcellations in a hypertensive individual. Each parcellation is overlaid atop the specified subject's structural T1 data that has been co-registered to fMRI space. The colors present in the parcellation represent the different ROIs defined by the ICA-based parcellation algorithm (IPA) and are consistent across all examples.

39

43

3.3	Intragroup dice similarity coefficient (DSC) distributions of the independent component analysis-based parcellation algorithm (IPA) and Personode individualized parcellations. The data is shown separated into their groups of either normotensive (NRM – blue) or hypertensive (HTN – orange) individuals. The DSC represents the simple spatial overlap of two ROI and is used in this context to quantify the consistency of their definitions. Each DSC is calculated as the overlap between a specified ROI across each subject. Figure 3.3A shows the DSC distribution for the IPA and Figure 3.3B shows the same information for Personode	44
3.4	Parcellation region of interest (ROI) size distributions. Individualized parcellation size distributions are shown in the violin plots with the group-derived parcellations being shown by the downward facing triangles in (3.4A, 3.4B). The individualized parcellation ROI size distributions are further broken down into groups with the NRM being the left side of the violin plots shown in light blue and blue, and the HTN being the right side of the violin plots shown in light orange and orange. For Personode sub-parcellations, the violin and scatter plots represent the distribution for each sub-parcellation of a given	44
3.5	network. MNI gray matter ROI sizes are shown in 3.4C All models' parcellation homogeneity values are shown as violin plots where the 25th and 75th percentiles are shown as shaded areas of the violins. Individualized parcellations from the independent component analysis-based parcellation algorithm (IPA) and Personode models are shown in Figures 3.5A and 3.5C respectively with their group independent component analysis (gICA) derived parcellation counterparts are shown in Figures 3.5B and 3.5D. Figure 3.5E presents the 35 IPA-analogous Montreal Neurological Institute (MNI) regions being shown in Figure 3.4E. For each method, the violin plots were further subdivided into left and right violins with the left violins shown in light blue and blue representing the normotensive individuals and the right violins shown in light orange and	45
	orange representing the hypertensive individuals	47

The nodal p-values and number of differentially weighted edges (DWEs) are shown in the plots above for different trials of the difference degree test (DDT) using different IPA parcellations. In each plot, the blue circles represent the nodal p-value while the orange bar plots represent the number of DWEs attached to each node. 3.6A shows the DDT findings when using the group independent component analysis (gICA)-derived IPA parcellations with 35 total ROI definitions, and 3.6B shows the same information for the individualized parcellations. Figures 3.6C and 3.6D show the DDT results when the number of ROIs increased to 44 for the gICA-derived (3.6C) and individualized (3.6D) parcellations. The black line in each figure denotes the default significance level (α) of 0.05.

49

65

- violin plots separated along sessions and sex assignment. Male individuals are shown in the left violins and females shown in the right violins with the different colors denoting different ROIs. The mean of each distribution is shown as a darkened horizontal line in the left and right violins with the 25th and 75th percentiles being shown in the shaded areas of the violins.

4.3	Group (gIPA) and individualized (iIPA) IPA ROI sizes are	
	shown for all subjects divided along sex (left violin; male, right	
	violin; female) and sessional assignments. The gIPA ROI sizes	
	are shown as inverted triangles in the plots while the analo-	
	gous atlas ROIs are shown as purple triangles. The various	
	colors shown in the plots are used to discern the various ROIs	
	from each other and across sessions. The mean of each group	
	is shown as a dark horizontal line in each of the violins and the	
	shaded areas of each violin represent the area between the first	
	and third quartiles	67
4.4	Ratio of central moments between human and pig datasets is	,
	seen in the figure. The distribution of these data is shown as a	
	box plot with outliers removed for visualization purposes	67
4.5	Homogeneity values are shown for individualized IPA (iIPA),	,
, ,	group IPA (gIPA), and the anatomical parcellations separated	
	along sex and sessional demographics. Various ROIs are shown	
	along the x-axis each of which are represented by a different	
	color of violin. For visualization purposes, only those ROIs	
	that exhibit large differences between males and females are	
	shown. The anatomical atlas demonstrated no sex-linked changes	
	at any timepoint. Male individuals are shown in the left violins	
	while the females are shown in the right violins. The mean of	
	each group is shown as a dark horizontal line in each of the	
	violins and the shaded areas of each violin represent the area	
	between the first and third quartiles	68
4.6	Various graph theory metrics are shown both for the group	
,	(gIPA) and individualized (iIPA) IPA parcellations. The four	
	metrics shown are density (Den), characteristic path length	
	(CPL), modularity (Mod), and functional connectivity strength	
	(FCS) with male individuals being shown in blue box plots and	
	females being shown in red box plots. The data is further sep-	
	arated along sessional lines with the dark vertical lines shown	
	in each plot delineating pre-TBI, one day post-TBI induction,	
	and 63 days post-TBI induction, while the different experimen-	
	tal groups are shown along the x-axis for each plot. Significant	
	differences are also overlaid in the plot with * indicating a p-	
	value of less than 0.05	70
	,	70

LIST OF TABLES

2. I	Demographic information of all individuals involved in the hypertension cohort. The treatment demographic is made up of individuals that are currently undergoing therapeutic treatment for hypertension.	16
2.2	The true and false positivity rate (TPR, FPR) results from data simulation with one hub node are shown with varying differentially weighted edges (DWEs). Three network simula-	16
	tion types were performed with different thresholding methods. Thresholding of the data is either done by an analytical model (aDDT) or by the empirical spread of the data (eDDT).	22
2.3	All anatomical information from the experimental results obtained by DDT processing. Hub nodes are denoted by a red highlight and all DWEs are listed without highlight where the right (R) and left (L) components of brain regions are listed	
	seperately. The associated resting state networks with the hub/non hub nodes include the Auditory (AUDI), Basal Ganglia (BASA), Cerebellar (CERE), Default Mode (DEFA), Executive Control (EXEC), Salience (SALI), and Visual (VISU) networks.	24
3.1	The mean and standard deviation of all homogeneity values shown in Figure 3.4 are shown in the table below with a breakdown of the statistics per group. As the Montreal Neurological Institute (MNI) parcellation is not derived from ICA data, it is not counted as a group-independent-component-analysis (gICA)-derived parcellation denoted by the double line	48
	(81011) defired partenation denoted by the double line	40

4.1 Subject demographics of piglet cohort. Three treatment sch		
	are shown including sham, mild TBI, and severe TBI. Sham	
	subjects received a craniectomy but no traumatic brain injury	
	(TBI) induction. The two TBI groups, mild and severe, are	
	differentiated by their cortical impact parameters of 3mm and	
	9mm respectively. Each subject was scanned over 3 timepoints	
	for a total of 102 scanning sessions	58
4.2	Scanning parameters of all functional and structural MRI data.	59
4.3	Sessional averaged homogeneity values are shown for the spec-	
	ified parcellation methods. Mean values are shown alongside	
	the standard deviation of the data for the individualized IPA	
	(iIPA), group IPA (gIPA) and anatomical parcellation methods.	69

CHAPTER I

The Study of Magnetic Resonance Imaging Data and Methodological Review

I.I A Brief Introduction to Magnetic Resonance Imaging

1.1.1 The physical basis of MRI

Magnetic resonance imaging (MRI) relies on subtle changes brought about by placing nuclei – typically in the form of hydrogen atoms bound within water or fat molecules - in an external magnetic field and applying a perturbative radiofrequency (RF) magnetic pulse to the system to measure the amplitude of these nuclei undergoing precession en masse, known collectively as "bulk magnetization". The net magnetization of various tissues is prepared by using timed applications of additive gradient magnetic fields and RF pulses, leading to differences in signal arising in each tissue. Biologically, the coherence of signal "source" from nuclear magnetization depends on the local susceptibility of tissues, which are indirect measures of physiological structure and processes. By applying a fast Fourier transform (FFT) to received signals stored in a raw data space known as "k-space" images of biological tissues can be obtained, with variations in image contrast correlated with scanner preparatory timing details, tissue properties, and physiological modulation of the tissue. The use of MRI can be found in many different fields and applications. Clinically, MRI can be used to determine pathological changes in a patient's tissue related to a myriad

of different disease states including spinal disc herniation (Sollmann et al., 2023), breast cancer development (Mann et al., 2019), vessel wall imaging (Maupu et al., 2022), and techniques such as real-time MRI can even be used to guide surgeons during an operation (Horvath et al., 2007). On the research side, MRI has been used to study nearly every aspect of the body including liver iron deposition in mice (Simchick et al., 2018), neurological changes linked with nutritional changes in pigs (Ahmed et al., 2023), white matter integrity post traumatic brain injury (TBI) (Fagan et al., 2024), along with many other uses (Kose, 2021).

1.1.2 Functional MRI

One of the many types of MRI is in functional MRI (fMRI). Built upon the underlying theory of MRI, fMRI utilizes what's referred to as the blood-oxygen level dependent (BOLD) signal to detect small magnetic field inhomogeneities created by deoxyhemoglobin. The hemoglobin protein has two states – oxyand deoxyhemoglobin – which are defined by the presence or absence of bound oxygen molecules. When oxygen is bound to the hemoglobin protein, the iron at the center of the heme molecule has no free electrons and creates a bulk diamagnetic effect in the hemoglobin protein. However, when oxygen isn't bound to the protein, there are free electrons located in the heme compound which causes a global paramagnetic effect in an external field (Brown et al., 2014). These two susceptibility states manipulate the coherence of MRI signal in well-perfused tissue, generating image contrast differences on the order of \sim 1% between locally normoxic and hypoxic conditions. The change from oxyhemoglobin to deoxyhemoglobin represents the consumption of oxygen in the body as well as the subsequent vasodilation increasing the local ratio of oxy- to deoxyhemoglobin in active tissue, and when this thought is applied to fMRI scans of the brain, it often gets tied directly to neuronal oxygen consumption. The relationship between this signal and neuronal oxygen consumption isn't as straightforward as it may appear at first glance, however (Hillman, 2014). Changes in the BOLD signal come from a cascade of microvascular events that result in increases in blood flow and blood volume (Raichle, 1998). Despite the BOLD signal often being misattributed directly to neuronal oxygen consumption, repeated studies have used the BOLD signal to show that the brain can be reliably segmented into functional networks both in humans (B. B. Biswal et al., 2010; B. Biswal et al., 1995; Smith et al., 2009), and other model animals (Mantini et al., 2011; Simchick et al., 2019)).

As the BOLD signal is tracked over time, researchers can probe into the

physiological response to a variety of different conditions using the functional timeseries. This includes studies focused on having a participant perform a task or otherwise receive some stimulus (task-based fMRI [tb-fMRI]) or to lie in the MRI in a state of relaxed wakefulness (resting-state fMRI [rs-fMRI]). Taskbased studies can focus on having subjects perform memory (Kumar et al., 2017; Prieto Del Val et al., 2016; Serrano et al., 2020), attention (Bagattini et al., 2017; Meehan et al., 2023), and/or motor (Niu, Cohen, et al., 2021) tasks as well as other paradigms. Each task is designed to focus in on specific and concentrated areas of brain activity. For example, if asked to perform certain motor tasks like tapping your fingers or wiggling your toes, the researchers can specifically focus on the regions of the brain associated with the sensorimotor network. In contrast to tb-fMRI, rs-fMRI involves the participant lying still without being allowed to fall asleep. In this state of relaxed-wakefulness, fMRI can detect the underlying activity of the brain as it functions as a dynamic network. The brain's underlying activity has been used to determine functionally similar areas of the brain that act as integrated networks which we now call resting-state networks (Kwong et al., 1992; Ogawa et al., 1990). Resting-state and task-based fMRI data represent two sides of the same coin in that, taken together, they each profile different phenomena relating to how the brain acts under certain conditions. Both methods benefit from their differences (Lemée et al., 2019; S. Zhang et al., 2016) while also suffering from similar issues (X. Hu & Yan, 2024; Specht, 2019), but taken together, they allow for a more holistic understanding of the brain and its function.

1.2 A Discussion of fMRI Analysis Methodology

1.2.1 Voxel-wise analysis

Given the physical basis of the BOLD signal and some of the findings of previous fMRI studies, the next question that follows is "how does tracking brain oxygen consumption become a scientifically significant result?" To answer this question, a review of current methodologies is warranted (Chen et al., 2017; K. Li et al., 2009; X. Zhan & Yu, 2015) which will be limited solely to rs-fMRI analyses. Regional homogeneity (ReHo) (Jiang & Zuo, 2016; Zang et al., 2004), a common measurement metric in the field, characterizes the similarity of nearby voxels (the three-dimensional extension of two-dimensional pixels) to determine similarities and differences in fMRI data (Xu et al., 2019; F. Zhang et al., 2021; Z. Zhang et al., 2023). Another metric that seeks to utilize the voxel-wise

timeseries directly is known as amplitude of low-frequency fluctuations (ALFF) (Fransson, 2005; Zou et al., 2008). Studies using ALFF quantify spontaneous fluctuations in the voxel-wise timeseries to obtain the fluctuation amplitude present in the data and then obtains its power spectrum for further analysis.

1.2.2 Seed-based analysis

Another branch of rs-fMRI analysis employs the use of seed-based techniques (Andrews-Hanna et al., 2007; Bastos & Schoffelen, 2015; Korgaonkar et al., 2014; Larson-Prior et al., 2009; Sierakowiak et al., 2015; Song et al., 2008) which use a priori information to define regions of the brain and subsequently compare each region to the rest of the brain to find the differences or similarities that exist in the data. The assumption that all brains can fit into an idealized reference brain has obvious limitations in morphologically abnormal brains or individuals who otherwise don't fit into the ideal brain structure that informs those predefined regions of interest (ROIs). One positive aspect of seed-based techniques is their ease of analysis as the ROIs directly tap into biological sources of BOLD signal. These studies (Carpenter et al., 1999; Mulert et al., 2004; Yoshino et al., 2006) often take the timeseries of every voxel and average them to obtain mean regional timeseries that, when obtained for all ROIs, form what is referred to as a timeseries matrix. These rectangular matrices contain regional snapshots of BOLD signals and, when correlation analysis is performed on them, can be used to build a functional connectivity (FC) matrix.

1.2.3 Quantifying regional similarities

An important aspect of many seed-based studies is the analysis of how similar regional timeseries are to one another. The analysis methodology can take many forms, but one common form of quantifying regional similarities is correlation analysis. Correlation analysis between two regions can be quantified using several metrics (Mahadevan et al., 2021). One common metric is Pearson's correlation coefficient used to determine similarities between two vectors. This metric (ρ_{XY}) is given by the equation

$$\rho_{\mathbf{XY}} = \frac{\operatorname{cov}(\mathbf{X}, \mathbf{Y})}{\sigma_{\mathbf{X}}\sigma_{\mathbf{Y}}} \tag{1.1}$$

where $\sigma_{\mathbf{A}}$ is the standard deviation of a given matrix \mathbf{A} and $\operatorname{cov}(X,Y)$ is the covariance of the two vectors X and Y which is given by

$$\operatorname{cov}(\mathbf{X}, \mathbf{Y}) = \langle \mathbf{XY} \rangle - \mu_{\mathbf{X}} \mu_{\mathbf{Y}} = \sum_{i=1}^{N} \frac{(x_i - \bar{x})(y_i - \bar{y})}{N}$$
 (1.2)

The Pearson's correlation coefficient has a range of [-1, 1] where I implies that the two vectors perfectly follow the same trend, -I indicates the two vectors trend linearly together but have opposite trends, and zero means that there is no relationship between the trends in the data. A representation of this relationship can be seen in Figure I.I While Pearson's correlation coefficient is

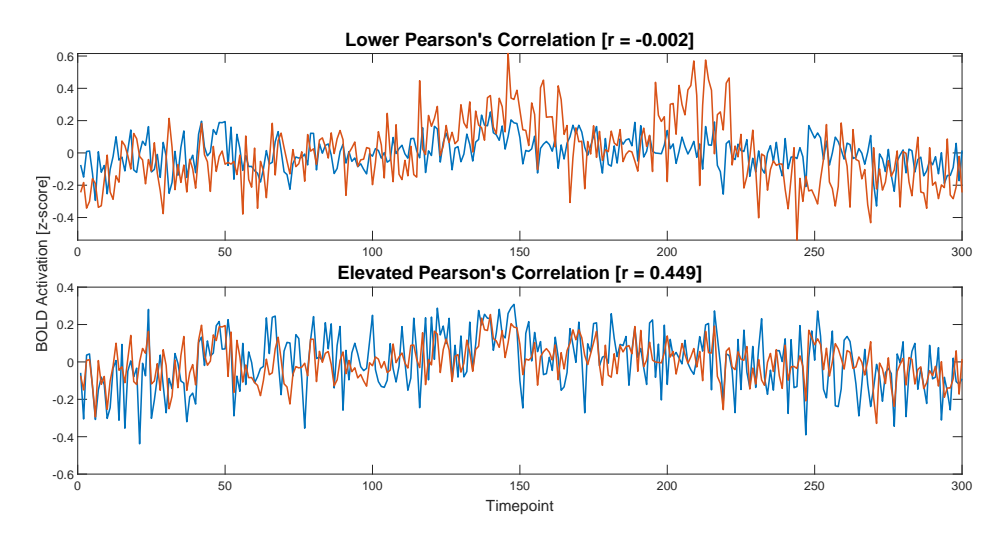


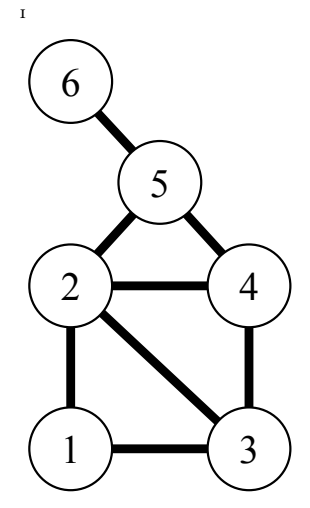
Figure 1.1: Example BOLD activation timeseries are shown with example Pearson's correlation values listed in the titles. The blue and red lines represent BOLD activation timeseries that have been Fisher transformed into z-scores (mean of zero and standard deviation of 1). The top plot shows a correlation value of approximately zero whereas the bottom figure shows an elevated correlation of 0.449.

mathematically intuitive, it is also the most simplistic. Newer methods like partial correlation (Marrelec et al., 2009) perform the same task as the Pearson coefficient, while also regressing out the effects from all other time regional timeseries. Both the Pearson and partial correlation metrics are instantaneous measures of FC, but there remains another category of metrics that attempt to quantify dynamic functional connectivity (dFC). One of the methods used to quantify dFC is wavelet coherence (Bernas et al., 2018; Cîrstian et al., 2023; Yaesoubi et al., 2015) which, alongside a measure of correlation, can also quantify if a given timeseries leads or lags another. Regardless of the method used to obtain similarities between seed regions, the main goal of this step in processing fMRI

data is to create a FC matrix that quantifies activation patterns throughout the brain.

1.2.4 Graph theory applied to functional connectivity

After FC matrices are obtained for every individual in a study, post-processing must be done to determine what differences exist between groups and/or individuals. The primary means of extracting information from FC matrices comes from the application of a subset of mathematics known as graph theory. Graph theory broadly posits that fundamental traits of complex systems can be preserved in structures containing a reduced data content known as graphs, which are comprised of points, referred to as "nodes" or "vertices". Furthermore, these points are connected by structures known as edges¹. A large scale example of a graph can be seen in Figure 1.2. Limiting the discussion to those topics relevant to fMRI analysis (Bullmore & Sporns, 2009; Farahani et al., 2019; van den Heuvel & Hulshoff Pol, 2010; J. Wang et al., 2010), there are many metrics that can be calculated from a graph that provide various network-like descriptions of brain function and connectivity. To gain a deeper understanding of graph theory metrics and what information can be gleaned from them, it is worth it to discuss them in greater detail.



Example graph with 6 nodes and 8 edges present.

Microscale graph theory metrics

This discussion is highly informed by Medaglia, 2017 who provides an excellent overview of graph theory metrics applied to fMRI analyses. Graph theory metrics can be broken into three different scales – micro, meso, and macroscale metrics – that describe the topology and organization structure of a graph. Microscale metrics describe what is occurring on the nodal level. One of the simplest metrics on this scale is nodal degree, which describes the total number of edges a specific node has connecting it to the rest of the graph. Clustering coefficient expands on nodal degree by defining the number of connections between direct neighbors of a specific node: a node's clustering coefficient quantifies how interconnected its neighbors are. If a node and its neighbors are fully interconnected, they can be collectively referred to as a clique. Nodal distance measures how many steps it takes to get from one node to another. Specifically, a node's distance refers to the number of edges it must pass through to get to a terminal node. For example, if two nodes were directly connected, they would have a distance of one whereas two nodes that are connected through a

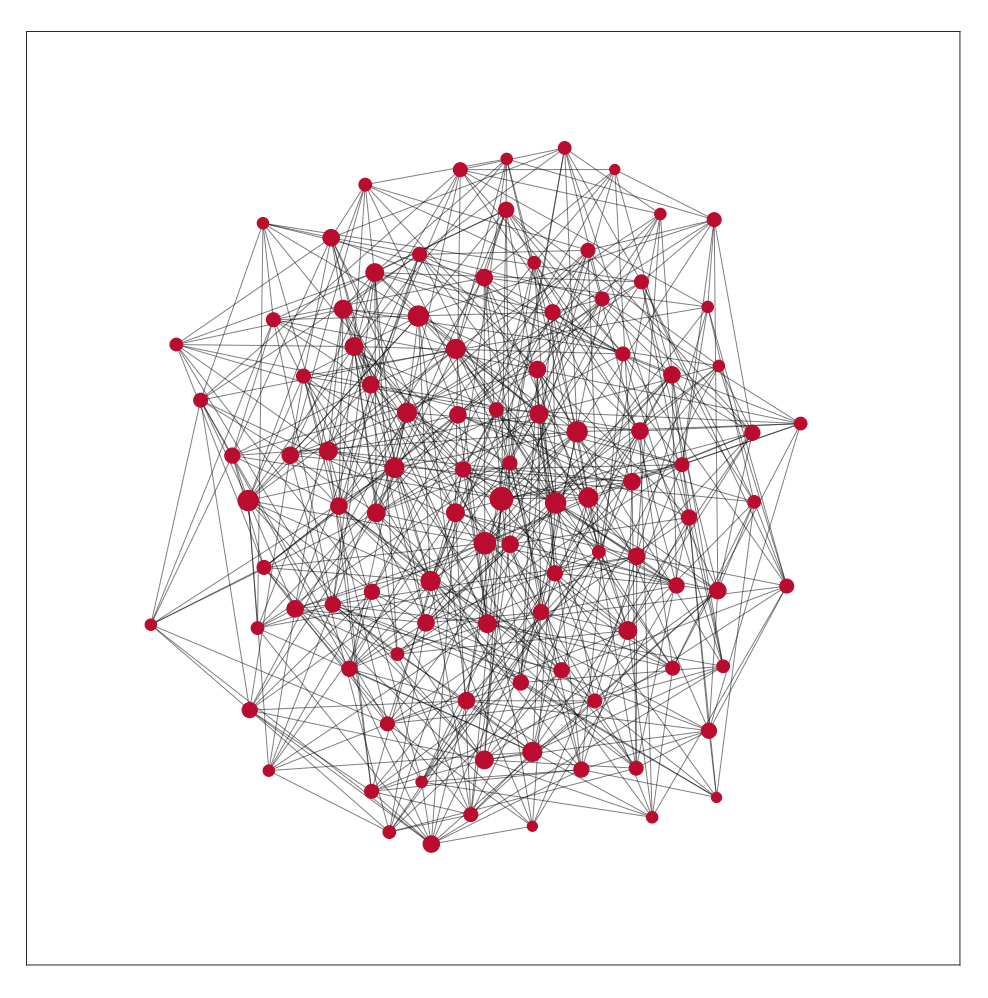


Figure 1.2: An example of a graph is shown where the size of the nodes, shown in red, represents the number of nodes connected to it. The graph contains 100 total nodes and a minimum nodal degree of six.

single intermediate node would have a distance of I. A node's efficiency can be quantified as the inverse distance. The final category of microscale metrics is collectivity referred to as centrality. Centrality describes the role a given node plays in the graph. While there are several different measures of centrality, a few stand out in the characterization of fMRI data. Betweenness centrality measures how often a given node appears in the path connecting distant nodes. A node with high betweenness centrality must be passed through by many other nodes if they want to interact with other nodes in the graph. Closeness centrality quantifies the average shortest distance connecting a given node to all other nodes. Nodes with high closeness centrality can easily interact with many nearby nodes. Lastly, eigenvector centrality describes the relationship of a given

node's centrality to its neighbor's centrality. This metric examines how many connections a node has with other nodes that exhibit a high degree of other centrality measures.

A more intuitive understanding of microscale graph theory metrics may be gained through placing them in the analogy of a person's social circle. If a node represents a person and an edge represents the friendship between those two people, nodal degree represents the number of friends that person has. The person's clustering coefficient represents how many of their friends are friends with each other and the distance/efficiency metrics would represent how close two people in the friend group are. The various centrality measures would represent how their friend groups interact with one another. A person with an increased betweenness centrality would be responsible for connecting all their friend groups together, the closeness centrality would measure if there any barriers to communication between friend groups, and their eigenvector centrality would describe how many influential people that person knows.

Mesoscale graph theory metrics

At the mesoscale, graphs are analyzed to find intermediate-level organizational patterns involving groups of nodes referred to as nodal clusters. These clusters of nodes exhibit both internal and external organizational patterns which are distinct from their local or global effects. One common mesoscale metric is modularity. Nodes exhibiting an increased modularity arrange themselves such that they are highly connected to other nodes in their cluster but have few outside connections to other nodes. At this scale, clusters can organize themselves into distinct structures which are classified into a few categories. Clusters and graphs can be categorized into assortative and disassortative networks. In an assortative network(Hao & Li, 2011) nodes with similar degree are connected to one another while a disassortative network does not show the same connectivity pattern between nodes of the same degree. Modular networks are subdivided into modules which are often connected to each other through intermediating nodes referred to as connector hubs. For graphical structures, hubs are nodes that exhibit high connectivity(Kirkley, 2024) and often exhibit elevated betweenness centrality. Finally, a core-periphery network is one that exhibits a central interconnected structure but whose peripheral nodes exhibit low interconnectivity. Mesoscale cluster organization can exhibit dynamic connectivity and can change over time(Khambhati et al., 2018).

Macroscale graph theory metrics

Macroscale metrics, often called global metrics, profile the organization of a graph on the whole. One such macroscale metric is graph density, defined as the ratio of the number of connections present in the graph versus the number of possible connections in the graph. This metric describes on a macroscale what is seen on the microscale, and often microscale metrics can be averaged across the graph to give further insight into macroscale organization. Examples of these averaged metrics include global clustering coefficient, characteristic path length, and global efficiency. Of these averaged metrics, the global clustering coefficient averages the local clustering coefficient of each node to determine to what extent a graph is interconnected. Another macroscale metric is the characteristic path length which is the average of all distances in a graph. In the same way that a node's efficiency is given as the average inverse of its distances, a graph's global efficiency can be measured as the inverse of characteristic path length. A final metric that is often used in fMRI analysis is the small world index (or small worldness) of a graph. A graph that exhibits an increased small-world index shows high interconnectivity inside clusters of nodes while exhibiting low connectivity to nodes outside of the cluster. This small world index differentiates from the mesoscale modularity in that it attempts to quantify how clusters of nodes interact with other clusters on the macroscale.

Calculating graph theory measures for an individual or cohort allows for the comparison and identification of significant differences in network structure. These findings have been used to study human development (Bassett et al., 2011), memory (X. Liang et al., 2015), neuropsychiatric disorders (Xia & He, 2011), neuropathologies (Fornito & Bullmore, 2015), and cognitive dysfunction (Miri Ashtiani et al., 2018) just to name a few uses its found in specifically fMRI post-processing.

1.2.5 Blind-source separation and independent component analysis

While seed-based FC analysis is a very popular method for analyzing fMRI data, another technique that is widely used is called blind-source separation (BSS). Broadly speaking, BSS is an umbrella term used to describe techniques that seek to recover underlying signals based on a condition of independence. There are two BSS techniques that are widely used: principal component analysis (PCA) and independent component analysis (ICA). Both methods seek to project the

data onto axes that maximize independence of the underlying components of the data. These two methods differ in how the axes are constructed. In PCA the axes are built based on the variance of the data. PCA has a long history in the field (Andersen et al., 1999; Viviani et al., 2005) where it has seen use in denoising (C. G. Thomas et al., 2002) and dimensionality reduction (Sidhu et al., 2012) of fMRI data amongst other uses (Smith et al., 2014; Wylie et al., 2024).

Independent component analysis defines its axes of independence based on measures of non-gaussianity. Through examining the standardized moments of the data, specifically the kurtosis (or "tailedness") of the data, ICA establishes the statistical independence of the underlying signals comprising the data. ICA assumes that the underlying sources are linearly independent and can be expressed as $\mathbf{X} = \mathbf{MS}$ where \mathbf{X} is the observed data, \mathbf{S} is the source signals, and \mathbf{M} is the so-called "mixing" matrix that describes how the sources are mixed. Once the mixing matrix \mathbf{M} is determined, it is a relatively straightforward task to recover the source signals (Mika, 2023). Once the mixing matrix has been calculated, inverting the matrix and applying it to the observed signals yields the underlying sources of those signals.

One widely available tool for performing ICA is a software suite collectively referred to as Functional Magnetic Resonance Imaging of the Brain (FMRIB) Software Library (FSL) (Jenkinson et al., 2012) which can perform three different versions of ICA: single-session ICA, multi-session temporal concatenation, and multi-session Tensor-ICA. Single-session ICA is the simplest case of ICA where an individual's data will undergo the ICA process as previously described. Multi-session temporal concatenation functions much in the same way that single-session ICA does, but stitches (concatenates) multiple individuals' timeseries together to form one long timeseries that increases the statistical power of individual components. The multi-session tensor-ICA places individual data along a higher-dimensional space to create a tensor before performing ICA on the data to obtain independent components. Each of these methods produces independent components (ICs) which are represented as spatial activation maps. These ICA techniques have been in use for over two decades (McKeown et al., 1998). In the last two decades however, the classification of ICs into signal, noise, and artifact categories has remained an open problem (Chou et al., 2022; Glasser et al., 2019; Griffanti et al., 2017; McKeown et al., 2003). Regardless of the classification of components, ICA has been used in many studies for artifact or noise removal (Carone et al., 2017; Griffanti et al., 2014), identification of RSNs (Pendse et al., 2011), and in the analysis of a variety of disease states (Cole et al., 2010).

1.3 Conclusion

Non-invasive studies based on MRI have become commonplace with fMRI being a very popular option when designing a study due to the statistical power of the underlying BOLD signal. Applying seed-based techniques to BOLD signals allows for the construction of graphs which further profile the underlying organizational structure of the brain. It is through the micro-, meso-, and macroscale analyses of graphs that differences between groups can be discovered. Additionally, techniques such as ICA can be used to calculate the underlying temporal or spatial signals present in the fMRI data which further exhibits how useful the fMRI protocol is. In the subsequent chapters, a discussion of previous and ongoing research into the areas of algorithm development, statistical testing, and methodological improvements will be detailed.

CHAPTER 2

CHARACTERIZATION OF RESTING-STATE FUNCTIONAL CONNECTIVITY CHANGES IN HYPERTENSION BY A MODIFIED DIFFERENCE DEGREE TEST

2.1 Abstract

2.1.1 Introduction

Hypertension affects over a billion people worldwide, and the application of neuroimaging may elucidate changes brought about by the disease. We have applied a graph theory approach to examine the organizational differences in resting-state functional magnetic resonance imaging (rs-fMRI) data between hypertensive and normotensive participants. To detect these groupwise differences, we performed statistical testing using a modified difference degree test (DDT).

2.1.2 Methods

Structural and rs-fMRI data were collected from a cohort of 52 total (29 hypertensive, 23 normotensive) participants. Functional connectivity maps were obtained by partial correlation analysis of participant rs-fMRI data. We modified the DDT null generation algorithm and validated the change through different simulation schemes, and then applied this modified DDT to our experimental data.

2.1.3 Results

Through a comparative analysis, the modified DDT showed higher true positivity rates (TPR) when compared with the base DDT while also maintaining false positivity rates below the nominal value of 5% in nearly all analytically thresholded trials. Applying the modified DDT to our rs-fMRI data showed differential organization in the hypertension group in the regions throughout the brain including the default mode network. These experimental findings agree with previous studies.

2.1.4 Conclusion

While our findings agree with previous studies, the experimental results presented require more investigation to prove their link to hypertension. Meanwhile, our modification to the DDT results in higher accuracy and an increased ability to discern groupwise differences in rs-fMRI data. We expect this to be useful in studying groupwise organizational differences in future studies.

2.2 Introduction

An estimated 1.28 billion people worldwide are living with hypertension ((NCD-RisC), 2021) which leads to an elevated risk for heart attack, stroke, and Alzheimer's disease, among a myriad of other maladies. Due to the global incidence of hypertension, significant effort has been devoted towards characterization of its manifestations in the body and brain, including the use of neuroimaging (e.g. Jennings et al., 2008). Functional magnetic resonance imaging (fMRI) is used in both clinical (e.g. Orringer et al., 2012) and research applications, as it gives insight into brain function through the blood-oxygen level dependent (BOLD) effect (Glover, 2011). Resting-state fMRI (rs-fMRI) involves scanning the brain while the participant is in a state of relaxed wakefulness, to study the brain's resting state functional activity. This type of imaging is widely used in both animal (e.g. Simchick et al., 2019) and human participants (e.g. M. H. Lee et al., 2013; Smitha et al., 2017). Traditional methods of processing rs-fMRI data involve independent component analysis (e.g. Calhoun and de Lacy, 2017), and more recent studies have used machine learning (e.g. Khosla et al., 2019) to find latent structure from rs-fMRI data.

Alongside the increase of machine learning applied to neuroimaging, there has been a rise in the use of graph theory as a method of analyzing rs-fMRI data. Graph theory posits broadly that complex systems can be broken down into a graph which is comprised of distinct points (nodes) and the connections between those points (edges). Graph theory can be applied to many different neuroimaging topics including cerebral blood flow in a resting state (Melie-García et al., 2013), as well as disease states such as hypertension (López-Gil et al., 2014), traumatic brain injury (Harris et al., 2016), and psychosis (Ganella et al., 2018). Graph theory can also be applied in the form of a Gaussian graphical model that is built upon structurally informed data (Higgins et al., 2018), with the best way to optimize these graphs also being an area of ongoing study (Chung et al., 2021). Many of these studies focus on graph structure such as nodal degree – a measure of how many connections a node has to other nodes – and topology (e.g. Bassett and Bullmore, 2006, Colizza et al., 2006, Crossley et al., 2014). We believe the group-to-group comparisons of nodal expression is deserving of further investigation, however. In this study we seek to elucidate the changes brought about by hypertension through group-wise differential expression of hub nodes.

A recent study (Higgins et al., 2019) demonstrated that a difference degree test (DDT) can be used to identify groupwise differences in resting-state functional connectivity (rsFC) graphs. The study first identified differentially

weighted edges (DWEs), then constructed a null model based on this differential expression and determined a statistical significance threshold of DWEs by either a theoretical/analytical model (aDDT) or by the empirical spread of the data (eDDT). These thresholds and null networks were then used to discern whether a node had a statistically significant number of DWEs attached to it. If statistical significance could be established, this node was then referred to as a differentially expressed hub node. This methodology resulted in high statistical power of results and was validated through simulation in the previous study. Some applications of the DDT include tracking neurological changes brought about by dietary restrictions in a porcine model (Ahmed et al., 2023).

The aim of the current study is to identify functional changes in the brain associated with hypertension to better understand the impacts of the disease. We hypothesize that the neurological changes caused by hypertension can be better identified and quantified using a modified DDT compared to the base DDT. We propose a modification to the DDT that produces higher true positivity rates (TPR) as compared to the base DDT. With the increase in TPR, the modification does result in an elevated false positivity rate (FPR) that stays below a nominal value of 5%. After we validate the proposed modification, we apply our modified DDT to experimental data to determine the organizational changes of the hypertensive cohort. In section 2 we detail the simulations that were performed, and in section 3 we show the results of this simulation along with the results of applying this modified DDT to our rs-fMRI data.

2.3 Materials and Methods

2.3.1 Participant demographics and data acquisition / processing

Our experimentally obtained data consisted of 52 total individuals, the demographic breakdown of which can be seen in Table 1 below. For a participant to be classified as normotensive, their measured blood pressure on the day of their scan must have a systolic pressure below 130 mmHg, a diastolic pressure below 80 mmHg, and must report no ongoing treatment for hypertension. If any of these criteria were not met, the participant was placed in the hypertension group. If a participant was currently pregnant or nursing or if the participant had previous diagnosis of congestive heart failure they would be excluded from the study. Each participant underwent rs-fMRI and 3D MR structural scanning on a Siemens 3T Magnetom Vida MRI scanner (Siemens Health Solutions, Malvern, PA). Resting state fMRI scans (2D-EPI, 48 slices, TR=1200ms, TE=33.00ms,

FA=57°, FOV=240x240 mm2, matrix=120x120, slice thickness=3mm, 500 total volumes) were acquired using a BioMatrix Head/Neck 20-channel receive coil. Structural images were also acquired, using a sagittal 3D scan (MPRAGE, 176 slices, TR=2300ms, TE=2.43ms, FA=9°, FOV=270x270mm2, matrix=240x256, slice thickness=1.2mm).

Data processing was performed using the Statistical Parametric Mapping

Table 2.1: Demographic information of all individuals involved in the hypertension cohort. The treatment demographic is made up of individuals that are currently undergoing therapeutic treatment for hypertension.

		Hypertension	Normotensive	Overall
	N	29	23	52
	Treatment	13	0	13
Age				
-	Mean	41.2	39.7	40.5
	Standard Deviation	2.7	3.1	3.0
Diabetes				
	Diabetic	3	О	3
	Non-Diabetic	25	23	48
	Unknown	I	О	I
Race				
	African American	24	IO	34
	Caucasian	5	13	18
Sex				
	Female	14	14	28
	Male	15	9	24

12 (Penny et al., 2011) toolkit with MATLAB 2021b (MathWorks, Natick, MA). Preprocessing of the rs-fMRI data began with slice timing correction followed by unwarping, registration to a reference space, timeseries detrending, and z-score transformation. The data was further registered to a standard space based on the MNI152 CerebrA atlas (Fonov et al., 2011) and parcellated into 88 cortical and subcortical regions using the same atlas. No band-pass filtering was done due to the detrending and regional averaging proving sufficient to smooth time-series noise. Normalized rs-fMRI timeseries were averaged to form 88 mean regional time series, and then a 88×88 rsFC map was obtained by partial correlation analysis, which was used to infer direct correlation while regressing out the effects of all other regions in the brain (Smith et al., 2013). This rsFC map represents regional time series correlations between every region in the atlas.

2.3.2 Difference Degree Test

The difference degree test (DDT) was used as a statistical test to identify brain regions contributing to changes in gray matter communications between groups. Figure 2.1 presents a flowchart of DDT processes. We input individual rsFC maps and participant demographic information into a linear regression algorithm that produced a p-value matrix based on group-wise differential expression. This step involved building a linear model based on the partial correlation value of a region over all the participants to obtain a p-value based on those results for all the regions. As a part of the linear regression, age, sex, race, and medication status were regressed out as nuisance variables while obtaining their p-values. Subtracting each p-value from 1 produced a difference network D, a matrix that represented the group-wise differential expression of each region. The difference network was then input to the null model generation algorithm to generate a null model, as well as a threshold value based on either theoretical or empirical distributions.

After the threshold value and null difference networks were obtained, we input those along with our difference network into the binomial statistical test. This step in the DDT used the null difference networks to establish a null probability based on binomial probability distribution-function (PDF) testing. This null probability was compared against the binomial PDF-tested difference network to find those differentially expressed hub nodes that exhibited a statistically significant number of nodes attached to them. The result is a measure of nodal statistical significance that, when thresholded (α =0.05), tells us which nodes express significant differential expression between the two groups.

The base DDT (Higgins et al., 2019) null-model generation algorithm was modified by the implementation of a brute-force mean/variance (BFMV) matching algorithm. This algorithm (Zalesky et al., 2012) was able to match the mean and variance of a given matrix with higher accuracy than that of the Hirscheberger-Qi-Steuer (HQS) algorithm (Hirschberger et al., 2007) found in the previous study. To achieve higher accuracy, the algorithm iteratively converged toward the mean and variance of a given matrix via vector addition. An ideal null generation algorithm produces a null that perfectly matches the mean and variance of a data matrix while also annihilating its internal structure. Annihilating the internal structure of the null model is important to avoid unwanted structure. This unwanted organization can come in the form of increased nodal degree among other graph theory metrics which can lead to incorrect null probability.

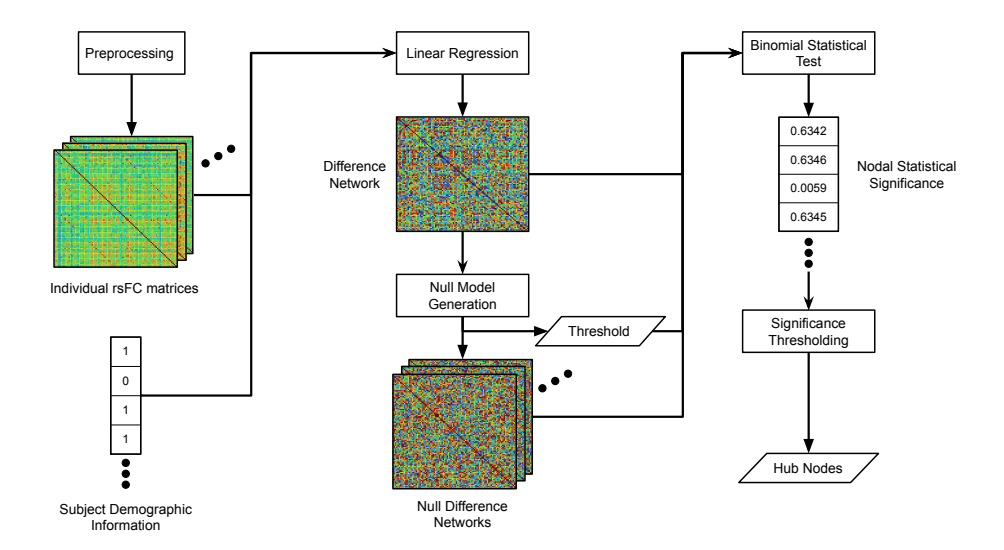


Figure 2.1: Flowchart of the Difference Degree Test (DDT). The resting state functional connectivity (rsFC) maps and participant demographic information are linearly regressed while regressing out the age, sex, and race as nuisance variables. The difference network (D) is used to generate an adaptive threshold value, as well as null networks with matching mean and variance with annihilated internal structure. The difference network, threshold, and null networks are used in the final statistical testing to obtain nodal statistical significance which, when thresholded, produces statistically significant differentially expressed hub nodes.

2.3.3 Data Simulation

To study the performance of the modified DDT, data simulation was performed. The goal of this data simulation was to build an underlying graphical structure, to select out and control for different number of hub nodes and DWEs, and to evaluate with what accuracy the DDT identified the given test parameters. We used three different simulation structures – random, small-world, and hybrid – each with differing underlying structure. The process of building the simulations consisted of building a common base matrix that all individuals would be based off, construction of a symmetric normally distributed perturbation matrix for each simulated individual, and the addition of an offset for all randomly selected DWEs for the test group. While selecting for the underlying structure, we also had control of the total number of nodes (N) representing brain regions in each simulation and the number of individuals in the groups.

These values were defined as 35 total nodes and 40 individuals per group for all simulations.

Building Common Base Matrix and Constructing Simulated Individual's Data

For random data simulations, a symmetric matrix of $N \times N$ dimensions was built with a normal distribution of zero mean and 0.12 standard deviation $(\mathcal{N}(0,0.12))$ for all off-diagonal elements manually defining 1 for all diagonal elements. This represented the common matrix by which all simulated individuals were based on for a random simulation trial. This type of random sampling resulted in a graph that has intrinsic structure, including some local clustering and short path lengths commonly seen in small-world graphs (Zalesky et al., 2012). Because we had no precise control over this common matrix's underlying clustering or path lengths, we differentiated this from the small-world matrix which has more structural control in its algorithm.

Small-world simulations started with a random rewiring algorithm (Watts and Strogatz, 1998) for building a small-world network. This small-world graph was converted into a precision matrix that was subsequently inverted to build a correlation matrix. The resulting correlation matrix was the small-world common matrix, and this matrix represented a simulated dataset that shows high local clustering and short path length in its equivalent adjacency matrix.

Hybrid data simulations were designed to use some of the underlying structure present in experimental data. By using the data from our study, we could preserve some of the more nuanced interactions that may be lost by random sampling of normal distributions. To accomplish this, a normotensive individual from our study was picked at random and N mean regional time series were extracted. Pearson correlation was then performed on these regional time series to obtain the N×N correlation matrix which defined the common matrix for a given hybrid data simulation.

Once the common matrix had been constructed, control and test group data were generated with each group containing the same number of individuals per group. To build each individual's data, we added a symmetric perturbation matrix with $\mathcal{N}(0,0.12)$ distribution to the common matrix. For control individuals, this resulting matrix was representative of that individual's data. For any number of selected DWEs for a given node in the test group, we also introduced a random offset (δ) with a $\mathcal{N}(0.1,0.02)$ distribution for individuals in the test group representing a differentially weighted edge. Alternatively stated: the k^{th} individual's data matrix \mathbf{M}_k , with common matrix \mathbf{C} and perturbative matrix \mathbf{P}_k , is defined as $\mathbf{M}_k = \mathbf{C} + \mathbf{P}_k$, and for a test individual's DWE be-

tween nodes i and j, $(m_{j,i})_k = (m_{i,j})_k = c_{i,j} + (p_i, j)_k + (\delta_i)_k$. For a given simulation, the chosen common matrix stayed the same for all individuals, but in the case of running multiple trials, this matrix would be randomly rebuilt. The mean of the perturbation matrix was chosen so that the weights would have an equal distribution about zero, and the standard deviation was chosen as it allowed for the inclusion of noise without allowing matrix values to exceed I.

Comparative Analysis of the DDTs

To quantify the performance of the modified DDT as compared to the base DDT, a comparative analysis was performed. For this analysis, a simulation's true positivity rate (TPR) and false positivity rate (FPR) was calculated and using the following formulas

$$TPR = \frac{1}{S} \sum_{i=1}^{S} \frac{TP_i}{TP_i + FN_i} \quad FPR = \frac{1}{S} \sum_{i=1}^{S} \frac{FP_i}{FP_i + TN_i}$$
 (2.1)

where TP is the true positive, FN is false negative, FP is false positive, and TN is true negative. These values differ from a per-run TRP/FPR as they were averaged the results over S=100 trials. Along with these mean TPR and FPR values, the standard deviation of the simulation's TPR and FPR values was also recorded. For each simulation scheme, the process of running 100 trials was repeated over 1, 3, and 5 hub nodes while also changing the number of DWEs per hub nodes to be 4, 7, and 11. This means the comparative analysis represents the results from 2700 individual simulations with the TPR and FPR values quantifying the accuracy of the modified and base DDTs.

After the comparative analysis and the processing of experimental results, further simulation was performed to mimic the parameters found through processing the experimental data. These experimentally analogous simulations were designed such that the total number of nodes, number of individuals per group, number of hubs, and DWEs per hub would be chosen to match the results seen in the experimental results found by the modified DDT. The purpose of this test was twofold. First was to compare the modified DDT's capability to correctly identify hubs and DWEs given an analogous system to our experimental data to the base DDT, and second was to investigate the sensitivity of the modified DDT through changing the significance threshold value α as compared to the base. To the second point, S=100 simulations were performed with the mean and standard deviations of TPR and FPR of those trials calculated as previously described for a range of α values from 0.005 to 0.05 in increments

of 0.0025 resulting in a total of 5700 individual simulations to profile the sensitivity curve as a function of α .

2.4 Results

2.4.1 Comparison of aDDT and eDDT Thresholding Methods

The results obtained from processing simulated data with one hub node for different test parameters are seen in Table 2 where the DDT used both aDDT and eDDT thresholding methods. Nodal TPR for every simulation is at or above 0.920 (92%) with 13 out of 18 of the tests showing a 100% TPR. Nodal FPR for all aDDT testing shows a downward trend as the number of DWEs increases. Nodal FPR for all eDDT tests does not exhibit trending as seen in aDDT data and is greater than aDDT FPR in every direct comparison. DWE TPR exhibits roll off as the number of DWEs increases and remains above 80% in all aDDT simulations. DWE FPR exhibits a decrease in all tests as the number of DWEs is increased with values at or below 2.1% for all tests. Due to the increase in FPR, eDDT was not used in further analyses.

2.4.2 Comparative Performance of the Modified DDT

The results of DDT comparative analysis with 1, 3, and 5 hub nodes are shown in Figure 2.2 below. The modified DDT (Fig. 2.2A-2.2C, upper section) produces higher nodal TPR values with a lower standard deviation than the base DDT (Fig. 2.2D-2.2F) in all the reported simulations. Along with this increased nodal TPR (blue, red, yellow shades), the modified DDT (Fig. 2.2A-2.2C, lower section) also presents an increased nodal FPR (purple, green, light blue shades) for all simulations when compared to the base DDT (Fig. 2.2D-2.2F). While below a nominal value of 0.05 for 24 out of the 27 simulations, nodal FPR rises above the nominal value in the case of 5 hub nodes with 11 DWEs per hub (the last 3 columns in Fig. 2.2C).

2.4.3 Experimental Data

Applying the modified DDT to the 52-participant, experimental partial correlation matrices resulted in the discovery of 5 hub nodes with 26 unique connections attached to those hubs. The anatomical labels associated with the nodes and DWEs are seen in Table 3 along with their associated resting state networks

Table 2.2: The true and false positivity rate (TPR, FPR) results from data simulation with one hub node are shown with varying differentially weighted edges (DWEs). Three network simulation types were performed with different thresholding methods. Thresholding of the data is either done by an analytical model (aDDT) or by the empirical spread of the data (eDDT).

			Nodal	Nodal	DWE	DWE
Simulation	Thresholding	DWEs	TPR	FPR	TPR	FPR
Random	aDDT	4	0.990	0.044	0.918	0.020
		7	1.000	0.035	0.894	0.017
		II	1.000	0.022	0.882	0.012
	eDDT	4	0.980	0.073	0.865	0.011
		7	1.000	0.071	0.840	0.009
		II	1.000	0.066	0.815	0.007
	aDDT	4	0.980	0.048	0.923	0.021
Small World		7	1.000	0.035	0.903	0.016
		II	1.000	0.024	0.875	0.013
	eDDT	4	1.000	0.070	0.840	0.010
		7	1.000	0.069	0.836	0.009
		II	1.000	0.064	0.821	0.007
Hybrid	aDDT	4	0.920	0.044	0.873	0.020
		7	1.000	0.030	0.880	0.016
		II	1.000	0.023	0.856	0.012
	eDDT	4	0.990	0.067	0.825	0.011
		7	1.000	0.080	0.820	0.010
		II	1.000	0.069	0.801	0.007

(Smith et al., 2009). With a median nodal degree of a hub being 5, this resulting graphical structure is seen in Figure 2.3. From the figure we can see two discreet networks of connections separated by hemispheres. The right thalamus (34) and right hippocampus (41) exhibit an indirect connection mediated by a cross-hemisphere connection to the left vermal lobules (87). In a similar fashion, the left caudal middle frontal (79) and the left pars triangularis (63) exhibit an indirect connection connected by a cross-hemisphere link to the right caudal middle frontal (35). The only direct connection between two hub nodes is seen in the left pars triangularis (63) and left pars orbitalis (81). As shown by Figure 2.4, hubs are approximately evenly distributed between hemispheres with 3 out of 5 hubs are located on the left hemisphere and the remaining 2 being located on the right. Tracing the nodes and DWEs back to the individual's partial correlation value results in the distributions seen in Figure 2.5. The group

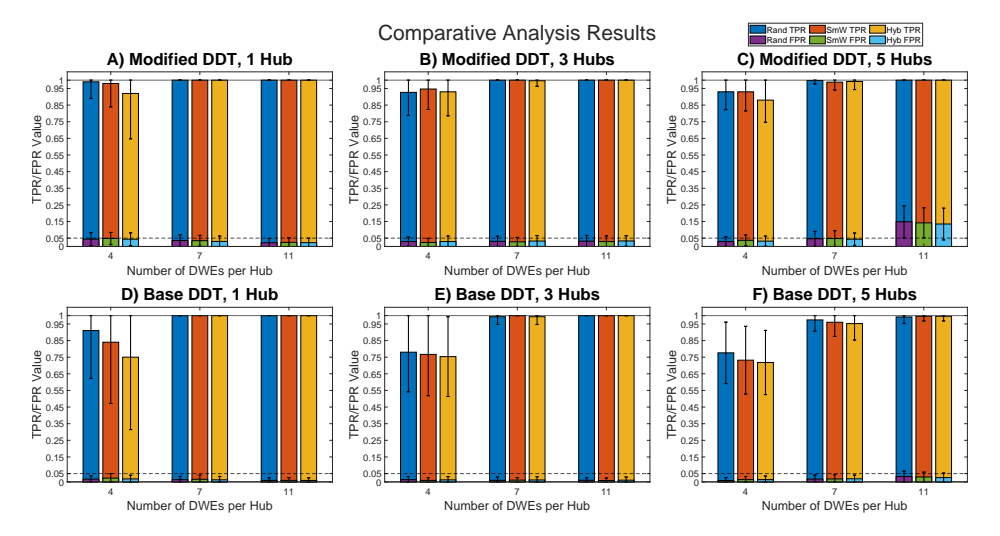


Figure 2.2: The comparative analysis results between the modified (2.2A-2.2C) and base (2.2D-2.2F) DDT are shown for I (2.2A,2.2D), 3 (2.2B,2.2E), and 5 (2.2C,2.2F) simulated hub nodes. The nodal true positivity rate (TPR) and false positivity rates (FPR) are given along the y-axis, with the different number (4, 7, or II) of differentially weighted edges (DWEs) per hub node being shown along the x-axis. Each different simulation type is shown in the assorted color combinations with the random (Rand) simulation's TPR being shown in blue with FPR in purple, the small world (SmW) TPR in red, FPR in green, and the hybrid (Hyb) TPR in yellow with the FPR in light blue. The error bars shown in the plot represent the standard deviation of the simulation's TPR/FPR values and are drawn uneven as to illustrate that no T/FPR value ever exceeded I or fell below o.

partial correlation values shown in Figure 2.5 do not exhibit any simple differential relationship with both group's interquartile range overlapping for every connection at every node.

2.4.4 Experimentally Analogous Simulations

To build experimentally analogous simulations, the total number of nodes (N) was selected to mimic those found in the experimental cohort, the number of members per group was set to 30, the number of hubs was set to 7 and the number of DWEs per hub was set to 5 to match the results shown in Figure 2.5. The results of this simulation are seen in Figure 2.6. An increase in modified DDT nodal FPR can be seen in the figure. Mean FPR values for the hybrid simulation stay below nominal while random and small world simulations do

Table 2.3: All anatomical information from the experimental results obtained by DDT processing. Hub nodes are denoted by a red highlight and all DWEs are listed without highlight where the right (R) and left (L) components of brain regions are listed seperately. The associated resting state networks with the hub/non-hub nodes include the Auditory (AUDI), Basal Ganglia (BASA), Cerebellar (CERE), Default Mode (DEFA), Executive Control (EXEC), Salience (SALI), and Visual (VISU) networks.

Region Number	Region Label	Resting State Network		
3	R Inferior temporal	DEFA		
6	R Lateral Orbitofrontal	EXEC		
12	R Transverse Temporal			
24	R Pallidum	DEFA		
29	R Isthmus Cingulate			
33	R Superior Frontal	EXEC		
34	R Thalamus			
35	R Caudal Middle Frontal			
38	R Superior Temporal	AUDI, SALI		
39	R Cerebellum Gray Matter	CERE		
40	R Posterior Cingulate	DEFA		
41	R Hippocampus	DEFA		
57	L Medial Orbitofrontal	EXEC, DEFA		
58	L Paracentral			
59	L Parahippocampal			
62	L Putamen	BASA		
63	L Pars Triangularis			
67	L Ventral Diencephalon			
69	L Middle Temporal			
72	L Pars Opercularis			
73	L Isthmus Cingulate			
76	L Entorhinal			
79	L Caudal Middle Frontal			
81	L Pars Orbitalis			
83	L Cerebellum Gray Matter	CERE		
85	L Hippocampus	DEFA		
87	L Vermal lobules I-V			
88	L Supramarginal			

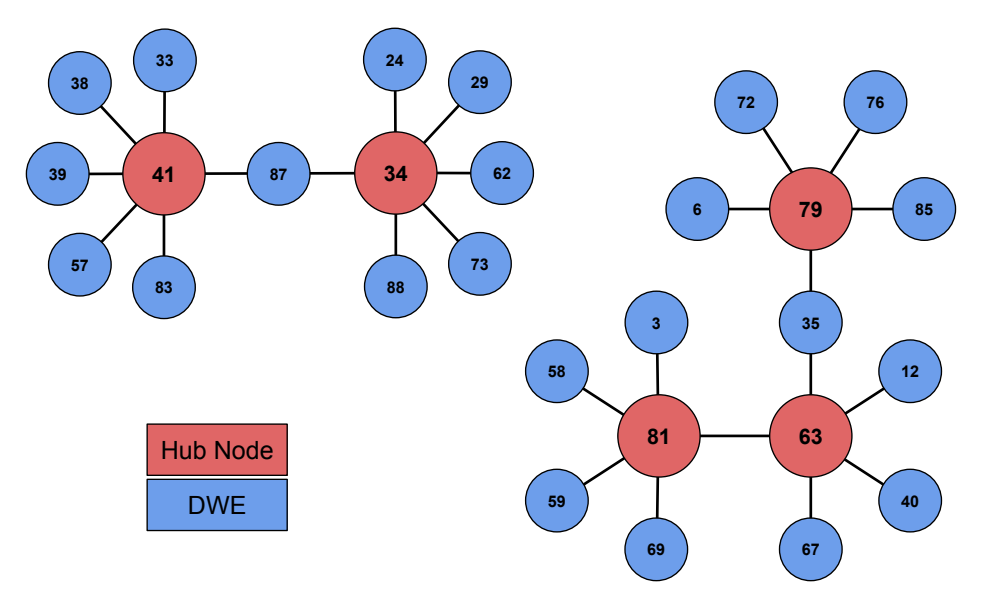


Figure 2.3: A tree graph representation of the hub nodes (red) and differentially weighted edges (DWE) connection with other non-hub nodes (blue) is shown. The numbers inside the circle represent the node number.

not. Also seen in Figure 2.6, the modified DDT obtains a higher mean nodal TPR at every value of α in every simulation type. In 14 out of the 57 total trials modified nodal TPR values were found to be significant via two-sided t-test with 99th percentile confidence intervals compared to the base DDT. With 12 out of 14 of the significant TPR values being found at lower α (0.005, 0.0150, 0.0175, and 0.020), the remaining 2 significant modified TPR values were found at the experimental α value of 0.05 in the small world and hybrid simulations.

2.5 Discussion

In this work, we implemented a modification to the DDT which was validated through simulation and then applied to our experimental data. Application of the BFMV matching algorithm modification to the DDT resulted in increased nodal TPR while still producing below nominal FPR values for nearly all aDDT simulations. We also reported that the modified DDT proves reliably accurate against a wide range of simulation parameters. Through rigorous statistical testing illustrated by Figures 2.2 & 2.6, the modified DDT demonstrated an ability to pick out the ground truth hub nodes with higher accuracy and more consistency when compared with the base DDT. This result is exemplified by

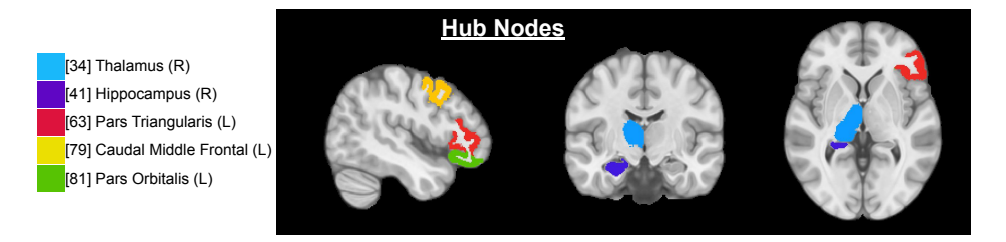


Figure 2.4: Illustration of the anatomical regions of seven statistically significant differentially expressed hub nodes. Node 3 is located at the Right (R) Inferior Temporal (light blue), Node 9 at the Right Inferior Parietal (blue), node 10 at the Right Lingual Gyrus (purple), node 31 at the Right Lateral Occipital (red), node 42 at the Right Hippocampus (orange), node 64 at the Left (L) Putamen (yellow), and node 85 at the Left Cerebellum Gray Matter (GM) (green). Presented in radiological orientation with left shown on the right side.

the 1 hub node with 4 DWEs test where the modified DDT identified the hub with higher mean and lower TPR standard deviation for all simulations when compared with the base DDT. The simulations in Figure 2.6 present two important reinforcements of the modified DDT. The first result comes from the higher mean nodal TPR for the modified DDT at every point of every simulation type. This result shows the increased sensitivity of the modified DDT brought about by the BFMV algorithm. The second is the modified DDT's ability to profile data that is more physically relevant. In the hybrid simulations, using experimentally derived mean regional time series of normotensive participants, using the α =0.05 value used in our experimental analysis, the modified DDT maintained below nominal FPR values while obtaining a statistically significant improvement over the base DDT in mean TPR values. Thus, the modified DDT shows higher statistical power and increased accuracy compared to the base DDT in analyzing differential expression of resting-state functional connectivity.

To properly explain how the BFMV algorithm produces an effect on the DDT, an in-depth look at the statistical testing must be done. Starting with the null model generation step (Fig. 2.1), the BFMV algorithm is used to build a null model comprised of individual null matrices designed to match the mean and variance of the difference network. Typically, 1000 individual null matrices comprise a single null model used for statistical testing. After building the null model, it, along with the difference network and threshold value, is put into the binomial statistical test as illustrated in Figure 2.1. The testing process is comprised of three main steps: 1) calculating null probability, 2) building a bi-

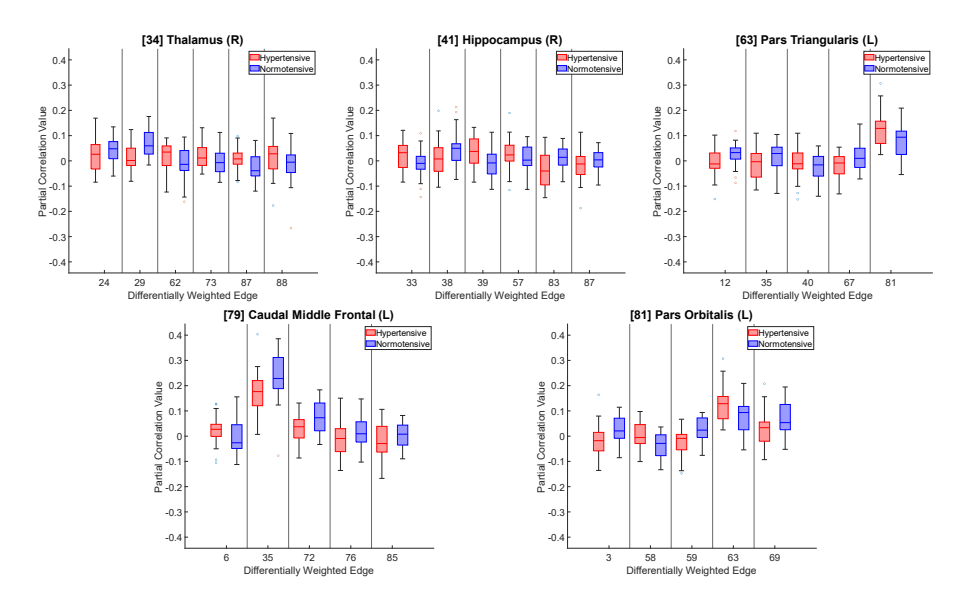


Figure 2.5: Group-segregated box plots of partial correlation values are shown for the seven differentially expressed hub nodes. The group's partial correlation value is listed on the y-axis while the x-axis represents different differentially weighted edges that hub node is connected to (Red: the hypertensive group; Blue: the normotensive group).

nomial distribution based on the null probability and 3) modeling of observed probability via a separate binomial distribution. It is step 1 and 2 of this process where the BFMV modification has an effect. The null probability represents the likelihood that every edge connected to a given node i would exhibit groupwise differences under the null hypothesis. The i^{th} node's null probability, \hat{p}_i^{null} , is calculated via the formula (Higgins et al., 2019)

$$\hat{p}_i^{null} = \frac{1}{U(N-1)} \sum_{u=1}^{U} \sum_{j \in \eta, j \neq i} \bar{a}_{ij}^{(u)}$$
(2.2)

where U is the total number of null matrices in the null model, N is the total number of nodes, η is the set of all nodes, and $\bar{a}_{ij}^{(u)}$ is the individual elements the u^{th} thresholded null matrix $\bar{\mathbf{A}}$. Once \hat{p}_i^{null} is obtained, the expected null nodal degree is modelled by Binomial $(N-1,\hat{p}_i^{null})$. The resulting matrix describes how likely a given node will have a specific nodal degree under the null hypothesis. If a less accurate null model is used during these calculations, the DDT will produce null probability values that may not accurately reflect the subtle topology present in the data. This is where the BFMV algorithm makes

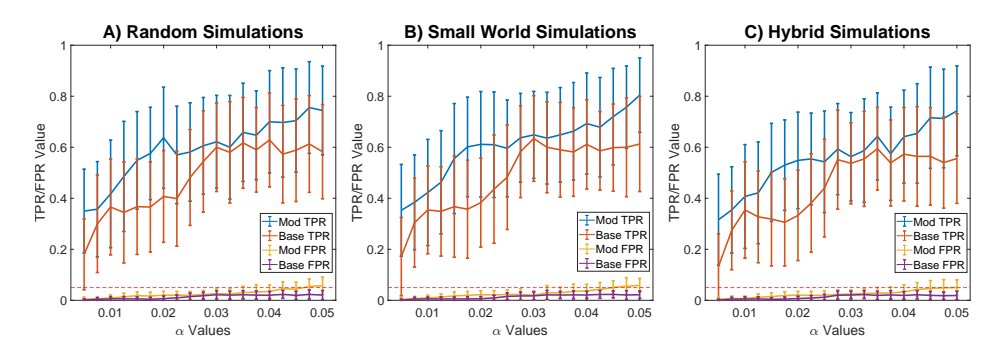


Figure 2.6: Modified (Mod) and Base difference degree test (DDT) mean true positivity rate (TPR) and false positivity rate (FPR) is shown for the random (6A), small world (6B), and hybrid (6C) simulation schemes. With the Mod TPR shown as a blue line, the Base TPR in red, Mod FPR in Yellow, and Base FPR in purple, the TPR and FPR values are shown as a function of α significance values. The bars shown on the lines represent a single standard deviation of the simulation over 100 trials.

its mark as it can more accurately profile the mean and variance of a difference network in comparison to the HQS algorithm used in the base DDT. Because the BFMV algorithm produces a more accurate null model when compared to the HQS algorithm, the resulting null probability and subsequent null binomial distribution is more accurate to the difference network. The result of this, as implied by Figure 2.6, is smaller nodal significance p-values. These lower p-values mean that, for a given significance value α , the modified DDT can more accurately identify hub nodes.

Modifying the null model generation algorithm from the HQS algorithm to the BFMV algorithm represents a meaningful change to the DDT. Through simulation, this change allowed us to find high TPR values with FPR still below the nominal 5% in nearly all aDDT simulations. The brute-force mean/variance matching algorithm was originally proposed as an alternative to the HQS algorithm in 2012 but, at the time, it was seen as too computationally expensive to implement. While the HQS algorithm has been widely used due to its computational efficiency, the BFMV algorithm does not meaningfully impact computation time in absolute terms (8 seconds for BFMV compared to the 0.5 seconds of HQS) and is worthy of further investigation to demonstrate its efficacy. Beyond demonstrating that the BFMV algorithm improves the DDT, these results further suggest the idea of other algorithms that could provide greater improvement to the null model generation. In theory, if an alternative algorithm could better match the difference network while also annihilating its internal struc-

ture it could further improve the TPR while decreasing FPR. Further pursuit of alternative null model generation algorithms will be left for future study.

The major shortcoming of the DDT modification is the elevated nodal FPR. This increased FPR is first notable in the results presented in Table 2 where eDDT produced nodal FPR values above the nominal 0.05 in all cases. After finding this increased FPR, we only used aDDT thresholding in further testing and recommend using aDDT thresholding in any future studies. Not only limited to the eDDT however, there is an observable increase in nodal FPR for aDDT simulations in the comparative analysis. While 24 out of 27 of the comparative tests performed showed aDDT producing mean nodal FPR values below the nominal (Figure 2.2), we must also acknowledge the large increase in FPR seen in the 5 hub, 11 DWE case (Figure 2.2C). Given the number of nodes in our system is defined as 35, the 5 hubs and 11 DWEs simulation represents a very noisy dataset where 9.24% of all unique connections could be listed as differentially weighted. While detecting 5 hubs is clearly within the bounds of what we can expect from experimental data, the increased experimental node count coupled with a median hub node degree of 5 means that this simulation represents an atypical dataset when compared to experimental results. The results of this simulation were notable as it emphasizes potential limits of the modified DDT.

When the modified DDT was applied to the experimental partial correlation data, it found 5 differentially expressed hub nodes and 26 unique significant connections. When the high mean TPR values and nominal mean FPR values seen in Figure 2.2C are considered within the context of Figure 2.3 showing the median nodal degree of 5 and 5 total hub nodes, it suggests that the simulations accurately profile expected results for the experimental data. This extrapolation is explored in the results shown in Figure 2.6 where, for experimentally analogous simulation parameters, the modified DDT exhibits increased TPR values for a given α value when compared to the base DDT. Taking all the results shown in the figures together, we claim that the experimental data is better profiled by our modified DDT than the base DDT.

There still remains a challenge when trying to draw conclusions based on experimental individual partial correlation values as seen in Figure 2.5. As neither group exhibits any simple trend when compared to the other, the underpinnings and underlying meaning of groupwise correlation differences warrants further investigation. While groupwise partial correlation values require more study, the results shown in Figure 2.3 show similarities to previous studies. A previous hypertension study (Shah et al., 2021) showed rsFC disruptions associated with the default mode network. We were able to detect a groupwise

difference in one of the regions of the default mode network, the hippocampus (node 41), between the two groups which is a reinforcement of the previous findings. However, we were unable to find disruptions in the dorsal attentional network as has been reported by other previous studies (Carnevale et al., 2020). While the study does show lateralization in the functional connectivity data reported as we have shown here, our findings do not further reinforce the study's other findings. This discrepancy could come from several sources, but it likely comes from the use of different statistical testing of the data. Whereas we use the DDT, the previous study used a general linear model to perform its correlation analysis.

Further exploration of the resting state differences discussed in this study should be performed to reinforce the claim posited that hypertension leads to changes in rsFC specifically in regions implicated in the default mode network. Furthermore, development of alternative null model generation algorithms to better match the difference network could theoretically reduce simulation FPR while maintaining high TPR and is likely to improve simulation results. Lastly, the application of the DDT could be further expanded to find differential expression of regions of the brain in a myriad of disease states.

2.6 Conclusion

With an estimated 1.28 billion people worldwide living with hypertension, studying how the disease affects the brain is vitally important. The current study evaluated resting state fMRI data and found evidence that the functional connectivity patterns in the hypertensive group differed from that observed in the normotensive group. Methodologically, this study is both a reinforcement and refinement of the findings of the base DDT. Verified by three simulated data types, the results presented in this study demonstrate promise for the application of the DDT in the analysis of groupwise differences. While the nodal FPR is higher than that in the previous study, we at least matched or, in most cases, improved upon the TPR in all comparative simulations performed. This simulation result leads us to have high confidence in our experimental results that found 5 hub nodes and 26 unique DWEs differentiating the hypertensive and normotensive group. These experimental findings point to possible functional connectivity changes associated with hypertension in the default mode resting state network. Going forward, we expect that the modified DDT will be used in many rs-fMRI studies and will allow for high statistical power analysis of differentially expressed regions of the brain.

2.7 Author Contribution Statement

William D. Reeves: Methodology, Software, Validation, Formal analysis, Writing – original draft, Visualization Ishfaque Ahmed: Methodology. Brooke S. Jackson: Conceptualization, Validation, Writing – review & editing. Wenwu Sun: Methodology. Michelle L. Brown and Celestine F. Williams: Investigation, Resources. Catherine L. Davis: Validation, Writing – review & editing, Supervision. Jennifer E. McDowell: Conceptualization, Writing – review & editing, Supervision, Project administration, Funding acquisition. Nathan E. Yanasak: Validation, Resources, Data Curation, Writing – review & editing, Project administration. Shaoyong Su: Conceptualization, Writing – review & editing, Supervision, Project administration, Funding acquisition. Qun Zhao: Conceptualization, Validation, Writing – review & editing, Supervision, Project administration.

CHAPTER 3

FMRI-BASED DATA-DRIVEN BRAIN PARCELLATION USING INDEPENDENT COMPONENT ANALYSIS

3.1 Abstract

3.1.1 Background

Studies using functional magnetic resonance imaging (fMRI) broadly require a method of parcellating the brain into regions of interest (ROIs). Parcellations can be based on standardized brain anatomy, such as the Montreal Neurological Institute's (MNI) 152 atlas, or an individual's functional activity patterns, such as the Personode software.

3.1.2 New Method

This work outlines and tests the independent component analysis (ICA)-based parcellation algorithm (IPA) when applied to a hypertension study (n = 48) that uses the independent components (ICs) output from group ICA (gICA) to build ROIs which are ideally spatially consistent and functionally homogeneous. After regression of ICs to all subjects, the IPA builds individualized parcellations while simultaneously obtaining a gICA-derived parcellation.

3.1.3 Results

ROI spatial consistency quantified by dice similarity coefficients (DSCs) show individualized parcellations exhibit mean DSCs of 0.69 ± 0.14 . Functional homogeneity, calculated as mean Pearson correlation value of all voxels comprising a ROI, shows individualized parcellations with a mean of 0.30 ± 0.14 and gICA-derived parcellations' mean of 0.38 ± 0.15 .

3.1.4 Comparison with Existing Method(s)

Individualized Personode parcellations show decreased mean DSCs (0.43 \pm 0.11) with the individualized parcellations, gICA-derived parcellations, and the MNI atlas having decreased homogeneity values of 0.28 \pm 0.14, 0.31 \pm 0.15, and 0.20 \pm 0.11 respectively.

3.1.5 Conclusion

Results show that the IPA can more reliably define a ROI and does so with higher functional homogeneity. Given these findings, the IPA shows promise as a novel parcellation technique that could aid the analysis of fMRI data.

3.2 Introduction

Neuroimaging studies using magnetic resonance imaging (MRI) often require the use of brain parcellation techniques. Brain parcellations, also known as atlases, allow for the segmentation of the brain into different regions of interest (ROIs) that can be used to study changes in the brain. Parcellations can be based on the specific anatomical features of the brain, collectively referred to as anatomical parcellations, or based on brain activation patterns quantified by functional MRI (fMRI) data, referred to as functional parcellations. The decision of which parcellation to use is made based on the goals of the study. Whatever the chosen method may be, brain parcellations can be found ubiquitously throughout the field of neuroimaging, including studies focusing on network analysis (Bullmore & Sporns, 2009; Melie-García et al., 2013; J. Wang et al., 2010), studies focusing on white matter tract differences (Y. Li et al., 2013; Lu et al., 2020), changes in cerebral volume (Terribilli et al., 2011), or those examining cerebral blood flow (S. Hu et al., 2019; B. P. Thomas et al., 2013).

The consideration of which parcellation is appropriate for use is often a foregone conclusion. Studies frequently use the Montreal Neurological Institute (MNI) (Mazziotta et al., 1995) anatomical parcellation, which serves as the default for many. Use of the MNI atlas includes studies following the minimal processing guidelines for the human connectome project (HCP) (Glasser et al., 2016), and is the default for researchers using statistical parametric mapping (SPM) (Penny et al., 2007), and FMRIB software library (FSL) (Smith et al., 2004) tools. There are other anatomical atlases available for use, such as the Chinese2020 atlas (P. Liang et al., 2015) or the techniques proposed to profile Korean and east Asian brains (J. S. Lee et al., 2005). These atlases could also be computed based on the structural scans by using tools such as the Automated Anatomical Labelling atlas (AAL) (Tzourio-Mazoyer et al., 2002) with the newest being AAL3 (Rolls et al., 2020), the Computational Anatomy Toolbox (CAT) (Gaser et al., 2022), or the Individual Brain Atlas using Statistical Parametric Mapping (IBASPM) (Alemán-Gómez et al., 2006; Gaser et al., 2022; Tzourio-Mazoyer et al., 2002). While many studies are based on anatomical parcellations, there have been several advances in the computation of parcellations based on fMRI. Functional parcellations can be based on spectral clustering (Craddock et al., 2012), boundary mapping (Gordon et al., 2014), consensus clustering (Ryali et al., 2015), density peak clustering (Luo et al., 2020), instantaneous connectivity patterns (van Oort et al., 2018), or other techniques (Arslan et al., 2018). In a comprehensive review of contemporary parcellation methods (Eickhoff et al., 2018), it was stressed that there is no gold-standard of parcellation. All parcellation methods, whether they are based on functional or structural attributes, add together to obtain the topographical information of the brain. The proposed method is therefore not attempting to show its material superiority over anatomical parcellation, but rather to show a step forward in functional parcellation methodology.

While there are different approaches for obtaining functional parcellations, this work focuses on employing independent component analysis (ICA) to define cortical and subcortical ROIs. The primary method of comparison is Personode, a MATLAB toolbox designed for semi-autonomous classification of ICA components (see Pamplona et al., 2020) that allows for the building of group and individualized parcellations based on canonical human resting state networks (RSNs). The proposed method differs from Personode in that it defines smaller scale ROIs without enforcing any shape constraints. We propose the ICA-based parcellation algorithm (IPA) that takes the independent components (ICs) output from group ICA (gICA), classifies them into ROI candidates, and produces both a single gICA-derived group atlas as well as individualized atlases based on dual-regression of gICA results.

The IPA was designed with two goals in mind. The first goal of the IPA was to build individualized atlases with spatially consistent ROI definitions. While the individuals are expected to exhibit slight differences in the location of a ROI, the IPA should consistently define a ROI in a specific region of the brain for each subject. The second goal of the IPA was to build ROIs that are functionally homogenous. As has been discussed in previous work (see Craddock et al., 2012; Gordon et al., 2014; Han et al., 2021; Thirion et al., 2006), these types of data-derived parcellations should encompass regions that are internally functionally homogeneous.

To assess and contrast their efficacy, Personode and the IPA were applied to an experimental resting-state fMRI (rs-fMRI) dataset taken from a hypertension study performed on 48 middle-aged adult humans exhibiting either normal or elevated blood pressure. For this evaluation, IPA and Personode spatial overlap and ROI consistency was quantified by dice similarity coefficient (DSC), with ROI sizes, and ROI homogeneity being used to further profile the ROIs produced by each method. In addition to comparing the two parcellation methodologies, the DSC, ROI sizes, and homogeneity values also allowed for a comparison between the hypertensive and normotensive individuals. These comparisons were used to compare not only different methodologies, but also how a test group affects the results of those methodologies. The parcellations produced by the IPA are co-registered to a reference subject's rs-fMRI data. The output of this process is designed to be a drop-in alternative to current anatom-

ical or functional parcellations for the researcher. For studies already using the MNI parcellation, the process can also output ROIs with the same numerical labels as the MNI152 atlas. However, the IPA is model agnostic and can be adapted to fit other labelling schemes. The process described here is applied to human data, but it could be adapted for use in any model system.

3.3 Materials and Methods

3.3.1 Individual data acquisition and preprocessing

The experimental data consisted of 48 total participants (a mean of 40.4 ± 3.0 years, with 22 males, 26 females, 17 Caucasian, and 31 African American participants) divided into two groups. One group of individuals that self-report ongoing treatment or meet the criteria (blood pressure over 130/80 mmHg) for hypertension (HTN, n = 26), and another group of normotensive individuals (NRM, n = 22). Each participant underwent rs-fMRI and 3D MR structural scanning on a Siemens 3T Magnetom Vida MRI scanner (Siemens Health Solutions, Malvern, PA) at Augusta University. Resting state fMRI scans (2D-Gradient echo EPI sequence, 48 slices, TR=1200ms, TE=33.00ms, FA=57°, FOV=240x240 mm2, matrix=120x120, slice thickness=3mm, 500 total volumes) were acquired using a BioMatrix Head/Neck 20-channel receive coil. Structural images were also acquired, using a sagittal 3D scan (MPRAGE, 176 slices, TR=2300ms, TE=2.43ms, FA=9°, FOV=270x270mm2, matrix=240x256, slice thickness=1.2mm).

Data preprocessing was performed using the Statistical Parametric Mapping 12 (Penny et al., 2007) toolkit with MATLAB 2021b (MathWorks, Natick, MA). Preprocessing steps included masking, unwarping, slice timing correction, and registration to a reference participant. Group independent component analysis was performed by FMRIB software library's (FSL) (Smith et al., 2004) MELODIC software on normotensive individuals. For data of hypertensive individuals, FEAT low-level preprocessing was done to prepare the data for dual-regression.

3.3.2 Building group and individualized atlases via IPA

The ROIs found through IPA depend on ICA, which falls underneath a larger umbrella term of blind signal segmentation (BSS). Broadly speaking, BSS techniques model observations as a mixture of underlying signals (Naik & Kumar, 2011). ICA accomplishes this task of identifying individual signals by assum-

ing a given set of N observations $[x_i(t)]$ and underlying signals $[s_i(t)]$ can be expressed as $\mathbf{x}(t) = \mathbf{A}\mathbf{s}(t)$ where A is referred to as the mixing matrix (Naik and Kumar). Simply put, ICA seeks to solve the mixing matrix by estimating the underlying signals with the assumptions that they are statistically independent and of a non-Gaussian distribution. In the case of the experimental data, MELODIC solved for 250 ICs during the gICA. The 250 components from gICA are used as the building blocks for determining ROIs through IPA in that they are used to find which ICs may show spatial overlap with anatomical regions. Furthermore, dual-regression requires the ICs from gICA to be used as the basis in defining an individual's analogous IC. ICA represents the foundation from which the IPA is built.

The IPA was defined by seven stages shown in Figure 3.1. The first stage was smoothing and thresholding of the ICs. In this stage, all ICs had a Gaussian smoothing filter applied with a standard deviation of 1.25. The smoothed volumes were thresholded to remove negative values and to select out highactivation voxels. The second stage of the IPA involved calculation of spatial Pearson correlation values. In the case of our data, spatial Pearson correlation analysis was performed between all ICs and every MNI region. This analysis resulted in a $M \times N$ (# MNI ROI by # ICs) matrix of correlation values bounded between -1 and 1 where higher values indicated increased signal intensity and spatial overlap between two regions. Stage three of the IPA, referred to as candidate IC selection, used the correlation matrix from stage 2 to rank the highest values per MNI region. The IPA then applied a percentile threshold to spatial Pearson values which produced a list of candidate ICs highly corresponding to MNI regions. Different spatial Pearson threshold percentiles were trialed, but ultimately assigning the threshold at the 60th percentile produced a reasonable number of ROIs while also choosing only those ICs that highly correspond to the anatomical reference. The fourth and fifth stages of the IPA involved Fisher z-score transformation of the data and subsequent z-score thresholding respectively. A z-score of 3.0 was chosen as it provided high selectivity while also producing ROIs of reasonable size. The outputs from this stage were spatially disconnected clusters of voxels that showed large activations in the original IC which required further processing to address the discontinuity of clusters across the brain. The sixth stage of the IPA involved ensuring that the ROI definition was spatially continuous with the area of greatest activation. The first step of this was to find the max activation voxel (MAV), where ROIs were first masked by a left/right (L/R) hemisphere mask to ensure the proper side was selected with defining the MAV. After finding the MAV from the L/R masked ROIs, the algorithm calculated the position of all voxels still present in the ROI. A continuity algorithm was run that started at the MAV and spread out in all directions until all voxels connected to the MAV were selected. This ensured that all ROIs were defined by the MAV and only contained spatially contiguous regions. The seventh stage of the IPA was ROI binarization that set all non-zero values of an ROI to a specific value.

While the gICA-derived IPA parcellations undergo all 7 stages of processing, the individualized parcellations do not undergo candidate IC selection (stage 3 in Fig.3.1). Through candidate IC selection as performed on gICA data, the IPA obtains a list of IC labels that spatially overlap with specific anatomical regions. The IPA then uses this list of IC labels along with individualized results from dual-regression to define individualized parcellations. This allows the IPA to build parcellations that are consistent in both the number of ROIs defined as well as the spatial distribution of ROIs across individuals.

In the case of overlapping ICs, the IPA employs a winner-takes-all strategy. Through IC candidate selection, the IPA obtains a list of unique candidate ICs (no ICs are chosen twice for different ROIs), the anatomical region the ICs most closely correspond to, and the spatial Pearson value of the ICs with that corresponding anatomical region. The list of candidates is ranked according to their spatial Pearson value, and the IPA iteratively moves down the list building ROIs based on the selected IC's activation scheme. As the IPA moves down the list, any previously defined ROI's voxels are removed from any newly defined ROI. This results in ICs that better profile the underlying anatomical reference being chosen as the winner in a head-to-head contest with ICs that may exhibit overlapping activation schemes.

3.3.3 Quantifying the Parcellations

To profile the performance of the IPA in comparison to other methods, several quantifications of the parcellations are obtained. The quantifications described below either profile the performance of the parcellation algorithm (dice coefficients, homogeneity), or profile differences present in the data that are detected by using the IPA (two-sided t-test, Wilcoxon rank-sum test, difference degree test).

Spatial Consistency via Dice Similarity Coefficient

One of the stated goals of the IPA is to produce parcellations with consistent spatial definitions. Spatial consistency is measured by the dice similarity coefficient (DSC). The DSC is a number between 0 and 1 that relates to how much

Obtaining ICA-based Parcellation Algorithm ROIs

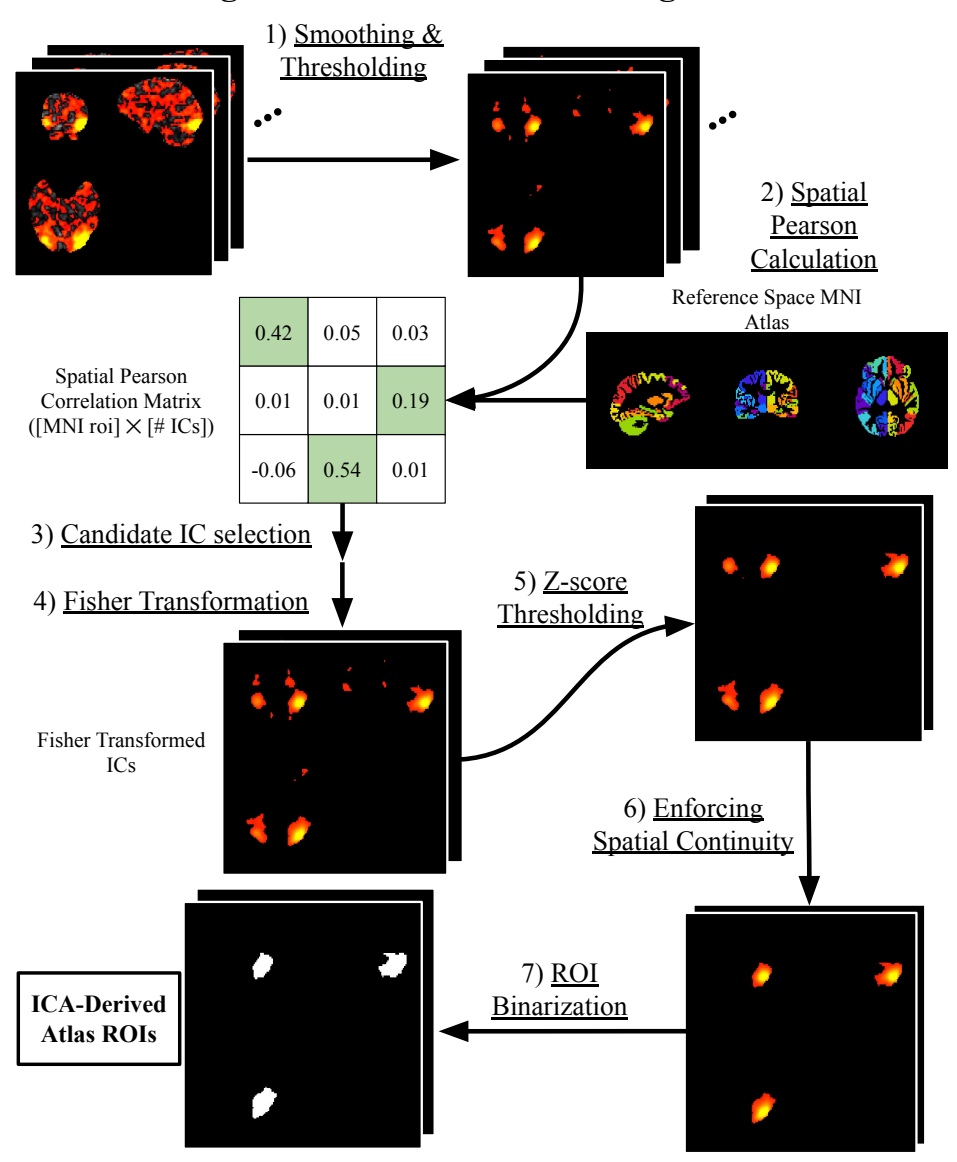


Figure 3.1: Overview of atlas region of interest (ROI) processing and selection. Starting from raw group independent component analysis (gICA) independent components (ICs), initial thresholding and data smoothing is performed. The smoothed components are then, IC-by-IC and region-by-region, compared against the Montreal Neurological Institute (MNI) atlas previously processed to be in reference-subject space to build a $M \times N$ spatial Pearson correlation matrix that can be used to identify which ICs highly correspond to specific regions in the brain. These selected ICs are then Fisher transformed and further processed via z-score thresholding to obtain ICs with high activation values. Using the max activation voxel (MAV) of the IC, spatial continuity is then enforced followed by binarization of the IC to build atlas ROIs.

overlap there is between two matrices. The DSC of two matrices A and B is calculated by

 $DSC = \frac{2|\mathbf{A} \cap \mathbf{B}|}{|\mathbf{A}| + |\mathbf{B}|}$ (3.1)

where the |X| notation refers to the number of elements present in the given matrix X. A DSC of o means that the two matrices have zero elements in common whereas a DSC of I means that the two matrices perfectly overlap with each other.

DSCs are often used as an alternative to a spatial Pearson correlation as they perform a similar role in quantifying spatial overlap. The difference between the DSC and the spatial Pearson value is that the DSC is a purely binary comparison metric. This means that the value of the overlapping elements plays no role in the determination of the score whereas the spatial Pearson correlation considers the intensity of the common entries. For each ROI, the spatial consistency analysis computed the pairwise DSC for a given ROI between two individuals. This process of pairwise DSC calculation was repeated across all ROIs and individuals to find how consistent the ROI definition was. This process was done for both the individualized IPA parcellations as well as the individualized Personode parcellations.

ROI Functional Uniformity by Homogeneity

The second main goal of the IPA was to define ROIs that exhibited similar functional activation patterns. To measure how similar the voxels comprising a region were, homogeneity values were calculated. The homogeneity values of a region were calculated as the average Pearson correlation value between all voxels in each ROI. This involved extracting the timeseries of each voxel inside of a ROI, performing Pearson correlation analysis on the resulting matrix, and averaging all elements of the correlation matrix. Alternatively stated, an individual's i^{th} ROI homogeneity value (h_i) is calculated using the equation below

$$h_i = \frac{1}{V} \sum_{j,k}^{V} r_{j,k} = \bar{r}_i \tag{3.2}$$

where V is the number of voxels in the ROI and $r_{j,k}$ is the Pearson correlation value between two voxelwise timeseries j and k. This process finds a homogeneity value for each ROI and each individual.

Homogeneity represents both a metric to quantify the IPA as well as a metric of comparison between parcellation methods. We hypothesize that an atlas based on functional activation would produce ROIs that are internally homo-

geneous in that the voxels of the ROI would all be functionally similar (Thirion et al., 2006). This means that we can compare the performance of the IPA against the other methods using homogeneity.

Groupwise Differences in Homogeneity Through Statistical Testing

To further profile what differences may be seen in the IPA, the two-sided t-test and Wilcoxon rank-sum test were applied to groupwise homogeneity. These two tests profile statistically significant differences found between two sets of observations. The differentiating factor between them is that the two-sided t-test assumes that the samples come from a normal distribution while the Wilcoxon rank-sum test does not. Because the two tests have different underlying expectations they allow for an extra avenue of comparison of the results.

Functional Connectivity Differences Using a Difference Degree Test

The difference degree test (DDT) (Higgins et al., 2019) is a type of statistical test that can be applied to groups of subjects to detect differences in functional connectivity patterns. Generally, the DDT attempts to find connections (edges) between regions (nodes) that show differential expression between groups. If a node has a significant number of differentially weighted edges (DWEs) attached to it, it is referred to as a differentially expressed hub node which could warrant further study. One of the outputs from the DDT is a list of p-values representing how certain the test is of nodal differential expression. The default setting for establishing significance in these values is a value of $\alpha=0.05$.

Finding groupwise differences using graph theory can be a challenging task for those using a lower number of ROI in their analyses. The challenge comes from lower dimensional graphs being highly sensitive to the loss or gain of connections as well as the statistical power loss of having fewer samples in the data. To examine the role this plays in groupwise analyses via the DDT, the number of ROIs in IPA parcellations was increased from 35 to 44 in total. To achieve this, the spatial Pearson threshold was changed from the 60th (Sec. 3.3.2) to 50th percentile of values.

3.4 Results

The proposed IPA and the Personode toolbox were applied to the experimental resting-state fMRI dataset to assess and contrast their efficacy in terms of DSC, ROI sizes, and ROI homogeneity values. The results of the IPA and Personode

along with the MNI152 anatomical atlas were further tested via statistical tests and the DDT.

3.4.1 Individualized Spatial Overlap and ROI Size Consistency

IPA parcellation examples are seen in Figure 3.2. For each subject, the IPA defined 35 ROIs while Personode defined 21 ROIs. To quantify ROI overlap, DSC values for both methods are profiled in Figure 3.3. The DSCs reported in Figure 3.3 represent a selection of all ROI's DSC consisting of the intragroup comparison of all ROIs. As shown in the figure, the IPA shows higher mean intra-group DSCs as compared with Personode with a mean normotensive DSC of 0.70 ± 0.13 versus 0.47 ± 0.16 and a mean hypertensive DSC of 0.68 ± 0.14 compared with 0.45 ± 0.15 . Looking at all DSCs for all subjects, IPA shows a mean of 0.69 ± 0.14 with Personode having an average of 0.43 ± 0.11 . For both groups using the IPA ROI definitions, there is a spike in the DSC values at zero that corresponds to regions that do not overlap with other individualized atlas ROI. A single ROI was constructed without overlap to other individuals for one normotensive and three hypertensive individuals. These mismatched ROIs represent 0.2% of all 1680 individualized IPA ROI definitions.

Further analysis of ROI sizes is shown in Figure 3.4. Figures 3.4A and 3.4B show the size distributions of the normotensive (left violin) and hypertensive (right violin) individuals as half-violin plots as well as the group-averaged ROIs as inverted triangles. Overall, Personode ROI definitions are more consistent in their sizes as compared to the IPA. As shown in Figure 3.4B, network subparcellation - shown as multiple inverted triangles in network - sizes exhibit a tight grouping around the group-averaged sub-parcellation sizes. When looking at the IPA (Fig.3.4A), it is shown that there is a much greater variation in ROI sizes as compared with Personode with the difference in size between individualized and group-derived ROIs being much greater in the IPA. Notably, the MNI anatomical ROIs are of a much larger size as compared to the functional parcellations.

When taking the DSCs and ROI sizes together and comparing to Personode, the IPA shows more consistency in the location of the ROI but less consistency when defining the size of the ROI. Both functional parcellation techniques also show much smaller ROI definitions when compared with the MNI parcellation.

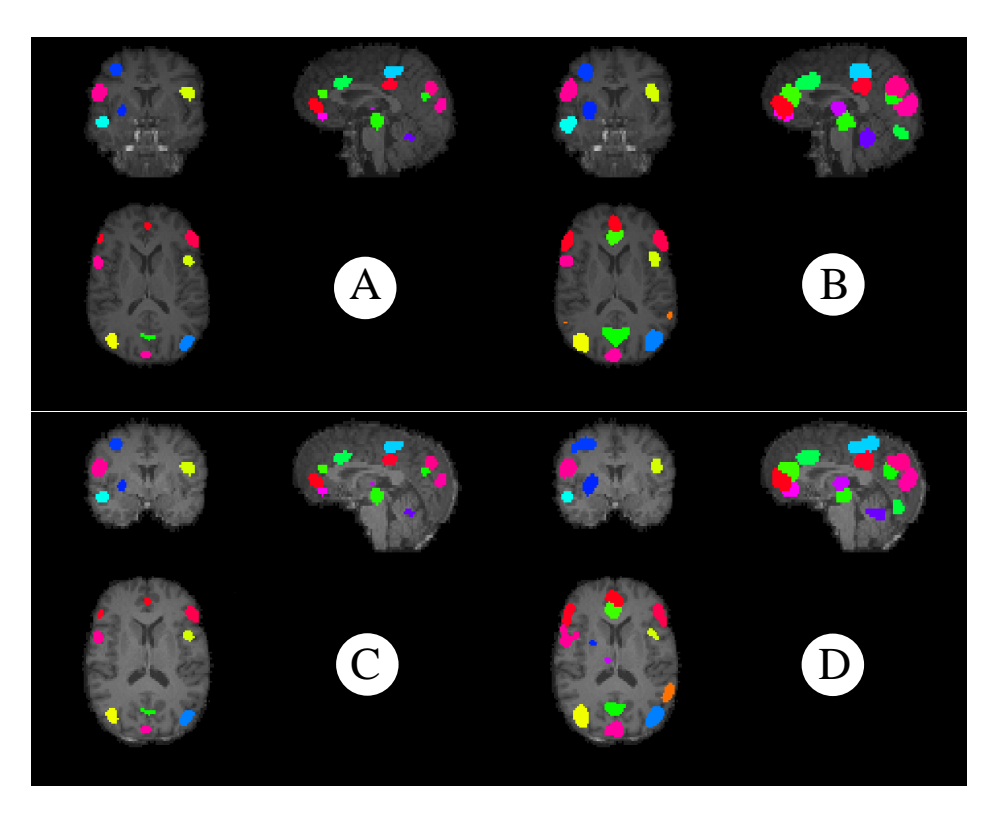


Figure 3.2: Visualizations of example IPA parcellations. The first column (2A/2C) shows the group independent component analysis (ICA) derived parcellations whereas the second (2B/2D) demonstrates the individualized parcellations. The top row (2A/2B) visualizes parcellations in a normotensive individual while the bottom row (2C/2D) exemplifies the parcellations in a hypertensive individual. Each parcellation is overlaid atop the specified subject's structural T1 data that has been co-registered to fMRI space. The colors present in the parcellation represent the different ROIs defined by the ICA-based parcellation algorithm (IPA) and are consistent across all examples.

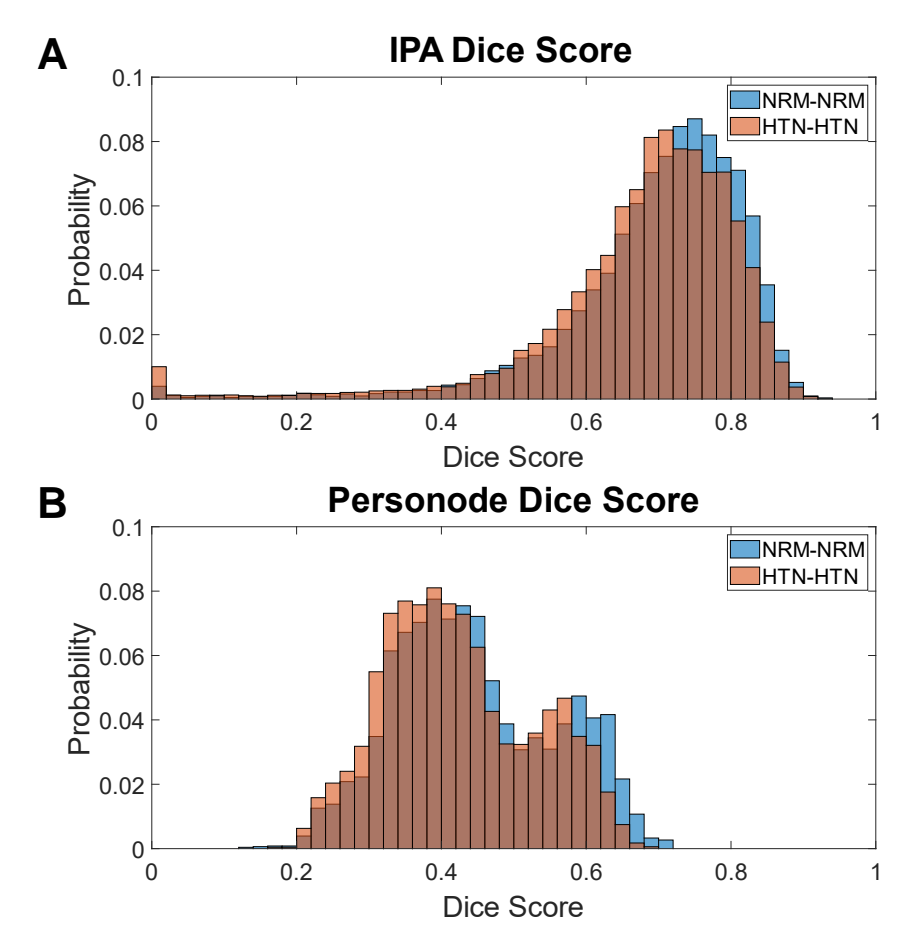


Figure 3.3: Intragroup dice similarity coefficient (DSC) distributions of the independent component analysis-based parcellation algorithm (IPA) and Personode individualized parcellations. The data is shown separated into their groups of either normotensive (NRM – blue) or hypertensive (HTN – orange) individuals. The DSC represents the simple spatial overlap of two ROI and is used in this context to quantify the consistency of their definitions. Each DSC is calculated as the overlap between a specified ROI across each subject. Figure 3.3A shows the DSC distribution for the IPA and Figure 3.3B shows the same information for Personode.

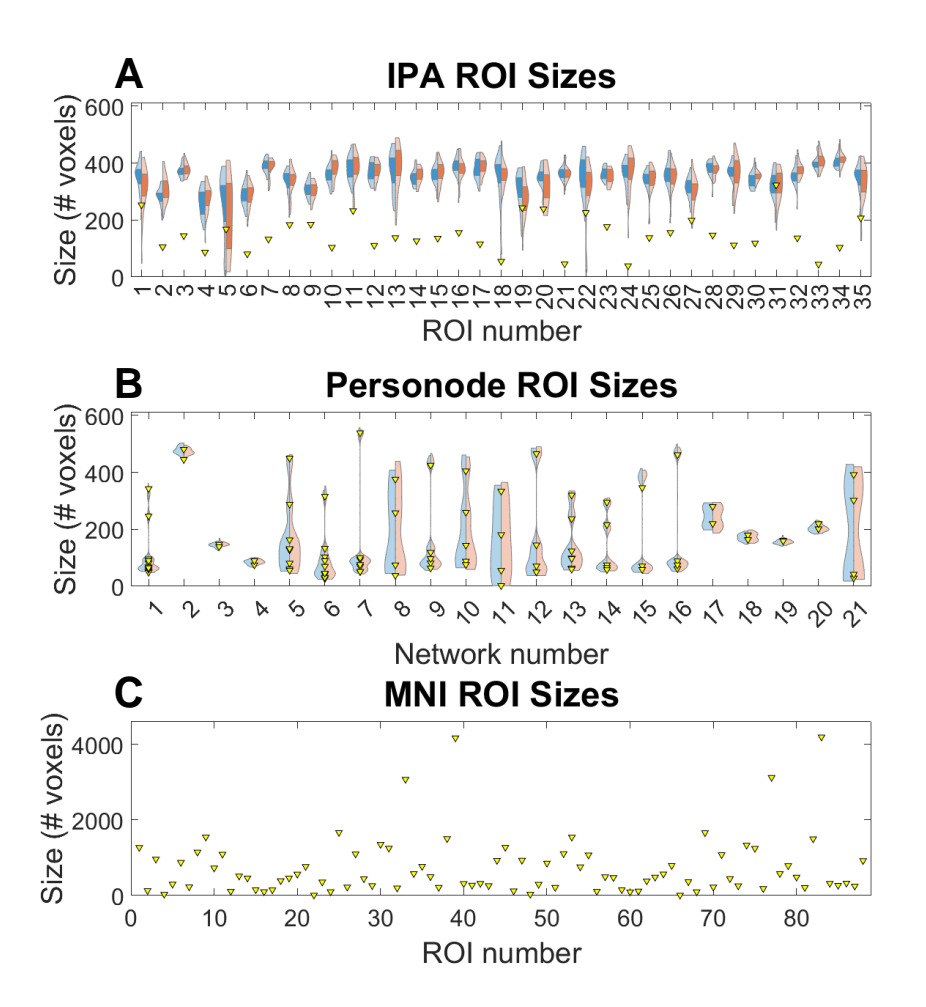


Figure 3.4: Parcellation region of interest (ROI) size distributions. Individualized parcellation size distributions are shown in the violin plots with the group-derived parcellations being shown by the downward facing triangles in (3.4A, 3.4B). The individualized parcellation ROI size distributions are further broken down into groups with the NRM being the left side of the violin plots shown in light blue and blue, and the HTN being the right side of the violin plots shown in light orange and orange. For Personode sub-parcellations, the violin and scatter plots represent the distribution for each sub-parcellation of a given network. MNI gray matter ROI sizes are shown in 3.4C.

3.4.2 Homogeneity Comparison

A comparison of parcellation homogeneity values can be seen in Figure 3.5 below showing all homogeneity values calculated across every individual separated into their respective hypertension status. In comparing the individualized parcellations from the IPA (Fig.3.5A) and those from Personode (Fig.3.5C), the homogeneity values are similar in their distribution. The normotensive individuals (left violins) show slightly elevated 75th percentiles as compared to the hypertensive individuals (right violins) in Figure 3.5A whereas 3.5C shows a more consistent distribution across the groups. The group-averaged parcellation homogeneity values shown for the IPA (Fig.3.5B) and Personode (Fig.3.5D) both show an elevated distribution to their values as compared with their individualized counterparts while showing similar distribution patterns to them. Normotensive individuals again appear to have elevated 75th percentiles to their data as compared to the hypertensive individuals in the IPA while Personode parcellation values show similar distributions across the groups.

3.4.3 Groupwise Testing

Application of the two-sided t-test produced no groupwise differences between any of the methods tested. When the Wilcoxon rank-sum test was applied to all parcellation methods, IPA gICA-derived parcellation ROI 10 – located at the right middle temporal – showed statistical significance with a p-value of 0.0290 with no other ROIs or methods showing any significance ($\alpha = 0.05$). The MNI homogeneity values show the lowest distributions compared with both the individualized and group-averaged functional parcellations. These holistic findings are quantified in the statistics found in Table 1 below where the homogeneity values seen in Figure 3.5 have been averaged by group to show groupwise trends in the data. As seen in Table 1, IPA parcellations exhibit slightly increased homogeneity values as compared with the Personode parcellations, while the structural MNI parcellations showing the lowest homogeneity values; Meanwhile, normotensive parcellations show higher homogeneity values when compared with the hypertensive parcellations. The DDT was applied to both the IPA and Personode parcellations. The DDT produced no significant hub nodes for the IPA at the default significance level of α = 0.05 as seen in Figures 3.6A and 3.6B. Performing the same analysis using the Personode parcellations also produced no significant hub nodes.

When the number of ROIs was increased from 35 to 44, the gICA-derived and individualized parcellations showed 1 and 2 hub nodes respectively. These

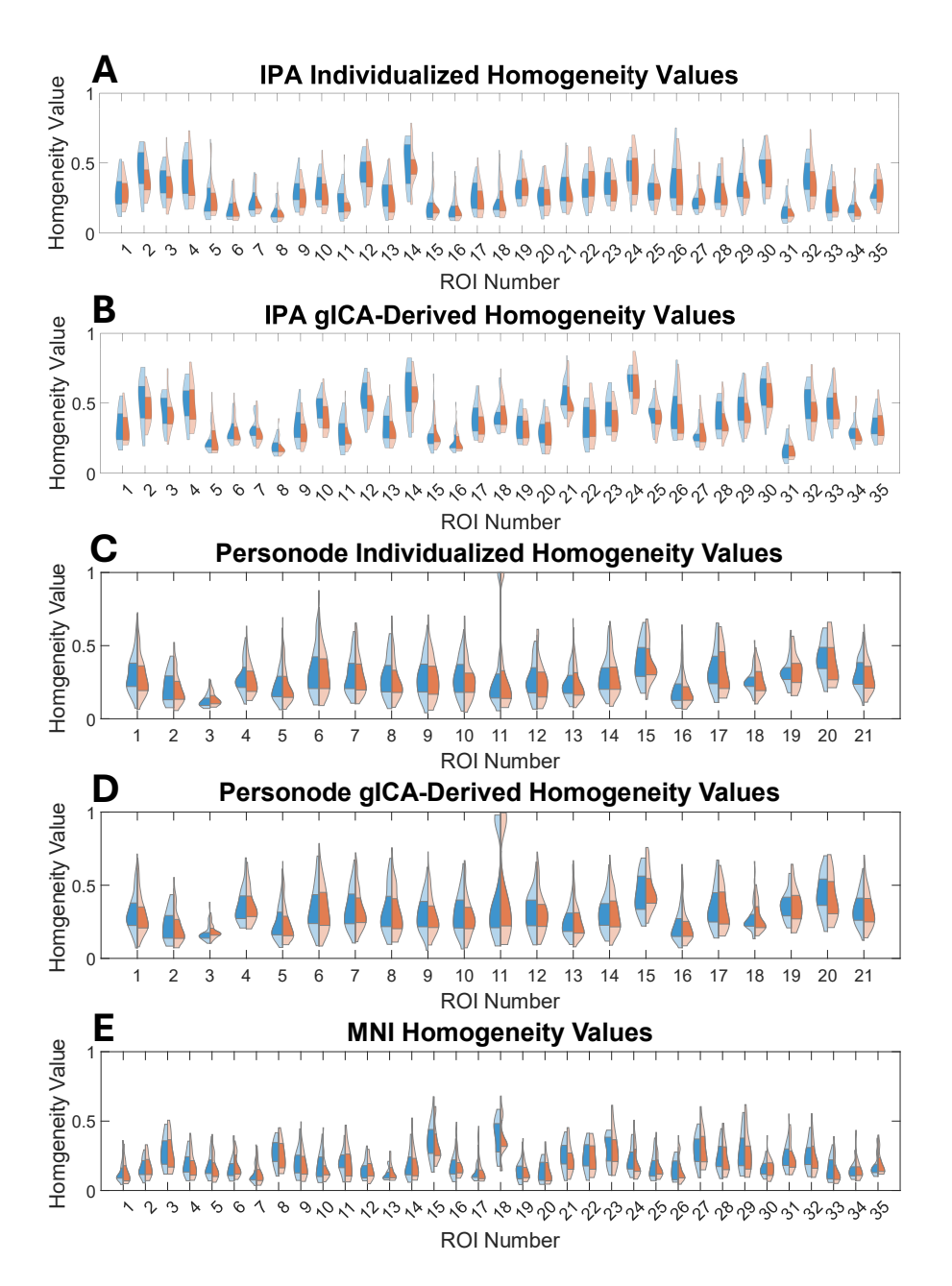


Figure 3.5: All models' parcellation homogeneity values are shown as violin plots where the 25th and 75th percentiles are shown as shaded areas of the violins. Individualized parcellations from the independent component analysis-based parcellation algorithm (IPA) and Personode models are shown in Figures 3.5A and 3.5C respectively with their group independent component analysis (gICA) derived parcellation counterparts are shown in Figures 3.5B and 3.5D. Figure 3.5E presents the 35 IPA-analogous Montreal Neurological Institute (MNI) regions being shown in Figure 3.4E. For each method, the violin plots were further subdivided into left and right violins with the left violins shown in light blue and blue representing the normotensive individuals and the right violins shown in light orange and orange representing the hypertensive individuals.

hub nodes are shown in Figures 3.6C and 3.6D below where their nodal degree and the significance level are shown overlaid on each other. The labels for these parcellations can be found in the appendix (Table A.I). The two methods share a hub node detected at the left rostral middle frontal portion of the brain (node #25 in Fig. 3.6C/D) and the individualized parcellation shows the same node (#25) and an additional hub node corresponding to the right caudal middle frontal area (node #17 in Fig. 3.6D).

Table 3.1: The mean and standard deviation of all homogeneity values shown in Figure 3.4 are shown in the table below with a breakdown of the statistics per group. As the Montreal Neurological Institute (MNI) parcellation is not derived from ICA data, it is not counted as a group-independent-component-analysis (gICA)-derived parcellation denoted by the double line.

	Homogeneity							
		gICA-derived		Individualized				
Parcellation	MNI	IPA	Personode	IPA	Personode			
Overall	0.20	0.38	0.31	0.30	0.28			
	± 0.11	± 0.16	± 0.15	± 0.14	± 0.14			
Normotensive	0.20	0.39	0.32	0.30	0.29			
	± 0.11	± 0.16	± 0.15	± 0.14	± 0.14			
Hypertensive	0.20	0.38	0.31	0.29	0.28			
	± 0.11	± 0.15	± 0.15	± 0.14	± 0.15			

3.5 Discussion

The first stated goal of this study is to build individualized ROIs that are consistent in their spatial definition. The proposed IPA accomplishes this goal with elevated DSCs as compared to Personode. As shown in Figure 3.3A, IPA ROI definitions show high consistency with intra-group DSC being 0.70 and 0.68 for the normotensive and hypertensive groups respectively. When compared with the Personode DSCs as seen in Figure 3.3B, the IPA clearly shows higher consistency in ROI definition. With mean intra-group DSCs of 0.45 and 0.42 for the normotensive and hypertensive individuals, Personode exhibits less consistency in network definition as compared to the IPA using these data.

This depression and bimodality of Personode DSCs likely comes from two sources. First, the ROI definition step relies on a priori anatomical information to define the ROI. Personode multiplies RSN templates and ICs together to obtain a weighted probability map of the RSN which, when selecting the

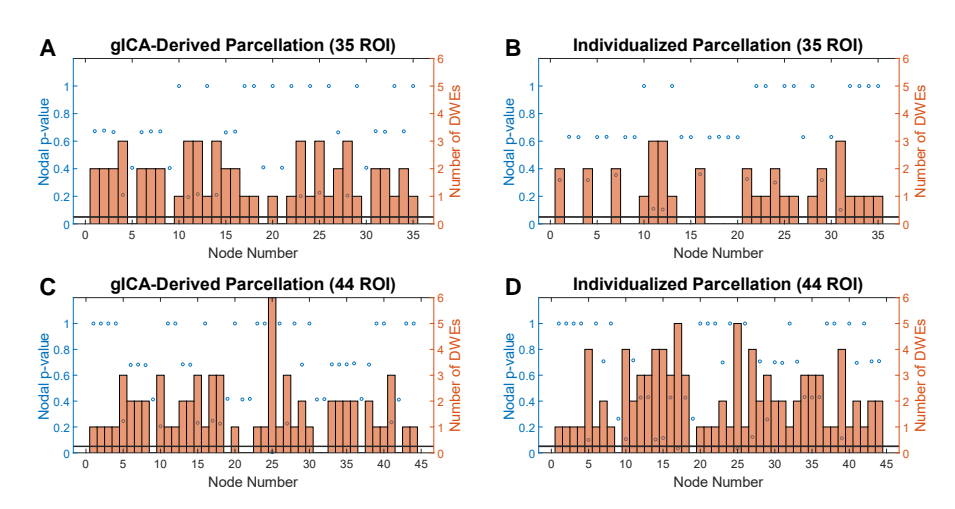


Figure 3.6: The nodal p-values and number of differentially weighted edges (DWEs) are shown in the plots above for different trials of the difference degree test (DDT) using different IPA parcellations. In each plot, the blue circles represent the nodal p-value while the orange bar plots represent the number of DWEs attached to each node. 3.6A shows the DDT findings when using the group independent component analysis (gICA)-derived IPA parcellations with 35 total ROI definitions, and 3.6B shows the same information for the individualized parcellations. Figures 3.6C and 3.6D show the DDT results when the number of ROIs increased to 44 for the gICA-derived (3.6C) and individualized (3.6D) parcellations. The black line in each figure denotes the default significance level (α) of 0.05.

MAV, could result in slight differences in MAV spatial definitions. The second factor at play is the small sub-parcellations that make up the larger personode networks. Smaller ROIs are more prone to variance in DSCs due to small fluctuations in spatial definitions resulting in lower overlap between the two ROIs. This is further exhibited in IPA DSCs where one small ROI's definition spatial location being off caused four individuals to exhibit zero overlap with the others. This isn't a statement on one method being superior to another, but it is instead a result of methodological differences resulting in different outcomes. The Personode ROI selection methodology causes more consistency in ROI sizes whereas the IPA results in a more spatially consistent ROI.

While the IPA exhibits high consistency as quantified by the DSCs, there is a lowered intra-group overlap in the hypertension group. One possible origin of this effect is the impact of using dual regression on the data. As our gICA was run on normotensive individuals and then dual-regression was done to obtain the ICs for both the normotensive and hypertensive individuals, we theorize that the dual-regression contributes to lowering hypertensive individual's DSCs. This perspective is supported by it being a consistent trend in both the IPA and Personode results as seen in Table 1. Another observation consistent with this finding is the increased number of inconsistent ROI definitions in hypertensive individuals as seen in Figures 3.2A. As previously mentioned, three of the hypertensive individualized ROIs did not show overlap with any of the others while only one ROI of the normotensive individuals showed this same result. While these issues represent a very small amount of the overall ROI definitions, it could be hypothesized that dual regression plays a part in this issue. It is also notable that Personode achieves higher consistency in ROI size. Personode and IPA operate in similar ways but differ in some key points. The Personode algorithm undergoes a step of multiplying ICs by binary canonical resting state network (RSN) templates. This enforces a general shape onto the ROIs selected. Personode and IPA attack the problem of ROI definition in two different ways, but fundamentally the two goals are different.

The second stated goal of this study is to build ROIs that are functionally homogeneous. The proposed IPA exhibits elevated ROI homogeneity in both the group and individualized parcellations implying that it accomplishes its goal. The caveat to the IPA's accomplishment is that ROI homogeneity values are intrinsically linked to their size. While in our testing these quantities do not exhibit simple linear or quadratic scaling, it is known that the larger ROI sizes will lower their expected homogeneity value (Gordon et al., 2014). True to this assumption, we find that many of the ROI homogeneity values shown in Figure 3.5 appear to be negatively correlated to the ROI sizes seen in Figure 3.4.

In general, the gICA-derived atlas ROI sizes were smaller and the MNI ROIs were bigger as compared to the individualized ROIs. This suggests differences in homogeneity values seen in Figure 3.5 may be explained in part or in total by the differences in the ROI sizes.

When statistical testing was applied to the homogeneity values to see if there were any significant differences, nearly all parcellations showed no statistically significant differences in groupwise expression. All ROIs except for ROI 10 of the gICA-derived parcellation tested against the Wilcoxon rank-sum test exhibit no differences between the groups. While this could point to the IPA having the ability to discern differences in groupwise expression of regions, much more testing is needed to make such a claim.

Further groupwise differences quantified by the DDT showed no significant hub nodes in the 35 ROI tested. Similarly, the Personode parcellations also did not produce any significant hub nodes. Due to the IPA producing fewer ROIs, nodal significance is difficult to establish in the DDT trials. With less than 16% of the total possible connections present in the IPA parcellations as compared with previous MNI-based studies, the IPA presents difficulties in being applied to graph theory analyses.

To examine if the number of ROIs was preventing the DDT from detecting significant hubs, a test was performed aimed at building parcellations with increased numbers of ROI. Changing the spatial Pearson threshold of the IPA to the 50th percentile resulted in parcellations with 44 regions built by the IPA. When these parcellations were used in the DDT, the individualized parcellations resulted in two hub nodes corresponding to the right caudal middle frontal and left rostral anterior cingulate and the gICA-derived parcellations resulted in one hub node located in the left rostral anterior cingulate. The caudal middle frontal (CMF) region of the brain is associated with the sensorimotor network while the anterior cingulate cortex is involved with the salience network. These findings imply some possible areas of change related to hypertension and represent a similar result with our previous work (Reeves, Ahmed, Sun, et al., 2023), where we used standard MNI parcellation and found 5 ROIs that showed differential expression in the brain, including the right thalamus, right hippocampus, left pars triangularis, left caudal middle frontal, and left pars orbitalis. Among the 5 regions we previously found, the caudal middle frontal was one of them. In slight contrast, we previously found the left CMF showed differential expression, we currently find the right CMF shows groupwise changes. This could point to the differential functional activation patterns of regions in the sensorimotor cortex of which the CMF is associated. The other hub node found in this analysis—the left rostral anterior cingulate—points to the consistency between

the two parcellation methods.

When looking specifically at previously studied methodologies that focus on employing ICA to analyze the brain, ICs have been used as spatial activation markers for quite some time. One of these methods involves using the power spectra and spatial activation scheme of ICs to define ICs of interest (Allen et al., 2011). Once ICs were validated by several experts, the ICs could be classified as a RSN and further analyzed for detecting covariate differences. Another study that focused on defining RSNs directly from ICs did so by utilizing a toolbox that trained a machine learning model to detect artifactual from signal components (Salman et al., 2022). Once trained, the classified ICs could then be labelled by pre-existing methods such as AAL. Another study inferred RSNs by matching ICs obtained through ICA on large datasets (Du et al., 2020). Once RSNs were established, they were then applied to a spatially constrained adaptive-ICA which quantified individualized metrics. All these methods employ the ICA to define ROIs, but all approach the issue of ROI definition from a different perspective. This holds true for the functional parcellation methods profiled in this study. Neither Personode nor the IPA approach the ROI definition step in the same way that previous studies have which delineates the previous studies from this one. There is overlap in the philosophy of employing ICA to define regions of interest in the brain, but these methods are all distinct from one another.

Because the IPA is focused on defining smaller ROIs as compared to other methods, this theoretically allows for a greater number of ROIs to be built. For some analyses, this represents tremendous flexibility in that the IPA can be adapted to build differing numbers of ROIs depending on the findings in the data and the desired analysis method. On the one hand, increasing ROI count allows for a more powerful analysis when using graph theory (e.g. the DDT results) or various other analyses. On the other hand, the increased ROI count comes at the expense of lowering the spatial Pearson threshold. When the spatial Pearson threshold is lowered, the resulting IC picked for ROI definition corresponds less precisely to the region attempting to be defined. While this could cause issues in ROI definitions, our testing found no major issues when increasing from 35 to 44 ROIs. The flexibility afforded by the IPA allows for fine control over ROI number and size which results in an algorithm that can adapt to suit the needs of a study.

An issue that requires further research is determining whether individualized or gICA-derived parcellations more accurately represent functional activation patterns found in the data. Given the higher homogeneity values found in the gICA-derived parcellations, it would be natural to draw the conclusion

that they are more accurately capturing a more functionally distinct ROI, but there is some uncertainty in that assumption. The uncertainty comes from the fundamental differences that exist in the data and homogeneity's large inversely-proportional dependence on ROI size. Preliminary testing was conducted on homogeneity values to establish a method of compensating for the effect of ROI size, but no suitable normalization strategy could be devised. Given that homogeneity is the primary metric of inter-model comparisons, future work should focus on developing a method to compensate for size's effect on the data and further establish statistical significance of comparisons through the development of a null-model generation algorithm.

One of the benefits of using this algorithm to build data derived atlases is its generalizability to any model system. Figure 3.1 implies that spatial Pearson correlation with an anatomical atlas is required for candidate IC identification, however, each study and researcher could adapt this step to their own processes. Hand-identification of candidate ICs (Griffanti et al., 2017), or newer techniques - such as machine learning - that can identify signal from noise (Chou et al., 2022; Glasser et al., 2016; Moradi et al., 2020; Thomas Yeo et al., 2011) could be used as alternatives to candidate IC selection. This means that there is no intrinsic dependency on the use of an anatomical reference. Because of this lack of dependency on anatomical parcellations, the IPA could easily be adapted for use on data that may not have readily available anatomical atlases or those that don't fit well with current anatomical atlases, such as those studying brain tumors (Niu, Wang, et al., 2021) or traumatic brain injury (Simchick et al., 2021), or functional imaging of patients who have undergone resection.

Another advantage of this method is that it can be inserted into an already defined processing pipeline. In other words, the output of this algorithm is an atlas that can be used as a one-to-one replacement for an atlas that is currently employed. For example, our past work (Reeves, Ahmed, Jackson, Sun, et al., 2023) used anatomical parcellations to parcellate the brain into different ROIs which was then analyzed using the underlying principles of graph theory. The only change that would need to occur to use the IPA in our previous work would be a simple replacement of the anatomical parcellations with those obtained through IPA. Functional parcellations such as the IPA appear to show greater ROI homogeneity as compared with anatomical parcellations which means that, when analyzing data based on fMRI scans, it is more likely to accurately capture regions of functional activation.

3.6 Conclusion

The work presented here profiles and compares the performance of a data-driven parcellation algorithm known as the ICA-based parcellation algorithm. This method shows large consistencies in ROI definitions quantified by dice similarity coefficients and a higher ROI homogeneity value as compared to another data-driven parcellation method known as Personode as well as the Montreal Neurological Institute's anatomical atlas. Given homogeneity's very large inversely-proportional dependence on ROI size, the IPA warrants further research into how it performs against other data. While it requires further study, the IPA is model agnostic, can directly replace current methods of parcellating the brain in studies involving functional MRI data, and could be used to parcellate a subject's brain in their native space resulting in less interpolation of the timeseries.

3.7 Acknowledgements

I want to thank Dr. Michelle Brown for her help in initial data validation and Eric Goetz for his aid in software development. This study has been reviewed and approved by the Institutional Review Board athe Medical College of Georgia (IRB number 1404353). This work is funded by NIH grant Ro1HL143440(Su) and the Augusta University MRI Intramural Program.

3.8 Author Contribution Statement

William D. Reeves: Methodology, Software, Validation, Formal analysis, Writing – original draft, Visualization Ishfaque Ahmed: Methodology. Brooke S. Jackson: Conceptualization, Validation, Writing – review & editing. Wenwu Sun: Methodology. Michelle L. Brown and Celestine F. Williams: Investigation, Resources. Catherine L. Davis: Validation, Writing – review & editing, Supervision. Jennifer E. McDowell: Conceptualization, Writing – review & editing, Supervision, Project administration, Funding acquisition. Nathan E. Yanasak: Validation, Resources, Data Curation, Writing – review & editing, Project administration. Shaoyong Su: Conceptualization, Writing – review & editing, Supervision, Project administration, Funding acquisition. Qun Zhao: Conceptualization, Validation, Writing – review & editing, Supervision, Project administration.

CHAPTER 4

EVALUATION OF FUNCTIONAL PARCELLATIONS IN A LONGITUDINAL DEVELOPMENTAL PIG TBI MODEL USING THE ANATOMY-FREE IPA

4.1 Introduction

Traumatic brain injury (TBI) is a very serious condition which results in over 2.5 million hospitalizations and 56,800 deaths annually (Peterson et al., 2019). Furthermore, an estimated 3.17 million people are living with a long-term disability related to their TBI (Zaloshnja et al., 2008), although the number of cases may be less well-known (e.g. Daugherty et al., 2025). A previous study has demonstrated a significant increase in the mortality rate of those diagnosed with TBI versus a control individuals over a thirteen year period (McMillan et al., 2011). TBI can be stratified into three different categories: mild, moderate, and severe. Previous categoization was solely based on the Glasgow coma score (Teasdale & Jennett, 1974), but new clinical guidelines suggest a nuanced approach to TBI classification that allows for a more tailored treatment plan (Eapen et al., 2022). While detection methods and classification criteria have improved over the years, very little improvement has been made in terms of patient outcomes in recent years (Stein et al., 2010) with up to 20% of mild TBI individuals being unable to return to work within one year of their injury(Nolin & Heroux,

2006). As of 2023, a computed-tomography (CT) image without contrast is the standard of care for acute assessment of TBI (Valente et al., 2023), but a higher detail can be found in various magnetic resonance imaging (MRI) modalities (Griffin et al., 2019; Yuh et al., 2013). In the post-acute phase of injury, one MRI modality of particular interest is functional MRI (fMRI) which can provide a unique perspective into how the brain function modeulates with TBI (Irimia & Van Horn, 2015).

One key aspect of fMRI is how brain oxygen consumption is tracked over time by the blood-oxygen level dependent (BOLD) signal (Logothetis, 2008; Ogawa et al., 1990; Uludağ, 2023). The ability to build so-called timeseries vectors that track a given region's BOLD signal over time provides the ability to compare how two regions act in similar or dissimilar ways. fMRI analyses come in two flavors: task-based and resting-state studies. While task-based studies focus on the brain activation during specific experimental tasks (Cao et al., 2014; McGillivray et al., 2021; Morante et al., 2021), resting-state fMRI (rs-fMRI) focuses on studying brain activity while the individual is in a relaxed wakeful state. Through pioneering experiments involving rs-fMRI, resting-state networks of brain activity were discovered (B. Biswal et al., 1995; Damoiseaux et al., 2006) which represented a crucial step towards establishing the paradigms currently in use for rs-fMRI study (Seitzman et al., 2019). By measuring the differences in timeseries vectors, researchers can establish how functionally connected two regions are. Collectively referred to as the functional connectome, this functional linkage between different regions of the brain allows researchers to study how the brain reacts to a myriad of disease states. These connectomes are built on the underlying principle that the brain can be segmented into discreet regions or "parcels". This process is typically performed with standardized parcellations referred to as atlases. In human studies, one of the standard atlases is the Montreal Neurological Institute atlas (Fonov et al., 2011), but there are several other techniques for parcellating the brain functionally (Lemaire et al., 2019; Rolls et al., 2020; Tang et al., 2010). While clinical MRI has been shown to lead to a higher detection of abnormalities following TBI (B. Lee & Newberg, 2005), TBI research utilizing fMRI, has had issues with data heterogeneity (Kashou et al., 2024). In contrast, there is some evidence to suggest that female individuals have a higher ability to cope with the injury in a behavioral and pathological sense (Rubin & Lipton, 2019). While there is evidence to support the increased ability of female individuals to cope with TBI, a review of clinical data and animal studies found opposing trends in the data suggesting the data heterogeneity, methodology, TBI severity, and many other factors affect the outcome of a given study (Gupte et al., 2019). Given the prevalence of TBI and the lack

of consensus on how TBI effects brain function, there is a need to develop a TBI model system that can be used to study TBI prospectively in parallel with retrospective clinical studies.

The pig is a translational animal model analogous to humans (Netzley & Pelled, 2023) as they have a more similar neuroanatomical structure to humans as compared to the traditional rodent (rat or mouse) model (Meyerholz et al., 2024). The pig TBI model system is of particular interest as induction of TBI can be done in a controlled manner (Kinder et al., 2019). In the piglet model, predictive MRI functional biomarkers have also been found (Ahmed et al., 2025; Simchick et al., 2019; H. Wang et al., 2021) further showing its promise as a translational model(Simchick et al., 2022). In this study, a piglet model system is used to study the neurodevelopmental, sex-linked, and longitudinal effects of TBI induced in the motor cortex. The process of TBI induction involves the use of a controlled cortical impact (CCI) (Osier & Dixon, 2016) to create analogous TBI across multiple individuals. The induced TBIs causes several downstream effects (Simchick et al., 2021) ultimately resulting in several challenges in data processing. One of the biggest challenges in TBI data processing is the shifting of the brain's midline (Hou et al., 2017) due to swelling. This can be seen in both the acute- and chronic stages of injury (Puffer et al., 2019) and it causes a shift in neuroanatomy. This shift in neuroanatomy causes the underlying assumptions of connectomes to be called into question. Specifically, if there is swelling and midline shift, the neuroanatomical structures are no longer in their homeostatic positions which causes issues in assuming the data can fit a standardized parcellation strategy.

In our previous work (Reeves et al., 2025), a method referred to as the independent component analysis (ICA)-based parcellation algorithm (IPA) was proposed for analyzing resting-state fMRI data of hypertensive human volunteers. While initially designed for human data analysis, the model-independent nature of the method allows it to be used in alternative model systems such as the developmental pig model used here. The IPA has shown promise as an alternative parcellation method, using ICA as the basis for defining ROIs that could then be used for further analysis. The IPA produced spatially consistent ROIs with elevated ROI homogeneity values compared to other parcellation methods. However, one of the issues of the previous work was the persistent reliance on a standardized anatomical atlas as the anchor for ROI definitions. At that time, a standardized anatomical atlas was used to identify possible independent components (ICs), used in the definition of new ROIs. Given that one of the goals of the IPA was to remove the standardization of ROI definitions to adapt to individualized changes in BOLD activation, the anatomical

anchor prevented the IPA from achieving that goal. In this work, both the individualized (iIPA) and group-based (gIPA) IPA are refined to remove the anatomical anchor and to profile how they may aid in the processing of TBI data. The newly modified IPA will be referred to as the anatomy-free IPA (af-IPA) to differentiate it from its preceding iteration which will retrospectively be referred to as the anatomical IPA (a-IPA). With the underlying goals of spatial consistency and regional homogeneity as important landmarks for the method to steer towards, the performance of the af-IPA is analyzed anew for this piglet TBI model system.

4.2 Materials & Methods

4.2.1 Pig demographics, acquisition, and processing

A total of thirty-four pigs were selected for this study which represented a subset of a larger cohort of individuals in an ongoing study. The demographic information of these individuals is provided in Table 4.1 below. Three treatment groups were established for this study defined by the severity of their induced TBI. TBI induction was performed by CCI (4 m/s velocity, dwell time of 400 ms) with an impact depth of 3mm for mild TBI individuals and a 9mm impact depth for severe TBI individuals (Schantz et al., 2024). A sham group consisting of individuals that underwent a craniectomy procedure but did not receive CCI was also established. Craniectomy and TBI procedures occurred when the pigs were seven weeks old and the pigs were scanned over three sessions one day prior, one day after, and sixty-three days after their respective surgical procedure.

Table 4.1: Subject demographics of piglet cohort. Three treatment schemes are shown including sham, mild TBI, and severe TBI. Sham subjects received a craniectomy but no traumatic brain injury (TBI) induction. The two TBI groups, mild and severe, are differentiated by their cortical impact parameters of 3mm and 9mm respectively. Each subject was scanned over 3 timepoints for a total of 102 scanning sessions.

	Sham	3mm	9mm	total
female	6	8	8	22
male	4	5	3	12
total	IO	13	II	34

Structural MRI and resting-state fMRI (rs-fMRI) scans were performed on a GE Discovery MR750 3.0T MRI scanner at the University of Georgia Bio-Imaging Research Center. The first two sessions were scanned using a 16 channel HD T/R knee coil and the final session scans were obtained using a 16 channel flex coil due to the increase in size of pigs caused by regular growth and development. A full list of scan parameters is given in table 4.2. Sedation was administered by intramuscular injections of xylazine (2 mg/kg Rompun, Dechra) and midazolam (0.2 mg/kg Sagent Pharmaceuticals). After sedation, topical lidocaine (0.5 mL 4% oral lidocaine, Novitium Pharma) was applied to the laryngeal folds along with intravenous propofol (0.5 mL to effect, PropoFlo, Zoetis) to facilitate intubation. Sedation was maintained via 1.0 – 2.5% inhalant isoflurane (VetOne) in oxygen. Pigs were allowed to respirate spontaneously while their temperature, respiration and heart rates were monitored. During the third session of scans the pigs were also given intravenous butorphanol (0.2 mg/kg Torphadine, Dechra). This study was performed in accordance with the guidelines outlines in the NIH Guide for the Care and Use of Laboratory Animals (Council, 2011) and was approved by the University of Georgia Animal Care and Use Committee (Animal Use Protocol: A2023 07-021-Y2-A7).

Table 4.2: Scanning parameters of all functional and structural MRI data.

	First Two Timepoints Final Timepoint			
Scan Type	fMRI	Anatomical	fMRI	Anatomical
Sequence	2D EPI	3D FSPGR	2D EPI	3D FSPGR
Imaging plane	coronal	axial	coronal	axial
Slice number	46	II2	46	124
Slice Thickness (mm)	2	0.5	2	0.5
Field of View (mm ²)	128 x 128	128 x 128	192 X 192	192 X 192
Matrix Size	64 x 64	256 x 256	128 x 128	512 X 512
Repetition Time (ms)	3000	8.4	3000	10.37
Echo Time (ms)	31	3.65	31	4.6
Flip Angle (degree)	80	9	8o	9
Total Volumes	300	I	300	I

Data pre-processing was performed using Statistical Parametric Mapping 12 (SPM12) (Penny et al., 2007) on MATLAB 2021b (MathWorks, Natick, MA). Processing steps included unwarping, slice timing correction, and removal of the first five volumes of the fMRI data. Individuals' functional and structural data were further processed by FMRIB Software Library (FSL) (Smith et al., 2004). These steps included data masking via FSL's Brain Extraction Tool (BET) and registration to reference fMRI space via FMRIB's Linear Image

Registration Tool (FLIRT). Registration allows all individuals to be placed in the same reference data space which is a requirement for subsequent processing steps. A +63 days sham individual was chosen as the reference space based on data size and quality considerations. Individual anatomical data were segmented into gray matter maps using FMRIB's Automated Segmentation Tool (FAST) before being registered to reference fMRI space via FLIRT. Sham subjects' group independent component analysis (gICA) data with 250 ICs was obtained via FSL's Multivariate Exploratory Linear Decomposition into Independent Components (MELODIC) multi-session temporal concatenation, and each individual's ICs were calculated using dual regression after applying FSL's FMRI Expert Analysis Tool (FEAT) low-level preprocessing on masked fMRI data from the TBI individuals. Once the results from gICA are obtained and each individual has their gray matter maps and dual-regression results, the af-IPA is then performed.

4.2.2 IPA Overview and Procedure

The af-IPA was performed through several steps that have been detailed in our previous work. The procedure is largely unchanged except for the final step of the process which now includes gray matter overlap enforcement and the candidate IC selection stage. The candidate IC selection process produced a list of ICs and their corresponding overlap with the gray matter similarly to the a-IPA method. The difference in candidate IC selection is the shift in focus away from anatomical landmarks as the anchor points for the ROIs to gray matter overlap being the anchor point for the ROIs. This is discussed in further detail in the following section. Due to strict requirements for ROI size and GM overlap, the af-IPA produced parcellations with a varying number of ROIs. This stemmed from the slight differences in IC activation between different individuals along the same IC.

The candidate IC selection procedure

The second stage of the af-IPA was referred to as candidate IC selection is a complex series of steps which sought to calculate to what extent candidate ICs overlapped with the gray matter. This process can be broken into two overarching steps. The first step involved clustering ICs into spatially similar groups and rejecting those ICs that exhibit artifactual patterns (Griffanti et al., 2017). Adapted from Ji et al., 2016, this clustering process began with dimensional reduction of the ICs into vectors via principal component analysis (PCA) which were concatenated together to form a two-dimensional embedding of the ICs.

Eta-squared similarity was calculated between all vectorized ICs to form a square similarity matrix. The normalized Laplacian matrix (Pospelov et al., 2021) was then obtained from the similarity matrix before eigenvector decomposition was performed to find the low-dimensional embedding of the data. Optimal eigenvector dimensionality was calculated by finding the minimum variance of distance ratios (Shi et al., 2009). With the assumption that the distance in embedded space (dy) should be proportional to the distance in the original space (dx), finding the minimum of the variance of these distance ratios results in the ideal embedding dimensionality. During this optimization, eigenvector dimensionalities ranging from three to fifteen were tested with the chosen dimensionality resulting in the lowest variance of distance ratios. A square distance matrix was computed from the city-block distance between the eigenvectors before density peak clustering (DPC) was performed to find IC cluster assignments. Artifactual ICs are identified by hand, and after cluster assignments are obtained, those artifactual ICs and any ICs they are grouped with them were rejected from the list of total ICs.

After artifactual components were removed, the remaining ICs underwent the final stage of candidate IC selection referred to as gray matter mapping. Gray matter mapping was performed by quantifying a given IC's spatial overlap with the individual's gray matter map. Both the spatial Pearson and dice similarity coefficient metrics were used to rank the ICs in terms of how well they overlapped with the gray matter probability map. Once the initial rank was established, a binarized ROI was defined from the IC and removed from gray matter map, helping to prevent the selection of overlapping ICs. The top IC was marked in the candidates list and removed from the pool of candidates before repeating the spatial overlap calculation for all remaining candidates. Once a specific number of candidates was defined, the GM mapping was stopped, and the final list of candidate ICs was returned.

4.2.3 Quantifying Parcellation Performance

IPA performance was quantified primarily by two metrics: how consistent were ROI definitions (spatial consistency) and how similar were the voxel-wise time-series within the ROI (homogeneity). As discussed in the previous IPA study, ROI spatial distributions should be relatively constant across individuals while also allowing for individualization of the ROI. To quantify spatial consistency, the dice similarity coefficient (DSC) was calculated across all individuals and ROIs. This metric is a binary measure of overlap between two datasets and is described in further detail in the previous work.

To study the functional homogeneity of the parcellations, each voxel inside of an ROI had its timeseries extracted and had the Pearson correlation calculated between it and all other voxels in the ROI. Once averaged, this produces a measure of how similar the voxelwise timeseries are to one another which was referred to as the ROI's homogeneity. As a basis of inter-parcellation comparison, common labels between a standardized anatomical atlas and the af-IPA parcellations were obtained. Since the current IPA method explores the removal of anatomical markers, to make ROI-to-ROI comparisons, anatomical landmarks were assigned an IPA ROI label that most closely matched their location in the brain. This allowed for the comparative analysis of ROIs between the iIPA, gIPA, and standardized anatomical parcellation methods. To determine what significant differences may exist, a Wilcoxon rank-sum test was performed between the sexes in the same group. The Wilcoxon rank-sum test was chosen because of its non-parametric nature which does not assume the data was sampled from a normal distribution. The rank-sum test was chosen as a post-hoc measure to match the shape of the data.

Central Moments Analysis of IPA Parcellation ROI Size

Previously gIPA parcellations showed consistently lower ROI sizes as compared to the iIPA ROIs. This trend was hypothesized to be caused by the shape of the activation pattern of the ICs produced by gICA (Reeves et al., 2025). To further investigate this trend a comparative analysis was performed between the previous study's data and the data presented here. After loading the gICA and each individual's dual-regression maps for both studies, all non-zero voxel values of candidate ICs were extracted and had their variance, skewness, and kurtosis calculated. In the previous IPA study, it was hypothesized that activation differences in the gICA and dual-regression results caused the differences seen in the ROI sizes. To compare the previous data to the new one, central moment ratios were calculated by dividing the gICA moments by those moments obtained from dual-regression data. This allowed for a single value to represent the relationship between the gICA and dual-regression data for a candidate IC. This process was repeated for all individuals and candidate ICs to build central moment ratio vectors. Once each individual's ICs had their central moment ratios calculated, outliers were removed and a permutation test was performed on each of the metrics. This involved two-tailed testing 100,000 permutations of the data to obtain a measure of how significantly different the two samples' mean values were. Once significance was established, further one-sided testing was performed to determine whether the ratios were significantly larger or

4.2.4 Overview of Graph Theory Metrics

Once the af-IPA performance was profiled, parcellation ROIs were used as the seed regions for a graph theory analysis. To obtain graph theory results, subject fMRI data was parcellated using IPA parcellations to find the ROI's mean regional timeseries. To obtain the mean regional timeseries, voxel-wise timeseries were first extracted, transformed into z-scores via Fisher transformation, and detrended to remove any linear trends present in the data. Along each timepoint each voxel in the region was subsequently averaged to build a vector representing the average activation of the region over time. This process is repeated for all seed regions to obtain a subject's timeseries matrix. Once a subject's timeseries matrix was calculated, Pearson correlation was performed on the matrix to obtain a functional connectivity (FC) matrix. These FC matrices were thresholded to obtain a fully reachable graph and had several graph theory metrics calculated from the resulting adjacency matrices.

To quantify graphical structure, density, characteristic path length, modularity, and mean functional connectivity strength were calculated for each individual's adjacency matrix. Density measured the average number of connections between nodes. A graph with increased density is one that exhibited a higher level of interconnectivity between its nodes. Characteristic path length assessed the average number of steps it took to move from one node to another. A graph that exhibited an increased characteristic path length was a less connected, less efficient graph overall. A graph's modularity represented how many of the graph's nodes formed into clusters that are interconnected but exhibited a low connectivity outside of the group. Lastly, the mean functional connectivity strength for the individual's graph was calculated representing how strong the connections were between various regions in the brain. Of the metrics calculated for each FC matrix, further hypothesis testing was performed. As was done for the previous metrics, all groupwise sex-linked differences were profiled using a Wilcoxon rank-sum test.

4.3 Results

4.3.1 Parcellation ROI Spatial Consistency

Parcellation examples are shown in Figure 4.1 below. Shown in the figure are ROI examples from the gIPA and iIPA parcellations. For visualization purposes, the iIPA parcellations were averaged for each of the subjects in a specified session and sex assignment to build a parcellation that is representative of the whole but does not exemplify any one subject. As can be seen in Figure 4.1, ROI definitions are consistent across various groups. This is further described on an individual scale in Figure 4.2 where the individual-to-individual DSCs are shown. As seen in the figure, both male and female individuals produce spatially consistent ROIs with 54.0% of all mean DSC being above 0.40. The lowest consistency was found in one day post TBI induction male ROIs with the pre-TBI females exhibiting the highest DSC values. Individualized parcellations contain 21 ± 2 ROIs.

4.3.2 ROI Size and Central Moment Comparisons

The size of ROIs is shown in Figure 4.3 below. Examining the mean ROI sizes for male and females over the different scanning sessions, male individuals exhibit more drastic changes in ROI sizes with five ROIs increasing and five ROIs decreasing across the sessions while female individuals showed four decreasing ROI sizes and one increasing size. This sex-related difference in ROI sizes also appears in 3 ROIs that are larger in the males than the females. Two ROIs in the pre-TBI timepoint (ROIs 64 and 113) and one at one day after TBI induction (ROI 64) show smaller ROI distributions in females. Meta-analysis of the central moments derived from the candidate IC activations showed that each metric is significantly different. The outlier-removed distribution of these metrics can be seen in Figure 4.4 below. One-sided testing resulted in variance and kurtosis being significantly larger, and skewness being significantly smaller in the current data. The variance, skewness, and kurtosis all produced p-values less than 0.001 with observed differences of 0.004, -24.421, 4.386 and effect sizes of 0.243, -1.493, and 1.546 respectively.

4.3.3 IPA and Anatomical Parcellation Homogeneity

Homogeneity values for the af-IPA and anatomical parcellations are seen in Figure 4.5 below. The effect of TBI is seen as Homogeneity values trend down-

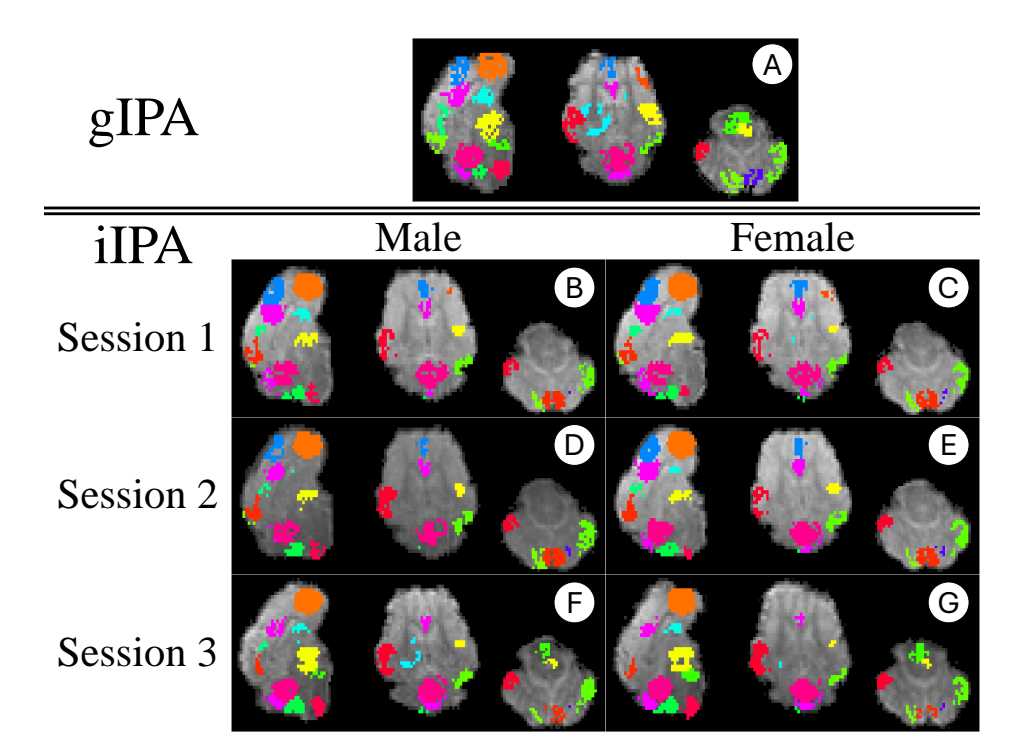


Figure 4.1: Averaged parcellations of the group (gIPA) and individualized IPA (iIPA) are shown. iIPA ROIs shown are averaged for all subjects in a given session and sex assignment where male (4.1A, 4.1D, 4.1F) and female (4.1C, 4.1E, 4.1G) parcellations are shown along the columns and the Pre-TBI(4.1B, 4.1C), one day after TBI induction(2D, 2E), and sixty-three days after TBI induction(4.1F, 4.1G) parcellations are shown along the rows. Because there is only one gIPA parcellation, there is no subdivision along the sessions or sexes. The different colors shown in the parcellations represent different ROIs of the parcellation with individual colors representing the same ROI across all parcellations.

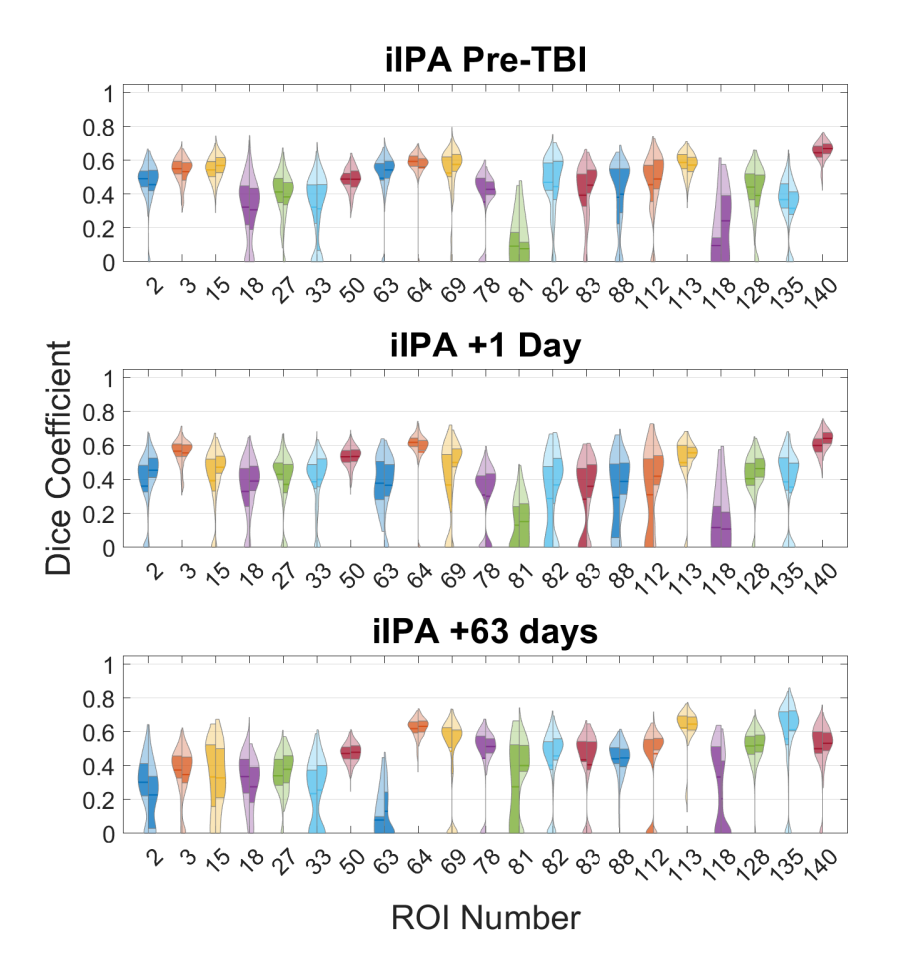


Figure 4.2: Dice similarity coefficients (DSCs) are shown for all subjects in violin plots separated along sessions and sex assignment. Male individuals are shown in the left violins and females shown in the right violins with the different colors denoting different ROIs. The mean of each distribution is shown as a darkened horizontal line in the left and right violins with the 25th and 75th percentiles being shown in the shaded areas of the violins.

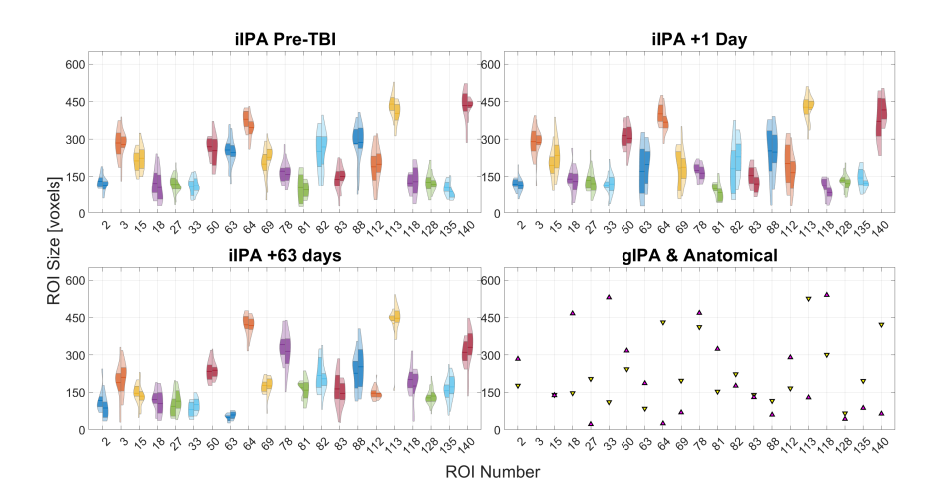


Figure 4.3: Group (gIPA) and individualized (iIPA) IPA ROI sizes are shown for all subjects divided along sex (left violin; male, right violin; female) and sessional assignments. The gIPA ROI sizes are shown as inverted triangles in the plots while the analogous atlas ROIs are shown as purple triangles. The various colors shown in the plots are used to discern the various ROIs from each other and across sessions. The mean of each group is shown as a dark horizontal line in each of the violins and the shaded areas of each violin represent the area between the first and third quartiles.

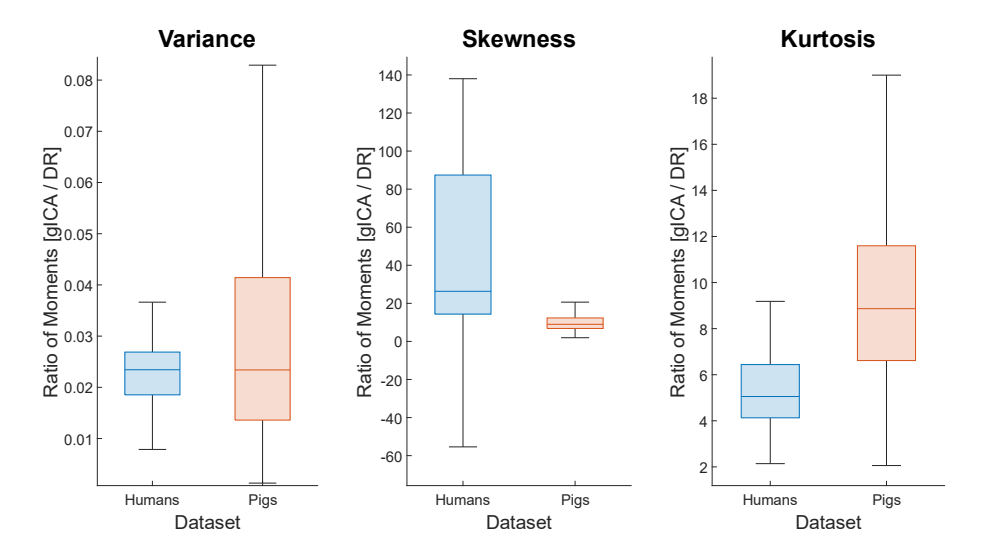


Figure 4.4: Ratio of central moments between human and pig datasets is seen in the figure. The distribution of these data is shown as a box plot with outliers removed for visualization purposes.

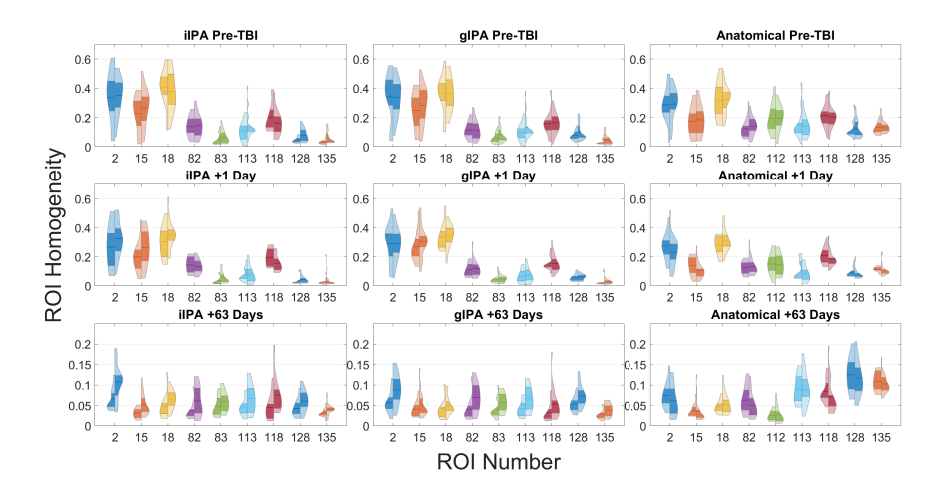


Figure 4.5: Homogeneity values are shown for individualized IPA (iIPA), group IPA (gIPA), and the anatomical parcellations separated along sex and sessional demographics. Various ROIs are shown along the x-axis each of which are represented by a different color of violin. For visualization purposes, only those ROIs that exhibit large differences between males and females are shown. The anatomical atlas demonstrated no sex-linked changes at any timepoint. Male individuals are shown in the left violins while the females are shown in the right violins. The mean of each group is shown as a dark horizontal line in each of the violins and the shaded areas of each violin represent the area between the first and third quartiles.

wards across the sessions. Notably, while anatomical ROI homogeneity values are slightly elevated against some IPA ROI, the only ROIs to exhibit any difference between the sexes are in the af-IPA parcellations with the gIPA showing the most overall at sixty-three days post TBI induction. The iIPA also exhibited six total sex-linked differences – two at the pre-TBI timepoint and four at sixty-three days post TBI induction. Examining the sessional performance of each method quantified by Table 4.3, the af-IPA and anatomical parcellations homogeneity values are very similar. There are specific ROIs that exhibit higher homogeneity in the af-IPA and those that have higher values through the anatomical parcellation, but overall trends show similar performance between the two methods.

Table 4.3: Sessional averaged homogeneity values are shown for the specified parcellation methods. Mean values are shown alongside the standard deviation of the data for the individualized IPA (iIPA), group IPA (gIPA) and anatomical parcellation methods.

	Home	ogeneity	
		Male	Female
	iIPA	0.18 ± 0.15	0.19 ± 0.13
Session 1	gIPA	0.18 ± 0.14	0.18 ± 0.12
	Anatomical	0.20 ± 0.11	0.20 ± 0.11
	iIPA	0.14 ± 0.11	0.16 ± 0.12
Session 2	gIPA	0.15 ± 0.12	0.15 ± 0.11
	Anatomical	0.15 ± 0.09	0.17 ± 0.10
	iIPA	0.05 ± 0.03	0.06 ± 0.04
Session 3	gIPA	0.04 ± 0.03	0.06 ± 0.04
	Anatomical	0.06 ± 0.05	0.07 ± 0.05

4.3.4 IPA Graph Theory Analysis

The results of applying the af-IPA parcellations to graph theory analysis can be seen in Figure 4.6 below. Out of the five metrics shown, the iIPA does not show any significant differences between the sexes under the Wilcoxon rank-sum test while the gIPA exhibits four. All significant differences occur in the severe TBI group where a sex-based difference in graph modularity and functional connectivity strength can be seen for the second session timepoint with further differences being found in the efficiency and characteristic path length for sixty-three days post TBI induction data.

4.4 Discussion

Through visual inspection of the average iIPA parcellations seen in Figure 4.1, ROIs are similar in their spatial definitions across the different groups of individuals. While individuals exhibit differences in the exact spatial distribution of ROIs as seen in Figure 4.2, cross-group average anatomical placements are consistent. When investigating the same trends at the individual level, the conclusion isn't quite as clear. As seen in Figure 4.2 many ROIs exhibit mean DSC

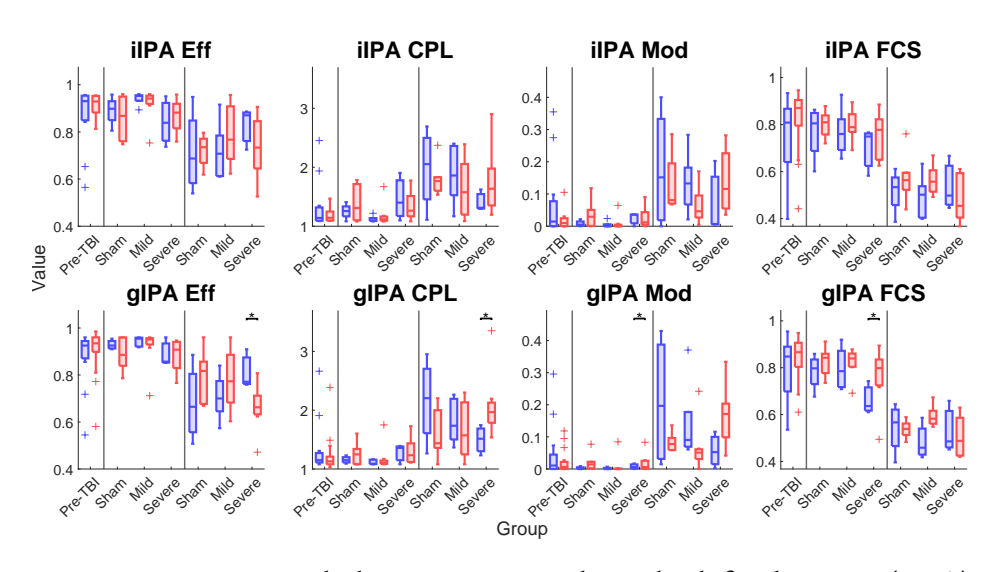


Figure 4.6: Various graph theory metrics are shown both for the group (gIPA) and individualized (iIPA) IPA parcellations. The four metrics shown are density (Den), characteristic path length (CPL), modularity (Mod), and functional connectivity strength (FCS) with male individuals being shown in blue box plots and females being shown in red box plots. The data is further separated along sessional lines with the dark vertical lines shown in each plot delineating pre-TBI, one day post-TBI induction, and 63 days post-TBI induction, while the different experimental groups are shown along the x-axis for each plot. Significant differences are also overlaid in the plot with * indicating a p-value of less than 0.05.

values above 0.5 with some reaching a DSC of 0.6 implying large consistencies in ROI definition, many ROIs exhibit poor overlap with other individuals in the group. Because iIPA ROI definitions are directly based on the dual-regression of gICA components, inconsistencies in ROI definitions all stem from individual differences in IC activation. This presents a challenge in longitudinal analyses where, especially in the case of acute TBI, anatomical features may shift due to swelling and cerebral hemorrhage. Despite some inconsistencies in spatial distribution, ROI sizes are very consistent across males and females with only 3 ROIs showing any significant difference. These data also result in gIPA and iIPA ROIs that are closer in size than what was seen in our previous work (Reeves et al., 2025). Previous changes in ROI sizes were linked with the difference in activation between gICA and dual-regression ICs. Following that same logic, the difference between gICA and dual-regression map activation patterns must be smaller. This was confirmed by central moment analysis where pig kurtosis ratios were significantly lower than those in humans and showed the largest effect size of -0.459. This change in kurtosis ratios between the gICA and dual-regression results (shown in Figure 4.4) is likely what leads to the difference in the gIPA/iIPA ROI size distributions between our previous study and this one. This finding helps reinforce the hypothesis originally proposed.

While spatial definitions appear positive, the lack of clear IPA superiority in ROI homogeneity values versus the anatomical parcellation is an issue. More surprising than the af-IPA performance, is the ability of the anatomical parcellation to maintain higher homogeneity values in many ROIs than IPA. In our previous study, ROI homogeneity was clearly inversely proportional to ROI size, but the pig data presented here doesn't show such a clear trend. Some ROIs that are smaller in the anatomical parcellation (i.e. ROIs 88, 128, and 140) exhibit clearly depressed homogeneity values as compared to other small ROIs such as ROI 64. Given that ROI 64 is much larger in the gIPA parcellations and shows similar homogeneity values to the anatomical, it is difficult to establish the same inverse relationship between ROI size and homogeneity in this model system. Homogeneity appears to be more related to the location of the ROI than the size of the ROI. This could be related to the young developing pig brains as compared to fully matured humans.

Two factors that weren't previously explored were the impact of acute injury and how the af-IPA can perform in a longitudinal analysis. From Figure 4.5 we can see a clear reduction in homogeneity values which may be related to known regional homogeneity decreases related to development (Hong, 2023), but could also be linked to expected deficiencies caused by TBI (J. Zhan et al., 2015). The effects of TBI may be seen in sex-linked differences observed in the

parcellations, however. Through analyzing sex-based differences in homogeneity distributions, Figure 4.5 shows IPA can produce a significant difference in homogeneity values for certain ROIs. Specifically, across both IPA methods, ROIs 2 and 18 show an elevated homogeneity in the female individuals. When looking at all significant differences shown in parcellation methods, the female individuals always show an elevated mean homogeneity as compared to their male counterparts. Given that the majority of these significant changes occur at the session 3 timepoint, these differences could be indicative of sex-linked difference in TBI compensatory mechanisms.

The method described here is highly dependent on the quality of ICA performed prior to its implementation. The gICA and dual-regression ICs are what ultimately become the ROIs defined in the different parcellations, so ensuring those are the best representations of the data is of vital importance to ROI definition. This becomes especially salient when devising the best strategy for longitudinal studies. In this study, it was decided to improve the statistical power of the data by using as many sham individuals as possible which means that sessions one, two, and three sham individuals were used as one dataset for gICA. This ensures consistency of IC number across the data and that all sessions and data start from the same gICA, but it also means that the gICA is based on data of developing pigs over a two-month span. ROI assignment number consistency is a very helpful result of this gICA scheme as a given IC will represent the same activation scheme across all individuals and timepoints. An alternative to this strategy is to run multiple gICAs across the different sessions which could be a better snapshot in time but doing so results in lower statistical power and inconsistencies in IC assignment number. While this method is appealing due to it being more sensitive to sessional changes, the ICs assigned in the gICA would be inconsistent across timepoints requiring further analysis to define analogous ROIs over time.

ROI assignments with the longitudinal ICA resulted in ICs that were consistently labelled over each session, but when making comparisons to the anatomical ROIs, ROI reassignment was performed. This ROI reassignment is a probabilistic process which places all ROIs on top of each other to calculate an overlap score. Based on the highest overlap, original ROI labels are reassigned to analogous ROI labels. This process is used to take anatomical labels to IPA labels but could be adapted to find consistent ROIs across time using a sessional gICA scheme. A final issue with the current scheme of IPA is the inconsistencies in the number of ROI defined in iIPA. Initial testing found that ROI size thresholding plays a large role in the consistency of ROI definitions. This effect is more pronounced in ROIs that are near the minimum size threshold, but be-

cause of differences in individual data can affect larger ROIs as well. Allowing for smaller ROIs or removing the strict GM overlap requirement would lead to an increase in consistency of the number of ROIs defined.

Global graph theory metrics shown in Figure 4.6 show sex-linked differences in the gIPA parcellations but no significant differences in the iIPA parcellations. This likely stems from the differences observed in ROI size, number, and position which produced slightly different distributions FC values resulting in divergent graphical organization. The one day post TBI induction timepoint sex-linked differences in functional connectivity strength and modularity imply that the female severe TBI group is, even at one day after TBI induction, responding in a different fashion to TBI than the male individuals. The gIPA severe TBI group 63 days post TBI efficiency and characteristic path length differences are two sides of the same coin implying that these graphs are less connected, and information moves less freely throughout the graph for female individuals. Furthermore, sixty-three days post TBI induction graphs clearly exhibit an overall different organization strategy as compared to sessions one and two. It is unclear exactly what factors influence the change in graph theory metrics, but one day post TBI induction differences may be tied to compensation related to the acute TBI while sixty-three days post TBI differences may be connected to a deeper restructuring of brain functional activation patterns. While there is evidence to suggest that females in animal models exhibit better outcomes than their male counterparts, methodology and experimental design play a large role in that finding. It is difficult to say definitively what differences exist and what the expectations should be for the individuals in this acute and post-acute phase of TBI, but the gIPA appears to match those findings in the literature for human TBI (McGlade et al., 2015; S. Wang et al., 2018).

The af-IPA underperforms in attempting to achieve its goals of spatial consistency and functional homogeneity. Being unable to match spatial consistency of the a-IPA while also being unable to outperform the idealized anatomical atlas are troubling findings. To get a broader perspective on the IPA's performance, however, there must be a discussion of the factors that produced these results. The purpose of this study was to discover sex-linked differences in a developmental pig TBI model. While the goals of this study are lofty and worth striving for, they bring with them many confounding variables that make data processing difficult. First, The difference in weight between when the pigs enter and when they leave the study can be upwards of 200 pounds. This means that physical considerations such as which coils to use and how best to scan the individuals are a serious consideration. Based on physical changes, data quality, and scanning optimization, different coils were used for the different timepoints and

concordantly data sizes changed over time. Further confounding the results, there is an expectation of sex-linked differences in response to TBI (S. Wang et al., 2018) as well as the separation of the individuals into three distinct treatment groups. Taking all these factors into account, the confounding variables in the system produce a complex and challenging dataset to work with. Placed under this lens doesn't absolve the af-IPA of its performance issues, but it helps describe a possible origin for the underlying difficulties. Despite the analytical challenges, the af-IPA is capable of building adaptable parcellations based on the underlying data present in the experimental data.

4.5 Conclusion

In this work, the performance of an improved version of the independent component analysis based parcellation algorithm (IPA) known as the gray matter IPA (af-IPA) was further profiled. Through the dice similarity coefficient, the af-IPA was able to show consistency in ROI definition but couldn't significantly outperform the anatomical parcellation in terms of region of interest homogeneity. This underscores the challenges in the processing of this model system, especially in the acute phase when individuals may exhibit large areas of signal loss. While the individualized parcellations couldn't detect any sex-linked differences in graph theory metrics, group IPA was used to find significantly increased functional connectivity strength in the female individuals which match findings in the literature. While the TBI model system presents many challenges in methodological development, the af-IPA represents an adaptable method for parcellating the brain into regions of interest. The removal of an anatomical anchor allows for adaptability in cases of midline shift or other scenarios where signal loss or swelling causes a shift in the anatomical landmarks which idealized anatomical parcellations are particularly susceptible to.

Funding

Work funded by the National Institute of Health (NIH) grants R21NS123732 and R21NS131526.

CHAPTER 5

Conclusion

The evolving data acquisition strategies for MRI and their proliferation in number demand improvements in research and analysis methodology. Increasing field strengths, improved scanning techniques (e.g., simultaneous multislice imaging (SMS) techniques Barth et al., 2016) and reconstruction methods (e.g., super-resolution Payne et al., 2023) are producing MRI images with greater resolution and detail than ever before. Due to the improvement in data quality but also the sheer volume of data, fMRI shows promise towards revealing a more sophisticated interpretation of function of the human brain. Through functional imaging, we are beginning to unravel many aspects of human consciousness and disease states by applying the inherent activation pattern of the brain to higher level analyses, although the scope and utility of what we may learn remains to be seen. It is at the intersection of increasing field strength and improvements in fMRI methodology that the preceding work has made its mark.

The initial work discussed here represented a very specific but meaningful change to statistical testing which produced significant changes in the detection of group-based differences. The brute-force mean-variance matching algorithm significantly improved the performance of the difference degree test (DDT) by increasing true positivity rates while also maintaining nominal false positivity rates. By increasing the sensitivity of the DDT and applying it to experimental data, several regions that could be linked to neurological adaptations to hypertension were found, and given the increase in sensitivity, the results are more likely representative of the data than the previous unmodified version. The DDT is at the forefront of determining graph-based group-linked changes in the data and the improvement made here helps to further its goal of aiding those analyses. While the work was able to improve the performance significantly, there is an upper limit to the progress than can be made by focusing

on improving the performance of that specific test. The development of the IPA symbolizes a step in the right direction of methodological development. The focus of the IPA is not limited to statistical testing, but to answer a larger question in the field: "what method of parcellation best represents the data?" Whether the effect of the IPA is large or small in the field is still to be seen, but the philosophy used in the development of the IPA is what is required to improve the field. To push forward, we must identify problems in the field and work along several paths to achieve a more wholistic result.

The foundational thesis of the IPA was to reduce the influence of interpolation and to allow the data to speak for itself. There are very real issues that come with assuming an individual can or should fit an idealized anatomy. Beyond the fact that a researcher's internal biases can influence the output of a study, the individuals chosen for study also shape the output on an individual level based on their own personal anatomical differences or clinical history. When the selection and research biases play into construction of idealized parcellations, the resulting atlas is then shaped by these factors. These issues were at the forefront when initially designing the functionality of the IPA.

Initial development of the anatomical IPA (a-IPA) provided a strong base from which further improvements could be made. It could build spatially consistent and functionally homogeneous ROIs which yielded parcellations that could be used in post-hoc analyses. Its use in functional connectivity analyses is of particular interest, as the ROIs are defined from functional activation patterns of the data. While this was a solid starting point, one of the larger goals of the a-IPA was to remove the requirement of idealized anatomical parcellations. This led to the development of the anatomy-free IPA (af-IPA) which removed the need for an idealized anatomical atlas from the ROI construction procedure by replacing it with a need for structural scans obtained from the same individual. This step produced parcellations that were able to address real-world issues in acute-phase traumatic brain injury. Issues like signal drop out and midline shift can now be compensated for by using the af-IPA. By using the individual's own structural scans, af-IPA parcellations can adapt to large anatomical changes.

While the IPA is a very useful tool, the field of MRI research is currently grappling with issues that will likely cause great change over the next few years. One immediately prescient issue is data reproducibility (Stikov et al., 2019; Stöcker et al., 2025). The IPA is just another tool in the analytical toolbelt, but too much heterogeneity in the field has led to a divergence of findings across studies (Vogt, 2023). While it may not be the final answer to data reproducibility, the IPA helps reduce the effect of interpolation on the data, which could

improve the homogeneity across studies. Another force of change in the field is the advent of so-called "artificial intelligence" algorithms. These algorithms have already made an impact the field of radiology and the clinical use of MRI (Mitsuyama et al., 2025; Stöcker et al., 2025; Truhn et al., 2023), and they are increasingly relied upon for nearly every task (Morgenstern et al., 2021). Machine learning algorithms have already had an impact on the field (Gassenmaier et al., 2021), but the proliferation "AI" promises to drastically change analyses in the near-term. One issue that machine learning and now "AI" algorithms have is their incredibly massive power consumption which has led to full-scale and scalable power plants being designed solely for their use. In contrast to these methods, the IPA can run in a matter of minutes on a relatively low-powered consumer-grade desktop computer. Another more technical issue plaguing current "AI" systems is the so-called "AI hallucination" (Slater & Humphries, 2025) where the information being presented is false either in part or in its entirety. Techniques must advance and new technologies must be explored for the betterment of science, but the exponential growth in power and data consumption will likely be unsustainable in the long run.

Current methods rely too much on idealizing the individual and guessing what data might look like. The IPA fills an analysis niche by reducing the effect of interpolation and allowing the individual's data to speak for itself. Because of the specific role the IPA fills, it still can be used to help and improve the analysis of fMRI data. The next step in the journey of the IPA is in building upon the function and further profiling its capabilities. Further improvements to the method would give it greater power and allow it to continue competing with other cutting-edge techniques. Refining the noise and artifactual component identification would be of great benefit as it would allow for the construction of an all-in-one package which would require little human feedback to take the output from independent component analysis and output the highest quality parcellations. Refinement and development of the software into a standalone package would also help get it into the hands of more researchers which could, in turn, help refine the method even further. Both in its current state and with future improvements, the IPA is a promising direction towards assisting researchers in finding the next great breakthrough in neuroimaging.

APPENDIX A SUPPLEMENTARY MATERIAL CHAPTER 3

ROI ID	IPA 35 Anatomy	IPA 44 Anatomy	Personode RSN
I	Right Rostral Middle Frontal	Right Rostral Middle Frontal	Dorsal Attention
2	Right Superior Parietal	Right Pericalcarine	Auditory
3	Right Inferior Parietal	Right Superior Parietal	Basal Ganglia
4	Right Lingual	Right Inferior Parietal	Cerebellum
5	Right Medial Orbitofrontal	Right Lingual	Cognition/Emotion
6	Right Putamen	Right Postcentral	Default Mode, Dorsal/Posterio
7	Right Pars Triangularis	Right Medial Orbitofrontal	Default Mode, Medial
8	Right Ventral Diencephalon	Right Vermal lobules VIII-X	Executive Control
9	Right Middle Temporal	Right Putamen	Frontoparietal, Left
IO	Right Precuneus	Right Pars Triangularis	Frontoparietal, Right
II	Right Pars Opercularis	Right Ventral Diencephalon	Ventral Stream, Left
12	Right Lateral Occipital	Right Middle Temporal	Ventral Stream, Right
13	Right Caudal Middle Frontal	Right Precuneus	Postcentral
14	Right Cuneus	Right Pars Opercularis	Precentral
15	Right Superior Temporal	Right Lateral Occipital	Precuneus
16	Right Cerebellum Gray Matter	Right Superior Frontal	Salience
17	Right Posterior Cingulate	Right Caudal Middle Frontal	Sensorimotor
18	Right Vermal lobules I-V	Right Cuneus	Visual, Primary I
19	Right Supramarginal	Right Superior Temporal	Visual, Primary II
20	Left Rostral Middle Frontal	Right Cerebellum Gray Matter	Visual, Medial
2I	Left Rostral Anterior Cingulate	Right Posterior Cingulate	Visual, Higher Level

٠.

22	Left Superior Parietal	Right Vermal lobules I-V
23	Left Inferior Parietal	Right Supramarginal
24	Left Lingual	Left Rostral Middle Frontal
25	Left Medial Orbitofrontal	Left Rostral Anterior Cingulate
26	Left Paracentral	Left Superior Parietal
27	Left Pars Triangularis	Left Inferior Parietal
28	Left Middle Temporal	Left Lingual
29	Left Caudal Anterior Cingulate	Left Medial Orbitofrontal
30	Left Precuneus	Left Paracentral
31	Left Pars Opercularis	Left Putamen
32	Left Lateral Occipital	Left Pars Triangularis
33	Left Thalamus	Left Middle Temporal
34	Left Cerebellum Gray Matter	Left Caudal Anterior Cingulate
35	Left Supramarginal	Left Precuneus
36		Left Pars Opercularis
37		Left Lateral Occipital
38		Left Thalamus
39		Left Caudal Middle Frontal
40		Left Superior Temporal
4 I		Left Cerebellum Gray Matter
42		Left Caudate
43		Left Vermal lobules I-V

44 || Left Supramarginal

BIBLIOGRAPHY

- Ahmed, I., Reeves, W. D., Sun, W., Dubrof, S. T., Zukaitis, J., West, F. D., Park, H. J., & Zhao, Q. (2023). Nutritional supplement induced modulations in the functional connectivity of a porcine brain. *Nutritional Neuroscience*. https://doi.org/10.1080/1028415X.2023.2166803
- Ahmed, I., Reeves, W. D., Laballe, M. H., Taber, M. F., Sneed, S. E., Kaiser, E. E., West, F. D., & Zhao, Q. (2025). A novel integration of brain structural and functional connectivity for identifying traumatic brain injury induced perturbations. *Journal of Neuroscience Methods*, 419, 110459. https://doi.org/https://doi.org/10.1016/j.jneumeth.2025.110459
- Alemán-Gómez, Y., Melie-Garcia, L., & Valdés-Hernández, P. (2006). Ibaspm: Toolbox for automatic parcellation of brain structures [cd]. in: Proceedings of the 12th annual meeting of the organization for human brain mapping, june 11-15, florence, italy. *NeuroImage*, 27.
- Allen, E. A., Erhardt, E. B., Damaraju, E., Gruner, W., Segall, J. M., Silva, R. F., Havlicek, M., Rachakonda, S., Fries, J., Kalyanam, R., Michael, A. M., Caprihan, A., Turner, J. A., Eichele, T., Adelsheim, S., Bryan, A. D., Bustillo, J., Clark, V. P., Feldstein Ewing, S. W., ... Calhoun, V. D. (2011). A baseline for the multivariate comparison of resting-state networks. *Front Syst Neurosci*, 5, 2. https://doi.org/10.3389/fnsys.2011.00002
- Andersen, A. H., Gash, D. M., & Avison, M. J. (1999). Principal component analysis of the dynamic response measured by fmri: A generalized linear systems framework. *Magnetic Resonance Imaging*, 17(6), 795–815. https://doi.org/https://doi.org/10.1016/S0730-725X(99)00028-4
- Andrews-Hanna, J. R., Snyder, A. Z., Vincent, J. L., Lustig, C., Head, D., Raichle, M. E., & Buckner, R. L. (2007). Disruption of large-scale brain systems in advanced aging. *Neuron*, 56(5), 924–35. https://doi.org/10.1016/j.neuron.2007.10.038
- Arslan, S., Ktena, S. I., Makropoulos, A., Robinson, E. C., Rueckert, D., & Parisot, S. (2018). Human brain mapping: A systematic comparison of

- parcellation methods for the human cerebral cortex. *NeuroImage*, 170, 5–30. https://doi.org/https://doi.org/10.1016/j.neuroimage.2017.04.
- Bagattini, C., Mazza, V., Panizza, L., Ferrari, C., Bonomini, C., & Brignani, D. (2017). Neural dynamics of multiple object processing in mild cognitive impairment and alzheimer's disease: Future early diagnostic biomarkers? *J Alzheimers Dis*, 59(2), 643–654. https://doi.org/10.3233/jad-161274
- Barth, M., Breuer, F., Koopmans, P. J., Norris, D. G., & Poser, B. A. (2016). Simultaneous multislice (sms) imaging techniques. *Magnetic Resonance in Medicine*, 75(1), 63–81. https://doi.org/https://doi.org/10.1002/mrm.25897
- Bassett, D. S., & Bullmore, E. (2006). Small-world brain networks. *Neuroscientist*, *12*(6), 512–23. https://doi.org/10.1177/1073858406293182
- Bassett, D. S., Wymbs, N. F., Porter, M. A., Mucha, P. J., Carlson, J. M., & Grafton, S. T. (2011). Dynamic reconfiguration of human brain networks during learning. *Proceedings of the National Academy of Sciences*, 108(18), 7641–7646. https://doi.org/doi:10.1073/pnas.1018985108
- Bastos, A. M., & Schoffelen, J. M. (2015). A tutorial review of functional connectivity analysis methods and their interpretational pitfalls. *Front Syst Neurosci*, 9, 175. https://doi.org/10.3389/fnsys.2015.00175
- Bernas, A., Aldenkamp, A. P., & Zinger, S. (2018). Wavelet coherence-based classifier: A resting-state functional mri study on neurodynamics in adolescents with high-functioning autism. *Computer Methods and Programs in Biomedicine*, 154, 143–151. https://doi.org/https://doi.org/10.1016/j.cmpb.2017.11.017
- Biswal, B. B., Mennes, M., Zuo, X. N., Gohel, S., Kelly, C., Smith, S. M., Beckmann, C. F., Adelstein, J. S., Buckner, R. L., Colcombe, S., Dogonowski, A. M., Ernst, M., Fair, D., Hampson, M., Hoptman, M. J., Hyde, J. S., Kiviniemi, V. J., Kötter, R., Li, S. J., ... Milham, M. P. (2010). Toward discovery science of human brain function. *Proc Natl Acad Sci U S A*, 107(10), 4734–9. https://doi.org/10.1073/pnas.0911855107
- Biswal, B., Zerrin Yetkin, F., Haughton, V. M., & Hyde, J. S. (1995). Functional connectivity in the motor cortex of resting human brain using echoplanar mri. *Magnetic Resonance in Medicine*, *34*(4), 537–541. https://doi.org/https://doi.org/10.1002/mrm.1910340409
- Brown, R. W., Cheng, Y.-C. N., Haacke, E. M., Thompson, M. R., & Venkatesan, R. (2014). Introductory signal acquisition methods. In *Magnetic*

- *resonance imaging* (pp. 113–139). https://doi.org/https://doi.org/10. 1002/9781118633953.ch8
- Bullmore, E., & Sporns, O. (2009). Complex brain networks: Graph theoretical analysis of structural and functional systems. *Nat Rev Neurosci*, 10(3), 186–98. https://doi.org/10.1038/nrn2575
- Calhoun, V. D., & de Lacy, N. (2017). Ten key observations on the analysis of resting-state functional mr imaging data using independent component analysis. *Neuroimaging Clin N Am*, 27(4), 561–579. https://doi.org/10.1016/j.nic.2017.06.012
- Cao, H., Plichta, M. M., Schäfer, A., Haddad, L., Grimm, O., Schneider, M., Esslinger, C., Kirsch, P., Meyer-Lindenberg, A., & Tost, H. (2014). Test–retest reliability of fmri-based graph theoretical properties during working memory, emotion processing, and resting state. *NeuroImage*, 84, 888–900. https://doi.org/https://doi.org/10.1016/j.neuroimage. 2013.09.013
- Carnevale, L., Maffei, A., Landolfi, A., Grillea, G., Carnevale, D., & Lembo, G. (2020). Brain functional magnetic resonance imaging highlights altered connections and functional networks in patients with hypertension. *Hypertension*, 76(5), 1480–1490. https://doi.org/10.1161/hypertensionaha.120.15296
- Carone, D., Licenik, R., Suri, S., Griffanti, L., Filippini, N., & Kennedy, J. (2017). Impact of automated ica-based denoising of fmri data in acute stroke patients. *NeuroImage: Clinical*, *16*, 23–31. https://doi.org/https://doi.org/10.1016/j.nicl.2017.06.033
- Carpenter, P. A., Just, M. A., Keller, T. A., Eddy, W. F., & Thulborn, K. R. (1999). Time course of fmri-activation in language and spatial networks during sentence comprehension. *Neuroimage*, 10(2), 216–24. https://doi.org/10.1006/nimg.1999.0465
- Chen, J. E., Rubinov, M., & Chang, C. (2017). Methods and considerations for dynamic analysis of functional mr imaging data. *Neuroimaging Clin NAm*, 27(4), 547–560. https://doi.org/10.1016/j.nic.2017.06.009
- Chou, Y., Chang, C., Remedios, S. W., Butman, J. A., Chan, L., & Pham, D. L. (2022). Automated classification of resting-state fmri ica components using a deep siamese network. *Frontiers in Neuroscience*, 16. https://doi.org/10.3389/fnins.2022.768634
- Chung, J., Jackson, B. S., McDowell, J. E., & Park, C. (2021). Joint estimation and regularized aggregation of brain network in fmri data. *J Neurosci Methods*, 364, 109374. https://doi.org/10.1016/j.jneumeth.2021.109374

- Cîrstian, R., Pilmeyer, J., Bernas, A., Jansen, J. F. A., Breeuwer, M., Aldenkamp, A. P., & Zinger, S. (2023). Objective biomarkers of depression: A study of granger causality and wavelet coherence in resting-state fmri. *Journal of Neuroimaging*, 33(3), 404–414. https://doi.org/https://doi.org/10.1111/jon.13085
- Cole, D. M., Smith, S. M., & Beckmann, C. F. (2010). Advances and pitfalls in the analysis and interpretation of resting-state fmri data. *Frontiers in Systems Neuroscience*, *Volume 4 2010*. https://doi.org/10.3389/fnsys. 2010.00008
- Colizza, V., Flammini, A., Serrano, M. A., & Vespignani, A. (2006). Detecting rich-club ordering in complex networks. *Nature Physics*, *2*(2), 110–115. https://doi.org/10.1038/nphys209
- Council, N. R. (2011). *Guide for the care and use of laboratory animals: Eighth edition*. The National Academies Press. https://doi.org/doi:10.17226/12910
- Craddock, R. C., James, G. A., Holtzheimer, 3., P. E., Hu, X. P., & Mayberg, H. S. (2012). A whole brain fmri atlas generated via spatially constrained spectral clustering. *Hum Brain Mapp*, 33(8), 1914–28. https://doi.org/10.1002/hbm.21333
- Crossley, N. A., Mechelli, A., Scott, J., Carletti, F., Fox, P. T., McGuire, P., & Bullmore, E. T. (2014). The hubs of the human connectome are generally implicated in the anatomy of brain disorders. *Brain*, 137(Pt 8), 2382–95. https://doi.org/10.1093/brain/awu132
- Damoiseaux, J. S., Rombouts, S. A. R. B., Barkhof, F., Scheltens, P., Stam, C. J., Smith, S. M., & Beckmann, C. F. (2006). Consistent resting-state networks across healthy subjects. *Proceedings of the National Academy of Sciences*, 103(37), 13848–13853. https://doi.org/doi:10.1073/pnas.0601417103
- Daugherty, J., Peterson, A., Black, L., & Waltzman, D. (2025). Summary of the centers for disease control and prevention's self-reported traumatic brain injury survey efforts. *J Head Trauma Rehabil*, 40(1), E1–e12. https://doi.org/10.1097/htr.000000000000975
- Du, Y., Fu, Z., Sui, J., Gao, S., Xing, Y., Lin, D., Salman, M., Abrol, A., Rahaman, M. A., Chen, J., Hong, L. E., Kochunov, P., Osuch, E. A., & Calhoun, V. D. (2020). Neuromark: An automated and adaptive ica based pipeline to identify reproducible fmri markers of brain disorders.

 *Neuroimage Clin, 28, 102375. https://doi.org/10.1016/j.nicl.2020.102375

- Eapen, B. C., Bowles, A. O., Sall, J., Lang, A. E., Hoppes, C. W., Stout, K. C., Kretzmer, T., & Cifu, D. X. (2022). The management and rehabilitation of post-acute mild traumatic brain injury [PMID: 35152817]. *Brain Injury*, 36(5), 693–702. https://doi.org/10.1080/02699052.2022. 2033848
- Eickhoff, S. B., Yeo, B. T. T., & Genon, S. (2018). Imaging-based parcellations of the human brain. *Nature Reviews Neuroscience*, 19(11), 672–686. https://doi.org/10.1038/s41583-018-0071-7
- Fagan, M. M., Scheulin, K. M., Sneed, S. E., Sun, W., Welch, C. B., Cheek, S. R., Kaiser, E. E., Zhao, Q., Duberstein, K. J., & West, F. D. (2024). White matter integrity and motor function disruption due to traumatic brain injury in piglets: Impacts on motor-related brain fibers. *Brain Sci*, 14(3). https://doi.org/10.3390/brainsci14030247
- Farahani, F. V., Karwowski, W., & Lighthall, N. R. (2019). Application of graph theory for identifying connectivity patterns in human brain networks: A systematic review. *Frontiers in Neuroscience*, *Volume 13 2019*. https://doi.org/10.3389/fnins.2019.00585
- Fonov, V., Evans, A. C., Botteron, K., Almli, C. R., McKinstry, R. C., & Collins, D. L. (2011). Unbiased average age-appropriate atlases for pediatric studies. *Neuroimage*, 54(1), 313–27. https://doi.org/10.1016/j.neuroimage. 2010.07.033
- Fornito, A., & Bullmore, E. T. (2015). Connectomics: A new paradigm for understanding brain disease. *European Neuropsychopharmacology*, 25(5), 733–748. https://doi.org/https://doi.org/10.1016/j.euroneuro.2014.02.011
- Fransson, P. (2005). Spontaneous low-frequency bold signal fluctuations: An fmri investigation of the resting-state default mode of brain function hypothesis. *Hum Brain Mapp*, 26(1), 15–29. https://doi.org/10.1002/hbm.20113
- Ganella, E. P., Seguin, C., Pantelis, C., Whittle, S., Baune, B. T., Olver, J., Amminger, G. P., McGorry, P. D., Cropley, V., Zalesky, A., & Bartholomeusz, C. F. (2018). Resting-state functional brain networks in first-episode psychosis: A 12-month follow-up study. *Aust N Z J Psychiatry*, 52(9), 864–875. https://doi.org/10.1177/0004867418775833
- Gaser, C., Dahnke, R., Thompson, P. M., Kurth, F., Luders, E., & Initiative, A. D. N. (2022). Cat a computational anatomy toolbox for the analysis of structural mri data. *bioRxiv*, 2022.06.II.495736. https://doi.org/10.II0I/2022.06.II.495736

- Gassenmaier, S., Küstner, T., Nickel, D., Herrmann, J., Hoffmann, R., Almansour, H., Afat, S., Nikolaou, K., & Othman, A. E. (2021). Deep learning applications in magnetic resonance imaging: Has the future become present? *Diagnostics (Basel)*, 11(12). https://doi.org/10.3390/diagnostics11122181
- Glasser, M. F., Coalson, T. S., Bijsterbosch, J. D., Harrison, S. J., Harms, M. P., Anticevic, A., Van Essen, D. C., & Smith, S. M. (2019). Classification of temporal ica components for separating global noise from fmri data: Reply to power. *NeuroImage*, 197, 435–438. https://doi.org/https://doi.org/10.1016/j.neuroimage.2019.04.046
- Glasser, M. F., Coalson, T. S., Robinson, E. C., Hacker, C. D., Harwell, J., Yacoub, E., Ugurbil, K., Andersson, J., Beckmann, C. F., Jenkinson, M., Smith, S. M., & Van Essen, D. C. (2016). A multi-modal parcellation of human cerebral cortex. *Nature*, 536(7615), 171–178. https://doi.org/10.1038/nature18933
- Glover, G. H. (2011). Overview of functional magnetic resonance imaging. Neurosurg Clin N Am, 22(2), 133–9, vii. https://doi.org/10.1016/j.nec. 2010.11.001
- Gordon, E. M., Laumann, T. O., Adeyemo, B., Huckins, J. F., Kelley, W. M., & Petersen, S. E. (2014). Generation and evaluation of a cortical area parcellation from resting-state correlations. *Cerebral Cortex*, *26*(1), 288–303. https://doi.org/10.1093/cercor/bhu239
- Griffanti, L., Douaud, G., Bijsterbosch, J., Evangelisti, S., Alfaro-Almagro, F., Glasser, M. F., Duff, E. P., Fitzgibbon, S., Westphal, R., Carone, D., Beckmann, C. F., & Smith, S. M. (2017). Hand classification of fmri ica noise components. *Neuroimage*, 154, 188–205. https://doi.org/10.1016/j.neuroimage.2016.12.036
- Griffanti, L., Salimi-Khorshidi, G., Beckmann, C. F., Auerbach, E. J., Douaud, G., Sexton, C. E., Zsoldos, E., Ebmeier, K. P., Filippini, N., Mackay, C. E., Moeller, S., Xu, J., Yacoub, E., Baselli, G., Ugurbil, K., Miller, K. L., & Smith, S. M. (2014). Ica-based artefact removal and accelerated fmri acquisition for improved resting state network imaging. *NeuroImage*, 95, 232–247. https://doi.org/https://doi.org/10.1016/j.neuroimage.2014.03.034
- Griffin, A. D., Turtzo, L. C., Parikh, G. Y., Tolpygo, A., Lodato, Z., Moses, A. D., Nair, G., Perl, D. P., Edwards, N. A., Dardzinski, B. J., Armstrong, R. C., Ray-Chaudhury, A., Mitra, P. P., & Latour, L. L. (2019). Traumatic microbleeds suggest vascular injury and predict disability in

- traumatic brain injury. *Brain*, *142*(11), 3550–3564. https://doi.org/10. 1093/brain/awz290
- Gupte, R. P., Brooks, W. M., Vukas, R. R., Pierce, J. D., & Harris, J. L. (2019). Sex differences in traumatic brain injury: What we know and what we should know. *Journal of Neurotrauma*, *36*(22), 3063–3091. https://doi.org/10.1089/neu.2018.6171
- Han, Z., Wang, L., Yan, T., & Wu, J. (2021). A fineset cortex atlas of human brain based on boundary mapping technique: An 7t fmri study. *2021 2nd International Conference on Computer Engineering and Intelligent Control (ICCEIC)*, 29–34. https://doi.org/10.1109/ICCEIC54227. 2021.00014
- Hao, D., & Li, C. (2011). The dichotomy in degree correlation of biological networks. *PLOS ONE*, 6(12), e28322. https://doi.org/10.1371/journal.pone.0028322
- Harris, N. G., Verley, D. R., Gutman, B. A., Thompson, P. M., Yeh, H. J., & Brown, J. A. (2016). Disconnection and hyper-connectivity underlie reorganization after thi: A rodent functional connectomic analysis. *Exp Neurol*, 277, 124–138. https://doi.org/10.1016/j.expneurol.2015.12.020
- Higgins, I. A., Kundu, S., Choi, K. S., Mayberg, H. S., & Guo, Y. (2019). A difference degree test for comparing brain networks. *Hum Brain Mapp*, 40(15), 4518–4536. https://doi.org/10.1002/hbm.24718
- Higgins, I. A., Kundu, S., & Guo, Y. (2018). Integrative bayesian analysis of brain functional networks incorporating anatomical knowledge. *Neuroimage*, *181*, 263–278. https://doi.org/10.1016/j.neuroimage.2018.07.
- Hillman, E. M. (2014). Coupling mechanism and significance of the bold signal: A status report. *Annu Rev Neurosci*, *37*, 161–81. https://doi.org/10.1146/annurev-neuro-071013-014111
- Hirschberger, M., Qi, Y., & Steuer, R. E. (2007). Randomly generating portfolioselection covariance matrices with specified distributional characteristics. *European Journal of Operational Research*, 177(3), 1610–1625. https: //doi.org/10.1016/j.ejor.2005.10.014
- Horvath, K. A., Li, M., Mazilu, D., Guttman, M. A., & McVeigh, E. R. (2007). Real-time magnetic resonance imaging guidance for cardiovascular procedures. *Semin Thorac Cardiovasc Surg*, 19(4), 330–5. https://doi.org/10.1053/j.semtcvs.2007.10.006
- Hou, J., Nelson, R., Wilkie, Z., Mustafa, G., Tsuda, S., Thompson, F. J., & Bose, P. (2017). Mild and mild-to-moderate traumatic brain injury-induced significant progressive and enduring multiple comorbidities.

- *Journal of Neurotrauma*, *34*(16), 2456–2466. https://doi.org/10.1089/neu.2016.4851
- Hu, S., Wu, H., Xu, C., Wang, A., Wang, Y., Shen, T., Huang, F., Kan, H., & Li, C. (2019). Aberrant coupling between resting-state cerebral blood flow and functional connectivity in wilson's disease. *Front Neural Circuits*, 13, 25. https://doi.org/10.3389/fncir.2019.00025
- Hu, X., & Yan, C.-G. (2024). Current status and future challenges in brain imaging: Insights from leading experts. *Medicine Plus*, *1*(4), 100049. https://doi.org/https://doi.org/10.1016/j.medp.2024.100049
- Irimia, A., & Van Horn, J. D. (2015). Functional neuroimaging of traumatic brain injury: Advances and clinical utility. *Neuropsychiatr Dis Treat*, 11, 2355–65. https://doi.org/10.2147/ndt.S79174
- Jenkinson, M., Beckmann, C. F., Behrens, T. E. J., Woolrich, M. W., & Smith, S. M. (2012). Fsl. *NeuroImage*, *62*(2), 782–790. https://doi.org/https://doi.org/10.1016/j.neuroimage.2011.09.015
- Jennings, J. R., Muldoon, M. F., Whyte, E. M., Scanlon, J., Price, J., & Meltzer, C. C. (2008). Brain imaging findings predict blood pressure response to pharmacological treatment. *Hypertension*, 52(6), 1113–9. https://doi.org/10.1161/hypertensionaha.108.120196
- Ji, B., Li, Z., Li, K., Li, L., Langley, J., Shen, H., Nie, S., Zhang, R., & Hu, X. (2016). Dynamic thalamus parcellation from resting-state fmri data. *Human Brain Mapping*, 37(3), 954–967. https://doi.org/https://doi.org/10.1002/hbm.23079
- Jiang, L., & Zuo, X.-N. (2016). Regional homogeneity:a multimodal, multiscale neuroimaging marker of the human connectome. *The Neuroscientist*, 22(5), 486–505. https://doi.org/10.1177/1073858415595004
- Kashou, A. W., Frees, D. M., Kang, K., Parks, C. O., Harralson, H., Fischer, J. T., Rosenbaum, P. E., Baham, M., Sheridan, C., & Bickart, K. C. (2024). Drivers of resting-state fmri heterogeneity in traumatic brain injury across injury characteristics and imaging methods: A systematic review and semiquantitative analysis. *Front Neurol*, 15, 1487796. https://doi.org/10.3389/fneur.2024.1487796
- Khambhati, A. N., Sizemore, A. E., Betzel, R. F., & Bassett, D. S. (2018). Modeling and interpreting mesoscale network dynamics. *Neuroimage*, 180(Pt B), 337–349. https://doi.org/10.1016/j.neuroimage.2017.06.029
- Khosla, M., Jamison, K., Ngo, G. H., Kuceyeski, A., & Sabuncu, M. R. (2019). Machine learning in resting-state fmri analysis. *Magn Reson Imaging*, 64, 101–121. https://doi.org/10.1016/j.mri.2019.05.031

- Kinder, H. A., Baker, E. W., & West, F. D. (2019). The pig as a preclinical traumatic brain injury model: Current models, functional outcome measures, and translational detection strategies. *Neural Regeneration Research*, 14(3), 413–424. https://doi.org/10.4103/1673-5374.245334
- Kirkley, A. (2024). Identifying hubs in directed networks. *Physical Review E*, 109(3), 034310. https://doi.org/10.1103/PhysRevE.109.034310
- Korgaonkar, M. S., Ram, K., Williams, L. M., Gatt, J. M., & Grieve, S. M. (2014). Establishing the resting state default mode network derived from functional magnetic resonance imaging tasks as an endophenotype: A twins study. *Hum Brain Mapp*, 35(8), 3893–902. https://doi.org/10.1002/hbm.22446
- Kose, K. (2021). Physical and technical aspects of human magnetic resonance imaging: Present status and 50 years historical review. *Advances in Physics: X*, 6(1), 1885310. https://doi.org/10.1080/23746149.2021. 1885310
- Kumar, S., Zomorrodi, R., Ghazala, Z., Goodman, M. S., Blumberger, D. M., Cheam, A., Fischer, C., Daskalakis, Z. J., Mulsant, B. H., Pollock, B. G., & Rajji, T. K. (2017). Extent of dorsolateral prefrontal cortex plasticity and its association with working memory in patients with alzheimer disease. *JAMA Psychiatry*, 74(12), 1266–1274. https://doi.org/10.1001/jamapsychiatry.2017.3292
- Kwong, K. K., Belliveau, J. W., Chesler, D. A., Goldberg, I. E., Weisskoff, R. M., Poncelet, B. P., Kennedy, D. N., Hoppel, B. E., Cohen, M. S., Turner, R., & et al. (1992). Dynamic magnetic resonance imaging of human brain activity during primary sensory stimulation. *Proc Natl Acad Sci US A*, 89(12), 5675–9. https://doi.org/10.1073/pnas.89.12.5675
- Larson-Prior, L. J., Zempel, J. M., Nolan, T. S., Prior, F. W., Snyder, A. Z., & Raichle, M. E. (2009). Cortical network functional connectivity in the descent to sleep. *Proc Natl Acad Sci U S A*, 106(11), 4489–94. https://doi.org/10.1073/pnas.0900924106
- Lee, B., & Newberg, A. (2005). Neuroimaging in traumatic brain imaging. *NeuroRX*, 2(2), 372–383. https://doi.org/10.1602/neurorx.2.2.372
- Lee, J. S., Lee, D. S., Kim, J., Kim, Y. K., Kang, E., Kang, H., Kang, K. W., Lee, J. M., Kim, J. J., Park, H. J., Kwon, J. S., Kim, S. I., Yoo, T. W., Chang, K. H., & Lee, M. C. (2005). Development of korean standard brain templates. *J Korean Med Sci*, 20(3), 483–8. https://doi.org/10.3346/jkms.2005.20.3.483

- Lee, M. H., Smyser, C. D., & Shimony, J. S. (2013). Resting-state fmri: A review of methods and clinical applications. *AJNR Am J Neuroradiol*, *34*(10), 1866–72. https://doi.org/10.3174/ajnr.A3263
- Lemaire, J.-J., De Salles, A., Coll, G., El Ouadih, Y., Chaix, R., Coste, J., Durif, F., Makris, N., & Kikinis, R. (2019). Mri atlas of the human deep brain. Frontiers in Neurology, Volume 10 - 2019. https://doi.org/10.3389/fneur. 2019.00851
- Lemée, J. M., Berro, D. H., Bernard, F., Chinier, E., Leiber, L. M., Menei, P., & Ter Minassian, A. (2019). Resting-state functional magnetic resonance imaging versus task-based activity for language mapping and correlation with perioperative cortical mapping. *Brain Behav*, *9*(10), e01362. https://doi.org/10.1002/brb3.1362
- Li, K., Guo, L., Nie, J., Li, G., & Liu, T. (2009). Review of methods for functional brain connectivity detection using fmri. *Comput Med Imaging Graph*, 33(2), 131–9. https://doi.org/10.1016/j.compmedimag.2008.10.011
- Li, Y., Jewells, V., Kim, M., Chen, Y., Moon, A., Armao, D., Troiani, L., Markovic-Plese, S., Lin, W., & Shen, D. (2013). Diffusion tensor imaging based network analysis detects alterations of neuroconnectivity in patients with clinically early relapsing-remitting multiple sclerosis. *Hum Brain Mapp*, 34(12), 3376–91. https://doi.org/10.1002/hbm.22158
- Liang, P., Shi, L., Chen, N., Luo, Y., Wang, X., Liu, K., Mok, V. C. T., Chu, W. C. W., Wang, D., & Li, K. (2015). Construction of brain atlases based on a multi-center mri dataset of 2020 chinese adults. *Scientific Reports*, 5(1), 18216. https://doi.org/10.1038/srep18216
- Liang, X., Zou, Q., He, Y., & Yang, Y. (2015). Topologically reorganized connectivity architecture of default-mode, executive-control, and salience networks across working memory task loads. *Cerebral Cortex*, 26(4), 1501–1511. https://doi.org/10.1093/cercor/bhu316
- Logothetis, N. K. (2008). What we can do and what we cannot do with fmri. *Nature*, 453(7197), 869–878. https://doi.org/10.1038/nature06976
- López-Gil, X., Amat-Roldan, I., Tudela, R., Castañé, A., Prats-Galino, A., Planas, A. M., Farr, T. D., & Soria, G. (2014). Dwi and complex brain network analysis predicts vascular cognitive impairment in spontaneous hypertensive rats undergoing executive function tests. *Front Aging Neurosci*, *6*, 167. https://doi.org/10.3389/fnagi.2014.00167
- Lu, Y., Li, X., Geng, D., Mei, N., Wu, P. Y., Huang, C. C., Jia, T., Zhao, Y., Wang, D., Xiao, A., & Yin, B. (2020). Cerebral micro-structural changes in covid-19 patients an mri-based 3-month follow-up study.

- *EClinical Medicine*, *25*, 100484. https://doi.org/10.1016/j.eclinm.2020. 100484
- Luo, Z., Zeng, L. L., Qin, J., Hou, C., Shen, H., & Hu, D. (2020). Functional parcellation of human brain precuneus using density-based clustering. *Cereb Cortex*, 30(1), 269–282. https://doi.org/10.1093/cercor/bhz086
- Mahadevan, A. S., Tooley, U. A., Bertolero, M. A., Mackey, A. P., & Bassett, D. S. (2021). Evaluating the sensitivity of functional connectivity measures to motion artifact in resting-state fmri data. *NeuroImage*, 241, 118408. https://doi.org/https://doi.org/10.1016/j.neuroimage.2021. 118408
- Mann, R. M., Cho, N., & Moy, L. (2019). Breast mri: State of the art. *Radiology*, 292(3), 520–536. https://doi.org/10.1148/radiol.2019182947
- Mantini, D., Gerits, A., Nelissen, K., Durand, J. B., Joly, O., Simone, L., Sawamura, H., Wardak, C., Orban, G. A., Buckner, R. L., & Vanduffel, W. (2011). Default mode of brain function in monkeys. *J Neurosci*, 31(36), 12954–62. https://doi.org/10.1523/jneurosci.2318-11.2011
- Marrelec, G., Kim, J., Doyon, J., & Horwitz, B. (2009). Large-scale neural model validation of partial correlation analysis for effective connectivity investigation in functional mri. *Human Brain Mapping*, *30*(3), 941–950. https://doi.org/https://doi.org/10.1002/hbm.20555
- Maupu, C., Lebas, H., & Boulaftali, Y. (2022). Imaging modalities for intracranial aneurysm: More than meets the eye. *Front Cardiovasc Med*, *9*, 793072. https://doi.org/10.3389/fcvm.2022.793072
- Mazziotta, J. C., Toga, A. W., Evans, A., Fox, P., & Lancaster, J. (1995). A probabilistic atlas of the human brain: Theory and rationale for its development: The international consortium for brain mapping (icbm). *NeuroImage*, *2*(2, Part A), 89–101. https://doi.org/https://doi.org/10.1006/nimg.1995.1012
- McGillivray, J. E., Debruin, H., Kumbhare, D., & Noseworthy, M. D. (2021). The effect of exercise on neural activation and cognition: A review of task-based fmri studies. 49(2), 21–52. https://doi.org/10.1615/CritRevBiomedEng.2021038975
- McGlade, E., Rogowska, J., & Yurgelun-Todd, D. (2015). Sex differences in orbitofrontal connectivity in male and female veterans with tbi. *Brain Imaging and Behavior*, *9*(3), 535–549. https://doi.org/10.1007/s11682-015-9379-3
- McKeown, M. J., Makeig, S., Brown, G. G., Jung, T. P., Kindermann, S. S., Bell, A. J., & Sejnowski, T. J. (1998). Analysis of fmri data by blind separation into independent spatial components. *Hum Brain Mapp*,

- 6(3), 160–88. https://doi.org/10.1002/(SICI)1097-0193(1998)6: 3<160::AID-HBM5>3.0.CO;2-1
- McKeown, M. J., Hansen, L. K., & Sejnowsk, T. J. (2003). Independent component analysis of functional mri: What is signal and what is noise? *Current Opinion in Neurobiology*, 13(5), 620–629. https://doi.org/https://doi.org/10.1016/j.conb.2003.09.012
- McMillan, T. M., Teasdale, G. M., Weir, C. J., & Stewart, E. (2011). Death after head injury: The 13 year outcome of a case control study. *J Neurol Neurosurg Psychiatry*, 82(8), 931–5. https://doi.org/10.1136/jnnp.2010. 222232
- Medaglia, J. D. (2017). Graph theoretic analysis of resting state functional mr imaging. *Neuroimaging Clinics of North America*, 27(4), 593–607. https://doi.org/https://doi.org/10.1016/j.nic.2017.06.008
- Meehan, C. E., Schantell, M., Wiesman, A. I., Wolfson, S. L., O'Neill, J., Bares, S. H., Johnson, C. M., May, P. E., Murman, D. L., & Wilson, T. W. (2023). Oscillatory markers of neurohiv-related cognitive impairment and alzheimer's disease during attentional interference processing. *Aging (Albany NY)*, 15(2), 524–541. https://doi.org/10.18632/aging. 204496
- Melie-García, L., Sanabria-Diaz, G., & Sánchez-Catasús, C. (2013). Studying the topological organization of the cerebral blood flow fluctuations in resting state. *Neuroimage*, *64*, 173–84. https://doi.org/10.1016/j.neuroimage.2012.08.082
- Meyerholz, D. K., Burrough, E. R., Kirchhof, N., Anderson, D. J., & Helke, K. L. (2024). Swine models in translational research and medicine. *Veterinary Pathology*, 61(4), 512–523. https://doi.org/10.1177/03009858231222235
- Mika, D. (2023). Fast gradient algorithm for complex ica and its application to the mimo systems. *Sci Rep*, 13(1), 11633. https://doi.org/10.1038/s41598-023-36628-w
- Miri Ashtiani, S. N., Daliri, M. R., Behnam, H., Hossein-Zadeh, G.-A., Mehrpour, M., Motamed, M. R., & Fadaie, F. (2018). Altered topological properties of brain networks in the early ms patients revealed by cognitive task-related fmri and graph theory. *Biomedical Signal Processing and Control*, 40, 385–395. https://doi.org/https://doi.org/10.1016/j.bspc. 2017.10.006
- Mitsuyama, Y., Tatekawa, H., Takita, H., Sasaki, F., Tashiro, A., Oue, S., Walston, S. L., Nonomiya, Y., Shintani, A., Miki, Y., & Ueda, D. (2025). Comparative analysis of gpt-4-based chatgpt's diagnostic performance with radiologists using real-world radiology reports of brain tumors. *Eu-*

- *ropean Radiology*, *35*(4), 1938–1947. https://doi.org/10.1007/s00330-024-11032-8
- Moradi, M., Ekhtiari, H., Victor, T. A., Paulus, M., & Kuplicki, R. (2020). Image-derived phenotyping informed by independent component analysis—an atlas-based approach. *Frontiers in Neuroscience*, 14. https://doi.org/10.3389/fnins.2020.00118
- Morante, M., Kopsinis, Y., Chatzichristos, C., Protopapas, A., & Theodoridis, S. (2021). Enhanced design matrix for task-related fmri data analysis. *NeuroImage*, 245, 118719. https://doi.org/https://doi.org/10.1016/j. neuroimage.2021.118719
- Morgenstern, J. D., Rosella, L. C., Daley, M. J., Goel, V., Schünemann, H. J., & Piggott, T. (2021). "ai's gonna have an impact on everything in society, so it has to have an impact on public health": A fundamental qualitative descriptive study of the implications of artificial intelligence for public health. *BMC Public Health*, 21(1), 40. https://doi.org/10.1186/S12889-020-10030-x
- Mulert, C., Jäger, L., Schmitt, R., Bussfeld, P., Pogarell, O., Möller, H. J., Juckel, G., & Hegerl, U. (2004). Integration of fmri and simultaneous eeg: Towards a comprehensive understanding of localization and time-course of brain activity in target detection. *Neuroimage*, 22(1), 83–94. https://doi.org/10.1016/j.neuroimage.2003.10.051
- Naik, G. R., & Kumar, D. K. (2011). An overview of independent component analysis and its applications. *Informatica*, 35(1).
- (NCD-RisC), N. R. F. C. (2021). Worldwide trends in hypertension prevalence and progress in treatment and control from 1990 to 2019: A pooled analysis of 1201 population-representative studies with 104 million participants. *Lancet*, 398(10304), 957–980. https://doi.org/10.1016/s0140-6736(21)01330-1
- Netzley, A. H., & Pelled, G. (2023). The pig as a translational animal model for biobehavioral and neurotrauma research. *Biomedicines*, 11(8), 2165. https://www.mdpi.com/2227-9059/II/8/2I65%20https://pmc.ncbi.nlm.nih.gov/articles/PMC10452425/
- Niu, C., Wang, Y., Cohen, A. D., Liu, X., Li, H., Lin, P., Chen, Z., Min, Z., Li, W., Ling, X., Wen, X., Wang, M., Thompson, H. P., & Zhang, M. (2021). Machine learning may predict individual hand motor activation from resting-state fmri in patients with brain tumors in perirolandic cortex. *Eur Radiol*, 31(7), 5253–5262. https://doi.org/10.1007/s00330-021-07825-w

- Niu, C., Cohen, A. D., Wen, X., Chen, Z., Lin, P., Liu, X., Menze, B. H., Wiestler, B., Wang, Y., & Zhang, M. (2021). Modeling motor task activation from resting-state fmri using machine learning in individual subjects. *Brain Imaging and Behavior*, 15(1), 122–132. https://doi.org/10.1007/S11682-019-00239-9
- Nolin, P., & Heroux, L. (2006). Relations among sociodemographic, neurologic, clinical, and neuropsychologic variables, and vocational status following mild traumatic brain injury: A follow-up study. *J Head Trauma Rehabil*, 21(6), 514–26. https://doi.org/10.1097/00001199-200611000-00006
- Ogawa, S., Lee, T. M., Kay, A. R., & Tank, D. W. (1990). Brain magnetic resonance imaging with contrast dependent on blood oxygenation. *Proceedings of the National Academy of Sciences*, 87(24), 9868–9872. https://doi.org/doi.10.1073/pnas.87.24.9868
- Orringer, D. A., Vago, D. R., & Golby, A. J. (2012). Clinical applications and future directions of functional mri. *Semin Neurol*, 32(4), 466–75. https://doi.org/10.1055/s-0032-1331816
- Osier, N., & Dixon, C. E. (2016). The controlled cortical impact model of experimental brain trauma: Overview, research applications, and protocol. In F. H. Kobeissy, C. E. Dixon, R. L. Hayes, & S. Mondello (Eds.), *Injury models of the central nervous system: Methods and protocols* (pp. 177–192). Springer New York. https://doi.org/10.1007/978-1-4939-3816-2 11
- Pamplona, G. S. P., Vieira, B. H., Scharnowski, F., & Salmon, C. E. G. (2020). Personode: A toolbox for ica map classification and individualized roi definition. *Neuroinformatics*, 18(3), 339–349. https://doi.org/10.1007/s12021-019-09449-4
- Payne, M., Mali, I., Mueller, T., Cain, M., Segev, R., & Bossmann, S. H. (2023).

 Super-resolution reconstruction in ultrahigh-field mri [doi: 10.1016/j.bpr.2023.100107].

 Biophysical Reports, 3(2). https://doi.org/10.1016/j.bpr.2023.100107
- Pendse, G. V., Borsook, D., & Becerra, L. (2011). A simple and objective method for reproducible resting state network (rsn) detection in fmri. *PLoS One*, *δ*(12), e27594. https://doi.org/10.1371/journal.pone.0027594
- Penny, W. D., Friston, K. J., Ashburner, J. T., Kiebel, S. J., & Nichols, T. E. (2007). Statistical parametric mapping: The analysis of functional brain images. Academic Press. https://doi.org/https://doi.org/10.1016/B978-0-12-372560-8.X5000-1

- Penny, W. D., Friston, K. J., Ashburner, J. T., Kiebel, S. J., & Nichols, T. E. (2011). *Statistical parametric mapping: The analysis of functional brain images*. Elsevier.
- Peterson, A. B., Xu, L., Daugherty, J., & Breiding, M. J. (2019). Surveillance report of traumatic brain injury-related emergency department visits, hospitalizations, and deaths, united states, 2014. https://stacks.cdc.gov/view/cdc/78062
- Pospelov, N., Tetereva, A., Martynova, O., & Anokhin, K. (2021). The laplacian eigenmaps dimensionality reduction of fmri data for discovering stimulus-induced changes in the resting-state brain activity. *Neuroimage: Reports*, 1(3). https://doi.org/https://doi.org/10.1016/j.ynirp.2021. 100035
- Prieto Del Val, L., Cantero, J. L., & Atienza, M. (2016). Atrophy of amygdala and abnormal memory-related alpha oscillations over posterior cingulate predict conversion to alzheimer's disease. *Sci Rep*, 6, 31859. https://doi.org/10.1038/srep31859
- Puffer, R. C., Yue, J. K., Mesley, M., Billigen, J. B., Sharpless, J., Fetzick, A. L., Puccio, A., Diaz-Arrastia, R., & Okonkwo, D. O. (2019). Long-term outcome in traumatic brain injury patients with midline shift: A secondary analysis of the phase 3 cobrit clinical trial. *Journal of Neuro-surgery JNS*, 131(2), 596–603. https://doi.org/https://doi.org/10.3171/2018.2.JNS173138
- Raichle, M. E. (1998). Behind the scenes of functional brain imaging: A historical and physiological perspective. *Proc Natl Acad Sci US A*, 95(3), 765–72. https://doi.org/10.1073/pnas.95.3.765
- Reeves, W. D., Ahmed, I., Jackson, B. S., Sun, W., Brown, M. L., Williams, C. F., Davis, C. L., McDowell, J. E., Yanasak, N. E., Su, S., & Zhao, Q. (2023). Characterization of resting-state functional connectivity changes in hypertension by a modified difference degree test. *Brain Connect*, 13(9), 563–573. https://doi.org/10.1089/brain.2023.0001
- Reeves, W. D., Ahmed, I., Jackson, B. S., Sun, W., Williams, C. F., Davis, C. L., McDowell, J. E., Yanasak, N. E., Su, S., & Zhao, Q. (2025). Fmri-based data-driven brain parcellation using independent component analysis. *Journal of Neuroscience Methods*, 417, 110403. https://doi.org/https://doi.org/10.1016/j.jneumeth.2025.110403
- Reeves, W. D., Ahmed, I., Sun, W., Brown, M., Williams, C., Davis, C. L., McDowell, J. E., Yanasak, N., Su, S., & Zhao, Q. (2023). Analyzing cbf connectivity differences affected by hypertension in arterial spin

- labelled data using graph theory. *International Society for Magnetic Resonance in Medicine Annual Meeting*, Abstract #4903.
- Rolls, E. T., Huang, C. C., Lin, C. P., Feng, J., & Joliot, M. (2020). Automated anatomical labelling atlas 3. *Neuroimage*, 206, 116189. https://doi.org/10.1016/j.neuroimage.2019.116189
- Rubin, T. G., & Lipton, M. L. (2019). Sex differences in animal models of traumatic brain injury. *J Exp Neurosci*, 13, 1179069519844020. https://doi.org/10.1177/1179069519844020
- Ryali, S., Chen, T., Padmanabhan, A., Cai, W., & Menon, V. (2015). Development and validation of consensus clustering-based framework for brain segmentation using resting fmri. *J Neurosci Methods*, 240, 128–40. https://doi.org/10.1016/j.jneumeth.2014.11.014
- Salman, M. S., Wager, T. D., Damaraju, E., Abrol, A., Vergara, V. M., Fu, Z., & Calhoun, V. D. (2022). An approach to automatically label and order brain activity/component maps. *Brain Connect*, 12(1), 85–95. https://doi.org/10.1089/brain.2020.0950
- Schantz, S. L., Sneed, S. E., Fagan, M. M., Golan, M. E., Cheek, S. R., Kinder, H. A., Duberstein, K. J., Kaiser, E. E., & West, F. D. (2024). Human-induced pluripotent stem cell-derived neural stem cell therapy limits tissue damage and promotes tissue regeneration and functional recovery in a pediatric piglet traumatic-brain-injury model. *Biomedicines*, 12(8), 1663. https://www.mdpi.com/2227-9059/12/8/1663%20https://pmc.ncbi.nlm.nih.gov/articles/PMC11351842/
- Seitzman, B. A., Snyder, A. Z., Leuthardt, E. C., & Shimony, J. S. (2019). The state of resting state networks. *Topics in Magnetic Resonance Imaging*, 28(4), 189–196. https://doi.org/10.1097/rmr.00000000000014
- Serrano, N., López-Sanz, D., Bruña, R., Garcés, P., Rodríguez-Rojo, I. C., Marcos, A., Crespo, D. P., & Maestú, F. (2020). Spatiotemporal oscillatory patterns during working memory maintenance in mild cognitive impairment and subjective cognitive decline. *Int J Neural Syst*, *30*(1), 1950019. https://doi.org/10.1142/s0129065719500199
- Shah, C., Srinivasan, D., Erus, G., Schmitt, J. E., Agarwal, A., Cho, M. E., Lerner, A. J., Haley, W. E., Kurella Tamura, M., Davatzikos, C., Bryan, R. N., Fan, Y., & Nasrallah, I. M. (2021). Changes in brain functional connectivity and cognition related to white matter lesion burden in hypertensive patients from sprint. *Neuroradiology*, *63*(6), 913–924. https://doi.org/10.1007/s00234-020-02614-6

- Shi, L., Yang, Q., He, P., & Xu, Y. (2009). A model of selecting the parameters based on the variance of distance ratios for manifold learning algorithms. https://doi.org/10.1109/fskd.2009.471
- Sidhu, G. S., Asgarian, N., Greiner, R., & Brown, M. R. (2012). Kernel principal component analysis for dimensionality reduction in fmri-based diagnosis of adhd. *Frontiers in Systems Neuroscience*, *Volume 6 2012*. https://doi.org/10.3389/fnsys.2012.00074
- Sierakowiak, A., Monnot, C., Aski, S. N., Uppman, M., Li, T. Q., Damberg, P., & Brené, S. (2015). Default mode network, motor network, dorsal and ventral basal ganglia networks in the rat brain: Comparison to human networks using resting state-fmri. *PLoS One*, 10(3), e0120345. https://doi.org/10.1371/journal.pone.0120345
- Simchick, G., Liu, Z., Nagy, T., Xiong, M., & Zhao, Q. (2018). Assessment of mr-based r2* and quantitative susceptibility mapping for the quantification of liver iron concentration in a mouse model at 7t. *Magn Reson Med*, 80(5), 2081–2093. https://doi.org/10.1002/mrm.27173
- Simchick, G., Scheulin, K. M., Sun, W., Sneed, S. E., Fagan, M. M., Cheek, S. R., West, F. D., & Zhao, Q. (2021). Detecting functional connectivity disruptions in a translational pediatric traumatic brain injury porcine model using resting-state and task-based fmri. *Sci Rep*, 11(1), 12406. https://doi.org/10.1038/s41598-021-91853-5
- Simchick, G., Shen, A., Campbell, B., Park, H. J., West, F. D., & Zhao, Q. (2019). Pig brains have homologous resting-state networks with human brains. *Brain Connect*, 9(7), 566–579. https://doi.org/10.1089/brain.2019.0673
- Simchick, G., Zhao, R., Hamilton, G., Reeder, S. B., & Hernando, D. (2022). Spectroscopy-based multi-parametric quantification in subjects with liver iron overload at 1.5t and 3t. *Magnetic Resonance in Medicine*, 87(2), 597–613. https://doi.org/https://doi.org/10.1002/mrm.29021
- Slater, J., & Humphries, J. (2025). Another reason to call bullshit on ai "hallucinations". *AI & SOCIETY*. https://doi.org/10.1007/s00146-025-02346-2
- Smith, S. M., Fox, P. T., Miller, K. L., Glahn, D. C., Fox, P. M., Mackay, C. E., Filippini, N., Watkins, K. E., Toro, R., Laird, A. R., & Beckmann, C. F. (2009). Correspondence of the brain's functional architecture during activation and rest. *Proc Natl Acad Sci USA*, 106(31), 13040–5. https://doi.org/10.1073/pnas.0905267106
- Smith, S. M., Vidaurre, D., Beckmann, C. F., Glasser, M. F., Jenkinson, M., Miller, K. L., Nichols, T. E., Robinson, E. C., Salimi-Khorshidi, G., Woolrich, M. W., Barch, D. M., Uğurbil, K., & Van Essen, D. C. (2013).

- Functional connectomics from resting-state fmri. *Trends Cogn Sci*, 17(12), 666–82. https://doi.org/10.1016/j.tics.2013.09.016
- Smith, S. M., Hyvärinen, A., Varoquaux, G., Miller, K. L., & Beckmann, C. F. (2014). Group-pca for very large fmri datasets. *NeuroImage*, 101, 738–749. https://doi.org/https://doi.org/10.1016/j.neuroimage.2014.07.051
- Smith, S. M., Jenkinson, M., Woolrich, M. W., Beckmann, C. F., Behrens, T. E. J., Johansen-Berg, H., Bannister, P. R., De Luca, M., Drobnjak, I., Flitney, D. E., Niazy, R. K., Saunders, J., Vickers, J., Zhang, Y., De Stefano, N., Brady, J. M., & Matthews, P. M. (2004). Advances in functional and structural mr image analysis and implementation as fsl. *NeuroImage*, *23*, S208–S219. https://doi.org/https://doi.org/10.1016/j. neuroimage.2004.07.051
- Smitha, K. A., Akhil Raja, K., Arun, K. M., Rajesh, P. G., Thomas, B., Kapilamoorthy, T. R., & Kesavadas, C. (2017). Resting state fmri: A review on methods in resting state connectivity analysis and resting state networks. *Neuroradiol J*, 30(4), 305–317. https://doi.org/10.1177/1971400917697342
- Sollmann, N., Fields, A. J., O'Neill, C., Nardo, L., Majumdar, S., Chin, C. T., Tosun, D., Han, M., Vu, A. T., Ozhinsky, E., Shah, L. M., Harris, R. E., Lobo, R., Anderst, W., Herzog, R., Psioda, M. A., Standaert, C. J., Price, R. T., Lotz, J. C., ... Krug, R. (2023). Magnetic resonance imaging of the lumbar spine: Recommendations for acquisition and image evaluation from the bacpac spine imaging working group. *Pain Med*, 24(Suppl 1), S81–s94. https://doi.org/10.1093/pm/pnac130
- Song, M., Zhou, Y., Li, J., Liu, Y., Tian, L., Yu, C., & Jiang, T. (2008). Brain spontaneous functional connectivity and intelligence. *Neuroimage*, 41(3), 1168–76. https://doi.org/10.1016/j.neuroimage.2008.02.036
- Specht, K. (2019). Current challenges in translational and clinical fmri and future directions. *Front Psychiatry*, 10, 924. https://doi.org/10.3389/fpsyt.2019.00924
- Stein, S. C., Georgoff, P., Meghan, S., Mizra, K., & Sonnad, S. S. (2010). 150 years of treating severe traumatic brain injury: A systematic review of progress in mortality. *Journal of Neurotrauma*, 27(7), 1343–1353. https://doi.org/10.1089/neu.2009.1206
- Stikov, N., Trzasko, J. D., & Bernstein, M. A. (2019). Reproducibility and the future of mri research. *Magnetic Resonance in Medicine*, 82(6), 1981–1983. https://doi.org/https://doi.org/10.1002/mrm.27939

- Stöcker, T., Keenan, K. E., Knoll, F., Priovoulos, N., Uecker, M., & Zaitsev, M. (2025). Reproducibility and quality assurance in mri. *Magnetic Resonance Materials in Physics, Biology and Medicine*. https://doi.org/10.1007/S10334-025-01271-1
- Tang, Y., Hojatkashani, C., Dinov, I. D., Sun, B., Fan, L., Lin, X., Qi, H., Hua, X., Liu, S., & Toga, A. W. (2010). The construction of a chinese mri brain atlas: A morphometric comparison study between chinese and caucasian cohorts. *NeuroImage*, 51(1), 33–41. https://doi.org/https://doi.org/10.1016/j.neuroimage.2010.01.111
- Teasdale, G., & Jennett, B. (1974). Assessment of coma and impaired consciousness. a practical scale [Teasdale, G Jennett, B Journal Article England 1974/07/13 Lancet. 1974 Jul 13;2(7872):81-4. doi: 10.1016/s0140-6736(74)91639-0.]. *Lancet*, 2(7872), 81–4. https://doi.org/10.1016/s0140-6736(74)91639-0
- Terribilli, D., Schaufelberger, M. S., Duran, F. L., Zanetti, M. V., Curiati, P. K., Menezes, P. R., Scazufca, M., Amaro, J., E., Leite, C. C., & Busatto, G. F. (2011). Age-related gray matter volume changes in the brain during non-elderly adulthood. *Neurobiol Aging*, 32(2), 354–68. https://doi.org/10.1016/j.neurobiolaging.2009.02.008
- Thirion, B., Flandin, G., Pinel, P., Roche, A., Ciuciu, P., & Poline, J. B. (2006). Dealing with the shortcomings of spatial normalization: Multi-subject parcellation of fmri datasets. *Hum Brain Mapp*, *27*(8), 678–93. https://doi.org/10.1002/hbm.20210
- Thomas, B. P., Yezhuvath, U. S., Tseng, B. Y., Liu, P., Levine, B. D., Zhang, R., & Lu, H. (2013). Life-long aerobic exercise preserved baseline cerebral blood flow but reduced vascular reactivity to co2. *J Magn Reson Imaging*, 38(5), 1177–83. https://doi.org/10.1002/jmri.24090
- Thomas, C. G., Harshman, R. A., & Menon, R. S. (2002). Noise reduction in bold-based fmri using component analysis. *NeuroImage*, 17(3), 1521–1537. https://doi.org/https://doi.org/10.1006/nimg.2002.1200
- Thomas Yeo, B. T., Krienen, F. M., Sepulcre, J., Sabuncu, M. R., Lashkari, D., Hollinshead, M., Roffman, J. L., Smoller, J. W., Zöllei, L., Polimeni, J. R., Fischl, B., Liu, H., & Buckner, R. L. (2011). The organization of the human cerebral cortex estimated by intrinsic functional connectivity. *Journal of Neurophysiology*, 106(3), 1125–1165. https://doi.org/10.1152/jn.00338.2011
- Truhn, D., Weber, C. D., Braun, B. J., Bressem, K., Kather, J. N., Kuhl, C., & Nebelung, S. (2023). A pilot study on the efficacy of gpt-4 in providing

- orthopedic treatment recommendations from mri reports. *Scientific Reports*, 13(1), 20159. https://doi.org/10.1038/s41598-023-47500-2
- Tzourio-Mazoyer, N., Landeau, B., Papathanassiou, D., Crivello, F., Etard, O., Delcroix, N., Mazoyer, B., & Joliot, M. (2002). Automated anatomical labeling of activations in spm using a macroscopic anatomical parcellation of the mni mri single-subject brain. *NeuroImage*, *15*(1), 273–289. https://doi.org/https://doi.org/10.1006/nimg.2001.0978
- Uludağ, K. (2023). Physiological modeling of the bold signal and implications for effective connectivity: A primer. *NeuroImage*, 277, 120249. https://doi.org/https://doi.org/10.1016/j.neuroimage.2023.120249
- Valente, J. H., Anderson, J. D., Paolo, W. F., Sarmiento, K., Tomaszewski, C. A., Haukoos, J. S., Diercks, D. B., Diercks, D. B., Anderson, J. D., Byyny, R., Carpenter, C. R., Friedman, B., Gemme, S. R., Gerardo, C. J., Godwin, S. A., Hahn, S. A., Hatten, B. W., Haukoos, J. S., Kaji, A., ... Vandertulip, K. (2023). Clinical policy: Critical issues in the management of adult patients presenting to the emergency department with mild traumatic brain injury: Approved by acep board of directors, february 1, 2023 clinical policy endorsed by the emergency nurses association (april 5, 2023). *Ann Emerg Med*, 81(5), e63–e105. https://doi.org/10.1016/j.annemergmed.2023.01.014
- van Oort, E. S. B., Mennes, M., Navarro Schröder, T., Kumar, V. J., Zaragoza Jimenez, N. I., Grodd, W., Doeller, C. F., & Beckmann, C. F. (2018). Functional parcellation using time courses of instantaneous connectivity. *NeuroImage*, 170, 31–40. https://doi.org/https://doi.org/10.1016/j. neuroimage.2017.07.027
- van den Heuvel, M. P., & Hulshoff Pol, H. E. (2010). Exploring the brain network: A review on resting-state fmri functional connectivity. *European Neuropsychopharmacology*, *20*(8), 519–534. https://doi.org/https://doi.org/10.1016/j.euroneuro.2010.03.008
- Viviani, R., Grön, G., & Spitzer, M. (2005). Functional principal component analysis of fmri data. *Human Brain Mapping*, *24*(2), 109–129. https://doi.org/https://doi.org/10.1002/hbm.20074
- Vogt, N. (2023). Reproducibility in mri. *Nature Methods*, 20(1), 34–34. https://doi.org/10.1038/s41592-022-01737-3
- Wang, H., Baker, E. W., Mandal, A., Pidaparti, R. M., West, F. D., & Kinder, H. A. (2021). Identification of predictive mri and functional biomarkers in a pediatric piglet traumatic brain injury model. *Neural Regeneration Research*, 16(2), 338–344. https://doi.org/10.4103/1673-5374.290915

- Wang, J., Zuo, X., & He, Y. (2010). Graph-based network analysis of restingstate functional mri. *Frontiers in Systems Neuroscience*, 4(16). https://doi.org/10.3389/fnsys.2010.00016
- Wang, S., Hu, L., Cao, J., Huang, W., Sun, C., Zheng, D., Wang, Z., Gan, S., Niu, X., Gu, C., Bai, G., Ye, L., Zhang, D., Zhang, N., Yin, B., Zhang, M., & Bai, L. (2018). Sex differences in abnormal intrinsic functional connectivity after acute mild traumatic brain injury. Front Neural Circuits, 12, 107. https://doi.org/10.3389/fncir.2018.00107
- Wylie, K. P., Vu, T., Legget, K. T., & Tregellas, J. R. (2024). Hierarchical principal components for data-driven multiresolution fmri analyses. *Brain Sci*, 14(4). https://doi.org/10.3390/brainsci14040325
- Xia, M., & He, Y. (2011). Magnetic resonance imaging and graph theoretical analysis of complex brain networks in neuropsychiatric disorders. *Brain Connectivity*, *I*(5), 349–365. https://doi.org/10.1089/brain.2011. 0062
- Xu, Z., Lai, J., Zhang, H., Ng, C. H., Zhang, P., Xu, D., & Hu, S. (2019).

 Regional homogeneity and functional connectivity analysis of restingstate magnetic resonance in patients with bipolar ii disorder. *Medicine*(*Baltimore*), 98(47), e17962. https://doi.org/10.1097/md.000000000017962
- Yaesoubi, M., Allen, E. A., Miller, R. L., & Calhoun, V. D. (2015). Dynamic coherence analysis of resting fmri data to jointly capture state-based phase, frequency, and time-domain information. *NeuroImage*, 120, 133–142. https://doi.org/https://doi.org/10.1016/j.neuroimage.2015.07.002
- Yoshino, A., Kawamoto, M., Yoshida, T., Kobayashi, N., Shigemura, J., Takahashi, Y., & Nomura, S. (2006). Activation time course of responses to illusory contours and salient region: A high-density electrical mapping comparison. *Brain Res*, 1071(1), 137–44. https://doi.org/10.1016/j.brainres.2005.11.089
- Yuh, E. L., Mukherjee, P., Lingsma, H. F., Yue, J. K., Ferguson, A. R., Gordon, W. A., Valadka, A. B., Schnyer, D. M., Okonkwo, D. O., Maas, A. I. R., Manley, G. T., & Investigators, t. T.-T. (2013). Magnetic resonance imaging improves 3-month outcome prediction in mild traumatic brain injury. *Annals of Neurology*, 73(2), 224–235. https://doi.org/https://doi.org/10.1002/ana.23783
- Zalesky, A., Fornito, A., & Bullmore, E. (2012). On the use of correlation as a measure of network connectivity. *Neuroimage*, *60*(4), 2096–106. https://doi.org/10.1016/j.neuroimage.2012.02.001

- Zaloshnja, E., Miller, T., Langlois, J. A., & Selassie, A. W. (2008). Prevalence of long-term disability from traumatic brain injury in the civilian population of the united states, 2005. *J Head Trauma Rehabil*, 23(6), 394–400. https://doi.org/10.1097/01.HTR.0000341435.52004.ac
- Zang, Y., Jiang, T., Lu, Y., He, Y., & Tian, L. (2004). Regional homogeneity approach to fmri data analysis. *NeuroImage*, 22(1), 394–400. https://doi.org/https://doi.org/10.1016/j.neuroimage.2003.12.030
- Zhan, J., Gao, L., Zhou, F., Kuang, H., Zhao, J., Wang, S., He, L., Zeng, X., & Gong, H. (2015). Decreased regional homogeneity in patients with acute mild traumatic brain injury: A resting-state fmri study. *J Nerv Ment Dis*, 203(10), 786–91. https://doi.org/10.1097/nmd.000000000000368
- Zhan, X., & Yu, R. (2015). A window into the brain: Advances in psychiatric fmri. *Biomed Res Int*, 2015, 542467. https://doi.org/10.1155/2015/542467
- Zhang, F., Hua, B., Wang, M., Wang, T., Ding, Z., & Ding, J.-R. (2021). Regional homogeneity abnormalities of resting state brain activities in children with growth hormone deficiency. *Scientific Reports*, 11(1), 334. https://doi.org/10.1038/s41598-020-79475-9
- Zhang, S., Li, X., Lv, J., Jiang, X., Guo, L., & Liu, T. (2016). Characterizing and differentiating task-based and resting state fmri signals via two-stage sparse representations. *Brain Imaging Behav*, 10(1), 21–32. https://doi.org/10.1007/s11682-015-9359-7
- Zhang, Z., Wu, Y., Luo, Q., Tu, J., Li, J., Xiong, J., Lv, H., & Ye, J. (2023). Regional homogeneity alterations of resting-state functional magnetic resonance imaging of chronic rhinosinusitis with olfactory dysfunction. *Frontiers in Neuroscience, Volume 17 2023.* https://doi.org/10.3389/fnins.2023.1146259
- Zou, Q.-H., Zhu, C.-Z., Yang, Y., Zuo, X.-N., Long, X.-Y., Cao, Q.-J., Wang, Y.-F., & Zang, Y.-F. (2008). An improved approach to detection of amplitude of low-frequency fluctuation (alff) for resting-state fmri: Fractional alff. *Journal of Neuroscience Methods*, 172(1), 137–141. https://doi.org/https://doi.org/10.1016/j.jneumeth.2008.04.012